THE UNIVERSITY *of* EDINBURGH

Electrical impedance tomography for real-time 3D tissue culture monitoring

Hancong Wu

A thesis submitted for the degree of Doctor of Philosophy

The University of Edinburgh

September 2019

Declaration

I hereby declare that the work presented in this thesis is my own unless otherwise acknowledged. This thesis has not been submitted for any other degree or professional qualification except to The University of Edinburgh for the degree of Doctor of Philosophy.

Hancong Wu

Date: 01/08/2019

Table of Contents

Acknowledgements

First of all, I would like to express my deepest gratitude to my principal PhD supervisor, Dr. Jiabin Jia, for all his help and support and for giving me the opportunity to work on such an exciting project. I will never forget his invaluable guidance and encouragement to my study and my daily life. All of my achievements would not have been possible without his patience, assistance and suggestions.

I would also like to thank my assistant supervisor, Dr. Pierre Bagnaninchi, for all his guidance and suggestions in cell culture and tissue engineering. Thank you for always been there to help and push me beyond my limits. Meanwhile, I want to thank my assistant supervisor, Dr. Javier Escudero Rodriguez, for his valuable advises in the selection of my research topics and his suggestions in signal processing.

Besides, I am grateful to my collaborators, Dr. Yunjie Yang, Dr. Wenli Zhou, Dr. Xipeng Yin, Dr. Shengheng Liu and Dr. Yong Bao, for their kind assistance and support since I undertook this work. I would extend my thanks to other colleagues in the Agile Tomography Group for all the discussions, lunches, dinners, coffees and drinks that we had.

Furthermore, I appreciate Katalin Kis, Helen Cope, Iain Gold and all the technicians at the biological laboratory and the electronics laboratory for always maintaining an excellent experimental environment and being so efficient in getting the job done.

Lastly but most importantly, I would like to take this opportunity to express my sincere thanks to my parents, Shaoping Li and Prof. Zhenqiang Wu. Thank you very much for encouraging me and helping me develop my self-confidence. Your selfless love and support enable me to go through the hard time and to surpass myself. I dedicate this thesis to you.

Lay Summary

Electrical impedance tomography (EIT) is a non-destructive imaging technique that can monitor the conductivity change in a confined space. Compared with other imaging techniques, EIT has the advantages of the low-cost, high-temporal resolution, non-destructive and non-radiative. Therefore, it has been widely applied in clinical applications, including thorax imaging, lung ventilation monitoring, breast cancer screening and functional brain imaging.

This thesis aims to improve the performance of EIT in miniature imaging and to apply it in real-time 3D tissue culture monitoring. Biological cells cultured in 3D can better mimic the behaviour of cells growing in the natural environment, but it is difficult for conventional techniques to monitor the condition of cells non-destructively due to the thickness of the tissue. Focusing on this challenge, this thesis introduces new protocols for real-time 3D tissue culture monitoring utilising EIT system and miniature EIT sensor and demonstrates novel models to analyse the characteristics of 3D tissue samples through EIT. The results of this thesis help the development of monitoring techniques in drug discovery and tissue engineering applications.

Abstract

Electrical impedance tomography (EIT) is an emerging image technique that can image the spatial conductivity distribution in the sensing area by generating an electric field and measuring the induced boundary voltages. With the advantages of low-cost, high-temporal resolution, non-destructive and non-radiative, EIT has been developed for the clinical applications, including thorax imaging, lung ventilation monitoring, breast cancer screening and functional brain imaging. Its feasibility for monitoring the motion and conductivity change of the human tissues has been well investigated. It, therefore, shows enormous potential in the *in-vitro* cellular characterisation, where samples have the same electrical properties as *in-vivo* human tissues.

Since conventional biological imaging techniques are mainly optimised for the monolayer cell culture, their performance is limited when processing the dense, highly scattering tissues, which can better mimic the *in vivo* situation than 2D cultured cells. Utilising EIT as a novel method to monitor these 3D samples may help to overcome the difficulties and improve the temporal resolution of the data. This thesis aims to evaluate the feasibility of miniature EIT for 3D sample imaging and improve its performance for real-time 3D tissue culture monitoring. Phantom studies were first carried out to evaluate the challenges of EIT imaging when performing in the sensors in the millimetre scale. Different imaging settings, including imaging modality and measuring frequency, were compared, and a combined regularisation method is proposed to improve the image quality. Besides, a physical model for 3D biological tissue was developed to estimate its equivalent conductivity through the electrical properties and volume fraction of cells. The spatial resolution of EIT for tissue culture imaging was examined based on the model. In addition, the protocols of time-difference and frequency-difference EIT for 3D tissue culture monitoring in tightly packed spheroids and sparsely distributed bioscaffolds have been developed and verified through the experiments utilising MCF-7 breast cancer cells. Moreover, equivalent circuit models were developed for the EIT measurement, and a joint simulation method combining the finite-

element model and equivalent circuit analysis was developed to analyse the measurement error in frequency-difference EIT. Finally, a calibration method was developed to eliminate the circuitry errors in frequency-difference EIT so that it can be applied for the long-term monitoring in biological applications.

In summary, this thesis presents the research works on improving the robustness of miniature EIT to the measuring noise and the background disturbance through the optimization of experimental protocols, measuring methods and imaging settings. It shows the potential to be applied in biological research using 3D cell culture, including drug discovery and tissue engineering.

List of Tables

List of Figures

Abbreviations

1D, 2D, 3D	1 Dimensional, 2 Dimensional, 3 Dimensional
AC	Alternating Current
ADC	Analog-to-Digital Converter
CC	Correlation Coefficient
CEM	Complete Electrode Model
CFDEIT	Calibrated Frequency-difference EIT
DC	Direct Current
DMEM	Dulbecco's Modified Eagle Medium
ECIS	Electric Cell-substrate Impedance Sensing
EIS	Electrical Impedance Spectroscopy
EIT	Electrical Impedance Tomography
EMA	Effective Medium Approximation
FBS	Fetal Bovine Serum
FDEIT	Frequency-difference Electrical Impedance Tomography
FE	Finite Element
FEM	Finite Element Method
fps	Frames per second
HG	High Glucose

KVL	Kirchhoff’s Voltage Law
LoG	Laplacian of Gaussian
PBS	Phosphate-Buffered Saline
PE	Position Error
RCF	Relative Centrifugal Forces
RLU	Relative Light Unit
RoI	Region of Interest
SEM	Scanning Electron Microscopy
SNR	Signal to Noise Ratio
SR	Sub-domain-based Regularisation
SSR	Spectra Sub-domain-based Regularisation
TDEIT	Time-difference Electrical Impedance Tomography
TEER	Trans-Epithelial Electrical Resistance
TEM	Transmission Electron Microscopy
TLoG	Tikhonov regularisation with LoG

Publication List

Journal papers

1. **H. Wu**, Y. Yang, P. Bagnaninchi, and J. Jia, " Calibrated frequency-difference electrical impedance tomography for 3D tissue culture monitoring", *IEEE Sensors Journal*, 2019 (Accepted).
2. **H. Wu**, Y. Yang, P. Bagnaninchi, and J. Jia, "Electrical Impedance Tomography for real-time and label-free cellular viability assays of 3D tumour spheroids", *Analyst*, vol. 143, pp. 4189-4198, 2018.
3. **H. Wu**, W. Zhou, Y. Yang, J. Jia, and P. Bagnaninchi, "Exploring the Potential of Electrical Impedance Tomography for Tissue Engineering Applications," *Materials*, vol. 11, p. 930, 2018.
4. X. Yin, **H. Wu (Co-first author)**, J. Jia, and Y. Yang, "A Micro EIT Sensor for Real-time and Non-destructive 3-D Cultivated Cell Imaging," *IEEE Sensors Journal*, vol. 18, pp. 5402-5412, 2018.
5. Y. Yang, **H. Wu**, P. Bagnaninchi and J. Jia, "Scaffold-based 3-D Cell Culture Imaging Using a Miniature Electrical Impedance Tomography Sensor", *IEEE Sensors Journal*, 2019 (Accepted).
6. S. Liu, **H. Wu**, Y. Huang, Y. Yang and J. Jia, "Accelerated Structure-Aware Sparse Bayesian Learning for 3D Electrical Impedance Tomography." *IEEE Transactions on Industrial Informatics*, 2019.
7. W. Gamal, **H. Wu**, I. Underwood, J. Jia, S. Smith, and P. Bagnaninchi, "Impedance-based cellular assays for regenerative medicine," *Philosophical Transactions of the Royal Society B*, vol. 373, p. 20170226, 2018.
8. Y. Yang, **H. Wu**, and J. Jia, "Image Reconstruction for Electrical Impedance Tomography Using Enhanced Adaptive Group Sparsity with Total Variation," *IEEE Sensors Journal*, vol. 17, pp. 5589-5598, 2017.

Conference Papers

9. **H. Wu**, P. Bagnaninchi, and J. Jia, " Investigation of measurement errors in miniature frequency-difference EIT measurement," presented at *the 20th International Conference on Biomedical Applications of Electrical Impedance Tomography*, University College London, London, UK, 2019.
10. **H. Wu**, Y. Yang, P. Bagnaninchi, and J. Jia, "3D cell spheroids drug response monitoring using electrical impedance tomography," presented at *the 19th International Conference on Biomedical Applications of Electrical Impedance Tomography*, University of Edinburgh, Edinburgh, UK, 2018.
11. **H. Wu**, S. Liu, Y. Yang, P. Bagnaninchi, and J. Jia, "Multi-plane electrode configuration for 3D cellular assay of electrical impedance tomography," presented at *the 19th International Conference on Biomedical Applications of Electrical Impedance Tomography*, University of Edinburgh, Edinburgh, UK, 2018.
12. **H. Wu**, Y. Yang, P. Bagnaninchi, and J. Jia, "Towards 3D impedance-based cellular assays with Electrical impedance tomography," presented at *the 4th International Conference on Impedance-Based Cellular Assays*, University of Edinburgh, Edinburgh, UK, 2018.
13. **H. Wu**, Y. Yang, P. O. Bagnaninchi, and J. Jia, "Imaging cell-drug response in 3D bioscaffolds by electrical impedance tomography," presented at *2017 IEEE International Conference on Imaging Systems and Techniques (IST)*, 2017, pp. 1-5.
14. **H. Wu**, Y. Yang, and J. Jia, "A simplified calibration method for multi-frequency EIT system," presented at *the 18th International Conference on Biomedical Applications of Electrical Impedance Tomography*,

Thayer School of Engineering at Dartmouth, Hanover, New Hampshire, USA, 2017.

15. **H. Wu**, Y. Yang, J. Escudero, and J. Jia, "Feasibility Study of Frequency-difference Electrical Impedance Tomography on Industrial Applications," presented at *the 8th World Congress on Industrial Process Tomography*, Iguassu Falls, Brazil, 2016.
16. Y. Yang, **H. Wu**, and J. Jia, "Quasi-2D EIT-optical Dual Modality Sensor for Cellular Imaging," presented at *the 19th International Conference on Biomedical Applications of Electrical Impedance Tomography*, University of Edinburgh, Edinburgh, UK, 2018.
17. Y. Yang, **H. Wu**, and J. Jia, "Simulation study of scaffold 3D cell culture imaging using a miniature planar EIT sensor," presented at *2017 IEEE International Conference on Imaging Systems and Techniques (IST)*, 2017, pp. 1-6.
18. Y. Yang, **H. Wu**, and J. Jia, "Optimal Design of a Planar Miniature EIT Sensor for 3D Cell Imaging," presented at *the 18th International Conference on Biomedical Applications of Electrical Impedance Tomography*, Thayer School of Engineering at Dartmouth, Hanover, New Hampshire, USA, 2017.
19. Y. Yang, **H. Wu**, and J. Jia, "Total Variation and L1 Joint Regularisation for High Quality Cell Spheroid Imaging Using EIT," presented at *the 18th International Conference on Biomedical Applications of Electrical Impedance Tomography*, Thayer School of Engineering at Dartmouth, Hanover, New Hampshire, USA, 2017.

Chapter 1 Introduction

1.1 Background and motivation

3D cell culture is a technique that allows biological cells to grow and interact with the surroundings in three dimensions. Compared with 2D cell culture, 3D cell culture better mimics the behaviour of cells growing in the natural environment and provides more accurate results for cellular assays [1, 2].

However, most of the existing techniques are mainly optimised for 2D cell culture monitoring and they have limitations when adapting for 3D tissue characterisations [3]. Confocal and fluorescence microscopy are popular methods for 2D cell culture characterisations, but they are limited to a penetration depth of few micrometres and therefore not suitable to measure the dense, highly scattering tissues [1]. Alternatively, dye conversion assays, such as MTT assay, are frequently used in biological experiments to evaluate the cell viability, but it is unknown if the reagents used in the assays can penetrate to the centre of the 3D model [4]. Scanning electron microscopy (SEM) and Transmission electron microscopy (TEM) can be used to evaluate large 3D tissues, but they require frozen and fixed samples, so they are only suitable for destructive endpoint studies [5]. Therefore, new measurement techniques are urgently needed to fulfil the requirements of 3D cell culture monitoring, from the perspective of high-penetration, non-destruction and high temporal resolution.

Impedance-based cellular assays are emerging techniques that can assess the quality of engineered tissue and cell-based products [6, 7]. They are defined as a range of methods using microelectrodes to measure the impedance of biological systems to gain information on the cellular behaviour of adherent cell cultures, cell suspensions and 3D tissue models. With the advantages of non-destructive and label-free, impedance-based cellular assays are gradually used in 3D cellular studies, especially for live cell analysis [8, 9] and long-time live-cell monitoring [10, 11]. Existing impedance-based techniques for cellular assays include trans-epithelial electrical resistance

(TEER), electrical impedance spectroscopy (EIS), electric cell-substrate impedance sensing (ECIS) and electrical impedance tomography (EIT).

First developed in 1978 [12], EIT is a tomographic imaging modality to visualise the conductivity distribution or variation within the sensing area [13, 14]. The basic working principle of EIT is to apply electric currents to selected electrodes successively and to measure corresponding boundary voltages at other electrode pairs. The current stimulation and voltage acquisition are carried out until all the non-redundant electrode combinations are deployed. The conductivity distribution or variation can be then obtained from the complete boundary voltage set by solving the inverse problem [15]. Compared with other impedance-based techniques, EIT has a higher spatial resolution but still maintains the high temporal resolution for the measurements.

Previous studies attempted to utilised EIT in the *in-vitro* experiments [16, 17] and found the following challenges before EIT can be applied for practical biological applications:

- Compared with the conventional EIT applications, cellular activities during cell culture result in relatively small perturbations on the boundary voltages, so the measurement noises may overwhelm the signal.
- The feasibility of EIT for long-term real-time monitoring needs to be investigated.
- The theoretical explanation of the correlation between the conductivity images and the biomedical scenarios remains a gap.
- Cross-validation experiments should be performed to evaluate the accuracy of EIT images.

1.2 Aims and objectives

This thesis mainly focuses on exploring and developing the EIT technique for biological applications, with emphasis on the monitoring of 3D tissue culture. Precisely, it aims to exploit time-difference and frequency-difference EIT to

develop adaptable, reliable and reproducible protocols and image reconstruction methods for real-time *in-vitro* monitoring of cell growth and cell viability during cell culture in spheroids and in extracellular matrices. To accomplish the main target, the following objectives are identified:

- Demonstrate the feasibility of time-difference and frequency-difference EIT for 3D tissue characterisation in miniature scale and investigate the optimal settings of miniature EIT for different biological applications.
- Develop physical models to demonstrate the correlation between the physical characteristics of the tissue samples and their conductivity distribution and variation.
- Conduct numerical and experimental studies on the real-time monitoring of 3D cell drug response, from the perspective of the position, shape, concentration and viability of the samples.
- Develop equivalent circuit models to analyse the measurement errors in miniature EIT measurements and investigate an error compensation method for frequency-difference EIT.
- Exploit frequency-difference EIT for long-term tissue culture monitoring utilising the error compensation method.

1.3 Main contributions

This thesis provides pioneering research on the development and optimisation of EIT for 3D tissue culture monitoring. The main contributions of this thesis are summarised as follows:

- The feasibility of miniature EIT for 3D biological tissue imaging was investigated by comparing the reconstructed images with EIS data. Challenges in the miniature EIT experiments were identified. A sub-domain-based reconstruction algorithm was developed to improve the image quality reconstructed from poor measurement signals in order to find the best imaging modality and stimulating frequency.
- A 3D physical model for biological tissues was developed to demonstrate the relationship between the biological characteristics of

the sample with its conductivity distribution. The model is adaptive from tightly packed spheroids to sparsely distributed scaffold samples. It is designed for the process analysis of cell growth and cell-drug response.

- The protocols of EIT for real-time cellular assay was developed and optimised for the monitoring of cell growth and cell-drug response in spheroids and bioscaffolds. It includes the formation of spheroid samples, microporous scaffold samples and hydrogel samples, the measurement procedures and the data processing methods.
- An equivalent circuit model was designed for the error analysis of the miniature EIT measurements. Based on the model, a novel calibration method was derived to eliminate the measurement errors in frequency-difference EIT and to exploit the application of frequency-difference EIT in long-term tissue culture monitoring.
- A joint simulation method was developed to analyse the effect of circuitry errors to the EIT measurements. This method combined the FEM modelling and analogue circuit simulation. An impedance network was developed for the miniature EIT sensor so that it can be analysed through the analogue circuit simulation with fully adjustable circuitry errors on each component.

1.4 Structure of the thesis

The thesis is composed of seven chapters and the remaining part is structured as follows:

Chapter 2 provides an overview of the techniques used in biology to measure impedance. The theory and history of impedance based cellular assays have been introduced. Details discussions include EIT measurements, mathematical problem definition of EIT, image reconstruction algorithms and the settings of miniature EIT for biological applications.

Chapter 3 evaluates the feasibility of EIT for 3D tissue image reconstruction. An initial proof-of-concept experiment is performed to demonstrate the

relationship between image quality and imaging modalities, stimulation frequencies and reconstruction algorithms. The reconstructed images are compared with the true conductivity spectra of the samples to indicate the optimal imaging settings.

Chapter 4 introduces a real-time, label-free and non-destructive method for transient cellular activities using time-difference EIT. An effective medium approximation model is developed to calculate the cell concentration and cell viability of a 3D biological tissue based on its equivalent conductivity. Simulations and experiments with MCF-7 tumour spheroids are conducted to validate this method for cell-drug response monitoring.

Chapter 5 investigates the potential of EIT for tissue engineering applications, where cells are sparsely distributed in stereoscopic space. Two types of bioscaffolds are formed and cultured in the miniature EIT sensor, where time-difference EIT and frequency-difference EIT are used to monitor the cell distribution and the conductivity variation during chemical insult. The advantages and limitations of both methods are discussed by analysing the experimental results.

Chapter 6 demonstrates the method for long-term tissue culture monitoring using frequency-difference EIT. An equivalent circuit model is developed to analyse the impedance artefacts in EIT measurements. The calibration method to eliminate the impedance artefacts has been derived to improve the accuracy of the measured voltage variation. A joint simulation method utilising COMSOL Multiphysics and circuit simulation software is developed to investigate the effect of measurement errors on the boundary voltages. The joint simulation method and practical experiments are then used to evaluate the performance of the calibration method.

Chapter 7 summaries the main finding of this thesis and discusses the limitation of the research. The potential work for the future is also discussed based on the novel developments produced in the thesis.

Chapter 2 Literature review

2.1 Introduction

Bioimpedance is defined as the basic electrical properties of biological cells with regard to the flow of current. Developed in the 1920s, impedance measurement of live biological cells [18] is widely accepted as a label-free, non-invasive and quantitative analytical method to assess cell status. In this chapter, the foundation and development of impedance measurement for live cell analysis were reviewed. As an emerging technique, electrical impedance tomography (EIT) was comprehensively introduced from the perspective of the principles of measurement, the mathematical calculation and the instrumentation for biological applications.

2.2 The foundation of impedance measurement for biological analysis

2.2.1 Electrical properties of a biological cell

The biological cell is a complex heterogeneous entity that contains the plasma membrane, the nucleus and the cytoplasm. The plasma membrane is mainly composed of the lipid bilayer with low ionic permeability, so it can be considered as a low conducting thin shell. If we neglect the dielectric properties of the nucleus, and we consider the cytoplasm as a homogenous conductive material, the cell can be modelled as a conducting sphere covered with an isolating thin layer, which is called the single-shell model (Figure 2-1) [19].

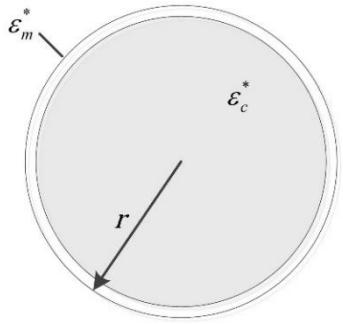

Figure 2-1 The single shell model of a biological cell. ε_m^* and ε_c^* are the complex permittivity of the membrane and the cytoplasm, while *r* is the radius of the cell.

When measuring the complex permittivity spectrum of the biological cell, three distinct dispersions can be observed, named α-dispersion, β-dispersion and γ-dispersion (Figure 2-2). The α-dispersion correlates with the gap junctions and the displacement of counter ions surrounding charged membranes [20, 21]. It ranges between few hertz to several thousand hertz, where the small particles in the extracellular medium start to polarise in the electric field. The β-dispersion is attributed to the interfacial polarisation of the plasma membrane [22, 23]. The frequency range of the β-dispersion is between 10 *kHz* and several hundred *kHz*. The dipolar γ-dispersion is contributed by the reorientation of large molecules, such as proteins and water molecules, and it happens at 1 *GHz* and above [21].

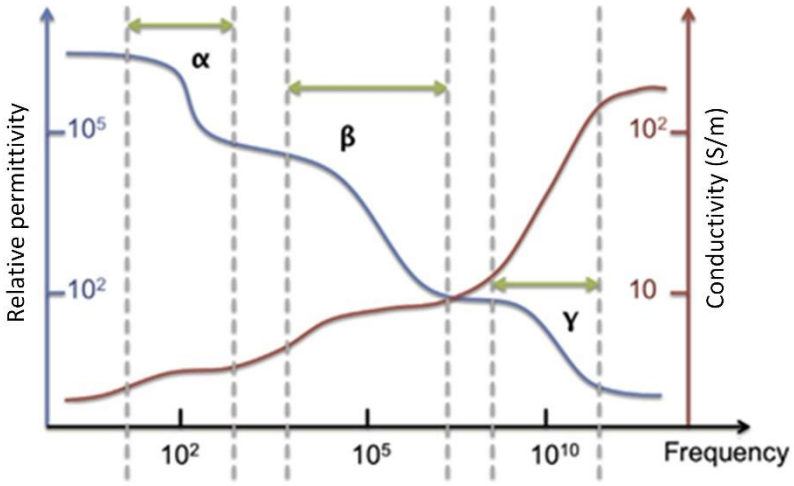

Figure 2-2 Complex permittivity spectrum of the biological cells [24]

2.2.2 Bioimpedance of the tissue sample

Due to the interfacial polarisation, the electric responses of tissue samples depend on the biological cells, extracellular medium and the stimulating frequency [24-26]. The equivalent circuit of a tissue sample should be modelled by at least three components (Figure 2-3) [13]. The extracellular medium is represented as a resistor R_e and the cytoplasm and the cell membranes are modelled by the series of a resistor R_i and a capacitor C_i. The resulting impedance of the whole tissue sample is:

$$Z = \frac{(R_i + \frac{1}{j\omega C_i})R_e}{R_i + R_e + \frac{1}{j\omega C_i}} \qquad \textbf{2-1}$$

where j is the imaginary symbol and ω is the frequency.

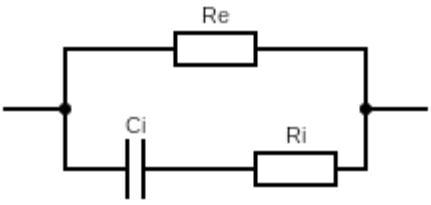

Figure 2-3 The simplest equivalent circuit model of the tissue sample considering the cell membrane, the cytoplasm and the extracellular medium

At lower frequencies, the equivalent impedance of the cell membrane is extremely high, and the current can only flow through the extracellular space (Figure 2-4 (a)). Hence, the equivalent impedance of the sample only depends on the extracellular medium. At higher frequencies, the current can cross both the extracellular medium and the cell membrane (Figure 2-4 (b)), so the equivalent impedance depends on the impedance of the extracellular medium and the electrical properties of the cells.

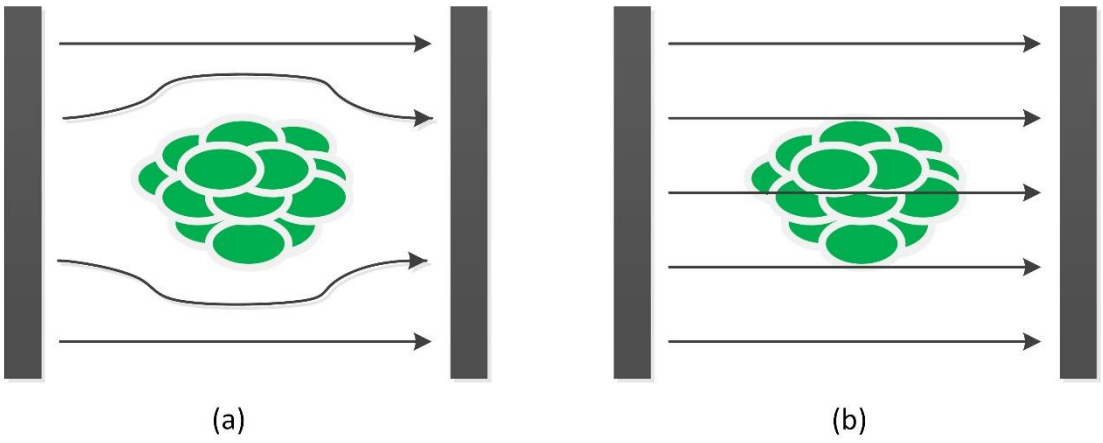

Figure 2-4 The current flow through the tissue sample at (a) low and (b) high frequencies

2.2.3 Impedance measurement strategies for the tissue samples

Bioimpedance can be obtained by injecting a current to the sample and measuring the corresponding voltages. The measurement is usually carried out with either the two-electrode or four-electrode measurement strategy.

In the two-electrode measurement strategy, the current injection and the voltage measurement are carried out from the same pair of electrodes. As demonstrated in Figure 2-5, the current is stimulated from ELE1 to ELE2 while the voltage is measured from the same electrodes. This strategy can be simply implemented and its most sensitive region can be adjusted by modifying the size of the electrodes [27-29]. Therefore, it is widely used in electric cell-substrate impedance sensing (ECIS) where the effects of cells growing on the electrodes are the focus of most concern [30-32]. However, recent studies have found that the impedances of the samples measured with the two-electrode measurement strategy are usually not accurate as it intrinsically includes the contact impedances Z_{c1} and Z_{c2} between the electrodes and the sample [33]. The measured impedance is equal to the sum of the impedance of the sample and the contact impedances (Eq. (2-2)). When the impedance of the sample is small, the measurement error is largely due to the presence of contact impedances.

$$Z_{mea} = \frac{V_{mea}}{I_{mea}} = Z + Z_{c1} + Z_{c2} \qquad \textbf{2-2}$$

This problem was encountered and solved for the first time in 1915 by Frank Wenner [34], who first proposed the four-electrode measurement strategy for minimising the contributions caused by the wiring and the contacts. With this method, the current is injected from ELE1 to ELE2, and the voltage drop on the sample is measured from ELE 3 and ELE4 [35-38]. In the ideal situation, the voltmeter can be considered as open circuit, so the voltage drop at contact impedances Z_{c3} and Z_{c4} is zero, and the measured voltage is the same as the voltage applied on the sample. Therefore, the four-electrode measurement

strategy is more popular in recent studies, and it is applied in the applications of EIS [39, 40] and EIT [41, 42] to measure biological cells and tissues.

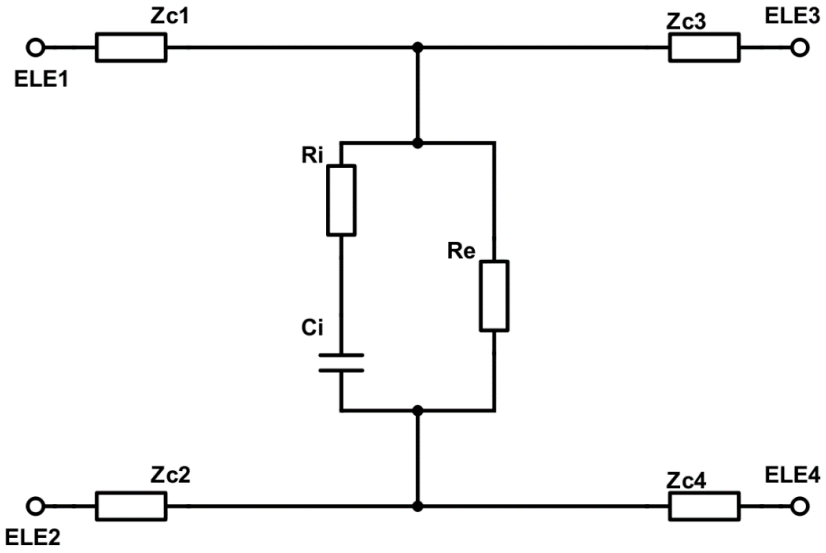

Figure 2-5 Equivalent circuit for the impedance measurement of the tissue sample. Re, Ri, Ci and Zc1 – Zc4 are the impedance of extracellular medium, the impedance of cytoplasm, the capacitance of the cell membranes and the contact impedances at ELE1-ELE4, respectively.

2.3 The development of impedance technology

2.3.1 Electrical impedance spectroscopy

In 1925, Fricke and Morse conducted the first experiment to measure the electric resistance and capacitance of red blood cells [18], where an alternative method for biological analysis was developed. At the early stages, electrical impedance spectroscopy (EIS) was mainly used in the non-invasive analysis of cell characteristics from the cell suspension measurements [43, 44]. Its accuracy was improved following the observation of the distinct dispersion phases in the impedance spectra of biological tissues [45]. These studies were finally summarised into the effective medium approximation theories, such as the Maxwell-Wagner-Hanai, to estimate physical characteristics of the cell suspensions from their dielectric parameters [19, 46]. The theories facilitated EIS to be applied in biological productions, such as in the monitoring of biomass in the fermentation tank and large bioreactor [47-49]. With the

development of microelectrodes, the applications of EIS has branched out into single-cell characterisation [50, 51] and 3D cell culture evaluation [8]. It has been shown to detect the cell cytotoxicity in spheroids [52, 53] and in bioscaffolds [9]. One of the most significant limitations of EIS is it only provide a lumped impedance value for the entire sample instead of the conductivity distribution in a different area [40]. As a consequence, not only the conductivity changes of the samples but also the contact impedance, background changes as well as the deformation of the sample affects the measurement, which make the experiment unrepeatable.

2.3.2 Electric cell-substrate impedance sensing

The impedance spectra measured by EIS are contributed by both the biological cells and culture medium. The electric characteristics of the cells are easily overwhelmed by the contribution of culture medium for the low cell-to-media volume ratio. In the 1980s, Giaever and Keese developed a novel method, named electric cell-substrate impedance sensing (ECIS), to reduce the contribution of the culture medium and increase the sensitivity to the cell activities [54, 55]. ECIS is a real-time and label-free monitoring technology in which a small alternating current (AC) is applied through gold microelectrodes [7]. Based on Maxwell's theory [28], ECIS uses a very small working electrode and a large counter electrode to provide high sensitivity to the impedance changes surrounding the working electrode (Figure 2-6). As a consequence, ECIS is only optimised for the monitoring of adherent cells growing on top of the working electrode and it is not suitable for the monitoring of large cell aggregates. Compared with EIS, ECIS focuses more on the single-cell characterisation and the communication in-between neighbouring cells. Yet, it has been extensively used for a wide range of biological assays including cell membrane integrity [56], cell barrier function [55, 57], cell proliferation [58-60], cytotoxicity [61-63], wound healing [64-66], cell signalling [67, 68] and cell invasion [69].

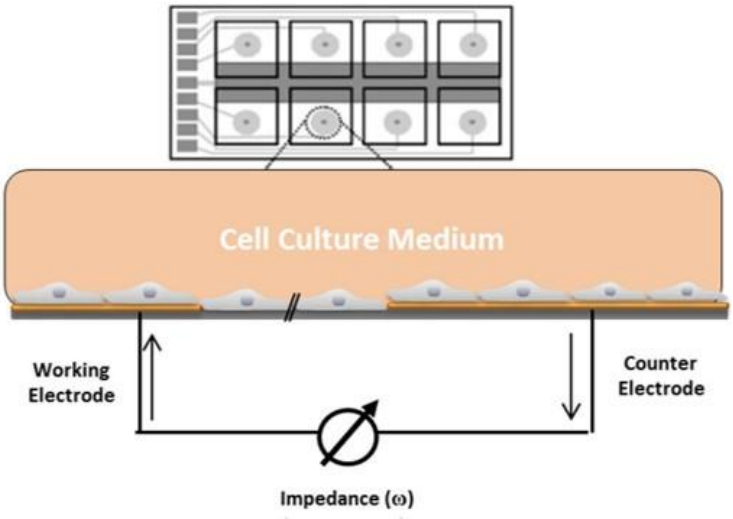

Figure 2-6 Schematic showing the principles of EICS and the design of the ECIS sensor

2.3.3 Electrical impedance tomography

Electrical impedance tomography was first developed in 1978 [12] and was mainly focused on clinical and industrial applications. The main advantage of EIT is that it provides the conductivity distribution instead of a lumped impedance value for the sensing area [40], so it can separate the impedance changes of the background from the contribution of the region of interest. Thorax imaging was one of the most popular EIT applications in the 1980s and 1990s. By measuring the conductivity contrast between air and human tissues, EIT can provide images of cardiac and respiratory changes [70, 71], blood flow [72] as well as tumour localisation [73]. In the 2000s, the combination of multi-frequency EIT measurement improved the spatial resolution and enriched the information containing in the reconstructed images. EIT was then proved to be a potential technique for functional brain imaging and studies were then carried out to analyse the relationship between the real-time conductivity changes with the brain dynamics [74], neural activities [75, 76] and brain diseases such as stroke [77, 78] and epilepsy [79, 80]. Other applications were also developed for the measurement of blood pressure [81] and breast cancer [82, 83]. EIT was first applied for biological applications in 2006, where Linderholm *et al.* tried to monitor the migration of human epithelial stem cells. The spatial

mapping of the electrical properties of *Physarum polycephalum*, a saline mould growing on agar gel, was demonstrated by Sun et al. [84]. Dynamic studies, including cell freezing [16] and cell sedimentation [85], were also reported in recent years. With the development of microelectronics, several designs of miniature EIT sensors for 3D tissue imaging were developed in the latest studies. Liu *et al*. developed and optimised an electrode array for the better imaging of miniature objects in the cubical sensor [86, 87]. In 2016, the gold plated electrodes were implemented on the substrate of the tissue culture dish by Yang *et al.* [88]. Yet, the investigation of miniature EIT is still at the very beginning stage, where researches are mainly focused on the development and optimization of miniature sensor arrays. This study aims to take a step further, investigating and developing protocols for EIT to demonstrate the real-time cellular activities during 3D cell culture.

2.4 The principles of electrical impedance tomography

2.4.1 EIT measurement

The measurement of EIT is developed based on the four-electrode measurement strategy. To calculate the conductivity distribution within the sensing area, both the injected current to a set of electrode pairs and the developed voltages on the other electrode pairs are required. As illustrated in Figure 2-7, the electrodes are commonly distributed on the boundary $\partial\Omega$ of the sensing area Ω. With the most common method, the adjacent drive method [15], the current is applied through an adjacent electrode pair, and the voltages are measured sequentially from all other adjacent electrode pairs without the pairs containing one or both the stimulating electrodes.

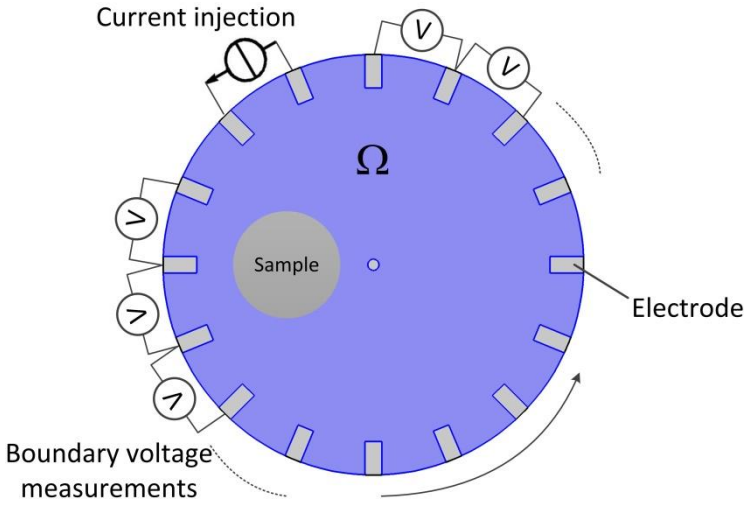

Figure 2-7 Schematic illustration of EIT's adjacent drive measurement principle

2.4.2 EIT imaging modalities

EIT imaging modalities can be differentiated by the combination of data, including time-difference imaging and frequency-difference imaging.

2.4.2.1Time-difference imaging

In the time-difference EIT (TDEIT), the current with a single frequency is injected into the sensor, and the measurements acquired at t_1 are referred to the measurements acquired at reference time t_0:

$$\Delta V = V_{t_1} - V_{t_0} \qquad \text{2-3}$$

This method allows the imaging of time-dependent variation of local conductivity. One of the significant advantages of TDEIT is it can eliminate the effect of instrumentation errors and unknown contact impedance between the electrodes and the background solution.

2.4.2.2Frequency-difference imaging

In the frequency-difference EIT (FDEIT), measurements acquired at f_1, are referred to the reference frequency f_0:

$$\Delta V = V_{f_1} - V_{f_0} \quad \textbf{2-4}$$

This method suppresses the contribution of frequency-independent materials and the modelling error, so it can be used for biological applications where the conductivities of materials are usually frequency-dependent [89]. Compared with TDEIT, FDEIT is more feasible, especially when stable time reference is not available.

After acquiring the boundary voltage vectors through EIT measurement, the reconstruction of conductivity distribution within the sensing area is carried out by solving the forward problem and inverse problem presented in Section 2.4.3 and Section 2.4.4, respectively.

2.4.3 The forward problem

The forward problem of EIT consists of finding the potential u from the knowledge of the complex conductivity distribution σ. The main purpose of solving the forward problem is to calculate the sensitivity of the boundary measurement to the conductivity changes at different positions within the sensing area Ω.This problem can be solved numerically by the finite element method [90], where the conductivity and potential are approximated to the same value within each pixel.

2.4.3.1Maxwell's equations

Once an accurate sensor model is created, the physical conditions imposed at the boundary to the electric field in the interior can be described by Maxwell's equations [91]:

$$\nabla \cdot E = \frac{\rho}{\varepsilon_0} \quad \textbf{2-5}$$

$$\nabla \times E = -\frac{\partial B}{\partial t} \quad \textbf{2-6}$$

$$\nabla \cdot B = 0 \quad \textbf{2-7}$$

$$\nabla \times B = \mu_0 J + \mu_0 \varepsilon_0 \frac{\partial E}{\partial t} \quad \text{2-8}$$

where ρ is the charge density, J is the current density, ε_0 is the electric constant and μ_0 is the magnetic constant.

By assuming a low-frequency current stimulation [92], the change of the magnetic field $\partial B / \partial t$ is considered negligible so that Eq. (2-6) becomes $\nabla \times E = 0$ and $E = -\nabla u$, where u is the electric potential. Therefore, taking the divergence of Eq. (2-8) and using Eq. (2-5) gives the Laplacian equation:

$$\nabla \cdot (\sigma \nabla u) = 0 \quad \text{2-9}$$

For the finite element method, a weak formulation is required [93]. Multiplying Eq. (2-9) by any test function v and integrating over the whole domain Ω gives:

$$\int_\Omega v \nabla \cdot (\sigma \nabla u) = 0 \quad \text{2-10}$$

therefore

$$\int_\Omega \nabla v \cdot (\sigma \nabla u) = \int_{\partial\Omega} v \sigma \frac{\partial u}{\partial n} \quad \text{2-11}$$

which is the weak formulation of the Laplace equation [94].

2.4.3.2 Electrode model

The Dirichlet boundary condition and the Neumann boundary condition are commonly used with the Laplacian equation (Eq. (2-9)) to match the EIT experiment setup, which is also known as the complete electrode model (CEM) [95, 96]. In CEM, the contact impedance z_l between the electrode and the sensing domain is assumed to be a constant, so the boundary voltage V_l is composed of the potential on the electrode and the voltage drop produced by the contact impedance.

$$u + z_l \sigma \frac{\partial u}{\partial n} = V_l \quad (l = 1, 2, ..., L) \qquad \textbf{2-12}$$

where L is the number of the electrode E_l on the surface $\partial\Omega$ and n is normal to the boundary $\partial\Omega$.

The current through the electrode equals the total current density on the electrode area and zero current density is applied to the rest of the surface:

$$\int_{E_l} \sigma \frac{\partial u}{\partial n} dS = I_l \quad (l = 1, 2, ..., L) \qquad \textbf{2-13}$$

$$\sigma \frac{\partial u}{\partial n} = 0 \text{ (The rest of the surface)} \qquad \textbf{2-14}$$

where I_l is the stimulation current on the electrode.

Based on Kirchhoff's law, the current injected to the sensing area and the boundary voltages on the electrodes must follow the following rules:

$$\sum_{l=1}^{L} I_l = 0 \qquad \textbf{2-15}$$

$$\sum_{l=1}^{L} V_l = 0 \qquad \textbf{2-16}$$

The existence and uniqueness of the model have been proved by Somersalo et al. [97].

Assuming the contact impedance is constant at each electrode, the combination of the CEM (Eq. (2-12) to (2-16)) and the weak formulation (Eq. (2-11)) gives:

$$\int_{\Omega} \nabla v \cdot (\sigma \nabla u) = \sum_{l=1}^{L} \frac{1}{z_l} \int_{E_l} v(V_l - u) \qquad \textbf{2-17}$$

Choosing $v = u$ yields:

$$\int_{\Omega}\sigma|\nabla u|^2+\sum_{l=1}^{L}\int_{E_l}z_l\left(\sigma\frac{\partial u}{\partial n}\right)^2=\sum_{l=1}^{L}V_lI_l \qquad \textbf{2-18}$$

2.4.3.3 Sensitivity matrix

The sensitivity matrix, which is also called the Jacobian matrix, defines the relationship between the conductivity change of the k^{th} pixel and the change of boundary measurement $V_{i,j}$:

$$J_k=\frac{\partial V_{i,j}}{\partial\sigma_k} \qquad \textbf{2-19}$$

where the i^{th} and j^{th} electrode pairs are selected as the current stimulation and voltage measurement, respectively.

Assuming small disturbances $\sigma\rightarrow\sigma+\delta\sigma$ and the corresponding disturbances $u\rightarrow u+\delta u$ and $V_l=V_l+\delta V_l$ with current I_l held constant, Eq. (2-18) gives:

$$\int_{\Omega}\delta\sigma|\nabla u|^2+2\int_{\Omega}\delta\sigma\nabla u\cdot\nabla\delta u+2\sum_{l=1}^{L}\int_{E_l}z_l\left(\sigma\frac{\partial u}{\partial n}\right)\delta\left(\sigma\frac{\partial u}{\partial n}\right)=\sum_{l=1}^{L}V_lI_l \qquad \textbf{2-20}$$

when the second-order terms are ignored.

Using the weak formulation Eq. (2-11) with $v=\delta u$ gives:

$$\int_{\Omega}\sigma\nabla u\cdot\nabla\delta u=\int_{\partial\Omega}\delta u\sigma\frac{\partial u}{\partial n} \qquad \textbf{2-21}$$

And applying CEM (Eq. (2-12)) on electrode l yields:

$$\left(\delta\sigma\frac{\partial u}{\partial n}\right)=\frac{1}{z_l}(\delta V_l-\delta u) \qquad \textbf{2-22}$$

Finally, the combination of (Eq. (2-20)), (Eq. (2-21)), (Eq. (2-22)) gives the power perturbation formula:

$$\sum_{l=1}^{L} V_l I_l = \int_{\Omega} \delta\sigma \left|\nabla u\right|^2 \qquad \textbf{2-23}$$

In order to find the voltage disturbance $\delta V_{i,j}$ in a specific measurement, Eq. (2-23) is solved by calculating $u(I_i)+u(I_j)$ and $u(I_i)-u(I_j)$, where $u(I_i)$ is the field generated by applying current I on the i^{th} electrode pair and $u(I_j)$ is the field generated by applying current I on the j^{th} electrode pair. Applying Eq. (2-23) to $u(I_i)+u(I_j)$ and $u(I_i)-u(I_j)$, and subtracting them from each other gives the sensitivity matrix for EIT measurement:

$$J = \frac{\partial V_{i,j}}{\partial \sigma} = -\int_{\Omega} \nabla u(I_i) \cdot \nabla u(I_j) dS \qquad \textbf{2-24}$$

2.4.4 The inverse problem

The EIT image reconstruction attempts to inverse the forward problem to estimate the conductivity distribution from the boundary voltage vectors and the sensitivity matrix:

$$\Delta\sigma = J^{\dagger}\Delta V \qquad \textbf{2-25}$$

However, the solution of Eq. (2-25) does not exist, because J is mostly not invertible. The solution to this problem becomes to minimise the difference between the components on both sides of Eq. (2-25):

$$\Delta\hat{\sigma} = \arg\min_{\Delta\sigma} \frac{1}{2}\left\|J\Delta\sigma - \Delta V\right\|_2^2 \qquad \textbf{2-26}$$

The solution to the least-square problem Eq. (2-26) can be written as:

$$\Delta\hat{\sigma} = (J^T J)^{-1} J^T \Delta V \qquad \textbf{2-27}$$

Since the inversion of $J^T J$ is highly ill-posed, a small noise in the boundary voltage vectors may cause significant error in the estimated conductivity distribution. In order to mitigate the ill-posedness, regularisation-based

reconstruction algorithms are commonly used in image reconstruction. The regularisation introduces information about the solution, commonly called prior knowledge, to the objective function Eq. (2-26) as an additional term:

$$\Delta\hat{\sigma} = \arg\min_{\Delta\sigma}\left(\frac{1}{2}\left\|J\Delta\sigma - \Delta V\right\|_2^2 + \lambda R(\Delta\sigma)\right) \quad \textbf{2-28}$$

where λ is the regularisation parameter, which controls the weight between two terms and $R(\Delta\sigma)$ is the regularisation term.

Some of the most popular EIT image reconstruction algorithms have been well summarised in recent literature reviews [98-100]. Below, a brief review of the image reconstruction algorithms related to this thesis is provided.

2.4.4.1One-step Tikhonov regularisation

Tikhonov regularisation is one of the most commonly used methods for image reconstruction in EIT. The incorporation of the regularisation term is based on the knowledge that the noise is dominated by high-frequency components with large amplitudes. By controlling the norm of the conductivity distribution, it can suppress the large noise components [101]:

$$\Delta\hat{\sigma} = \arg\min_{\Delta\sigma}\left\{\frac{1}{2}\left(\left\|J\Delta\sigma - \Delta V\right\|_2^2 + \lambda\left\|\Delta\sigma\right\|_2^2\right)\right\} \quad \textbf{2-29}$$

By taking the derivative of Eq. (2-29) and let it to zero, the solution is:

$$\Delta\hat{\sigma} = (J^T J + \lambda I)^{-1} J^T \Delta V \quad \textbf{2-30}$$

where I is the identity matrix, which has the same dimension with $J^T J$.

This method can be improved by introducing the Laplacian of Gaussian (LoG) filter to the additional term to reduce the fringe effect in the reconstructed image:

$$\Delta\hat{\sigma} = \arg\min_{\Delta\sigma}\left\{\frac{1}{2}(\left\|J\Delta\sigma - \Delta V\right\|_2^2 + \lambda\left\|L\Delta\sigma\right\|_2^2)\right\} \quad \textbf{2-31}$$

where L is the four-connected region second-order Laplacian operator matrix [102].

Its solution is therefore calculated as:

$$\Delta\hat{\sigma} = (J^T J + \lambda L^T L)^{-1} J^T \Delta V \quad \textbf{2-32}$$

2.4.4.2Non-linear iterative algorithms

Non-linear iterative algorithms propose to iteratively search the global minimum of the objective function Eq. (2-28). At each step, the estimated conductivity distribution is updated to reduce the residual of the objective function until it meets the criteria. The commonly used iterative algorithms include *l1* regularisation [103, 104] and total variation (TV) regularisation [105].

l1 regularisation is based on the knowledge that the conductivity distribution is sparse, which means most of the elements are zero [106]. This prior knowledge can be utilised to emphasise the non-zero conductivity variation and suppress the small noise in the estimated results. In EIT image reconstruction, this can be achieved by controlling the *l1* norm of the conductivity distribution:

$$\Delta\hat{\sigma} = \arg\min_{\Delta\sigma}(\frac{1}{2}\left\|J\Delta\sigma - \Delta V\right\|_2^2 + \lambda\left\|\Delta\sigma\right\|_1) \quad \textbf{2-33}$$

This equation can be solved by several well-investigated methods, such as basis pursuit denoise [107] and the least absolute selection and shrinkage operator [108].

TV regularisation is another regularisation algorithm that is widely used in EIT image reconstruction [105, 109, 110]. It is based on the knowledge that conductivity distribution with unexpected noise has high total variation, reflected in the high integration of the absolute gradient. Therefore, reducing

the total variation of the estimated conductivity distribution, which subjects to the original objective function, reduces the unwanted noise while maintaining the other information in the images, such as the edge. This is achieved by introducing the integral of the absolute gradient of the conductivity distribution to the original objective function as a regularisation term:

$$\Delta\hat{\sigma} = \arg\min_{\Delta\sigma}\left(\frac{1}{2}\left\|J\Delta\sigma - \Delta V\right\|_2^2 + \lambda\left\|\Delta\sigma\right\|_{TV}\right) \quad \textbf{2-34}$$

where $\left\|\Delta\sigma\right\|_{TV}$ is defined as:

$$\left\|\Delta\sigma\right\|_{TV} = \sum_{x,y}\sqrt{(D^{v}_{x,y}(\Delta\sigma))^2 + (D^{h}_{x,y}(\Delta\sigma))^2} = \left\|\nabla(\Delta\sigma)\right\|_1 \quad \textbf{2-35}$$

where (x, y) is the coordinate of the selected pixel, while $D^{h}_{x,y}(\Delta\sigma)$ and $D^{v}_{x,y}(\Delta\sigma)$ are the horizontal and vertical difference operators, respectively:

$$D^{h}_{x,y}(\Delta\sigma) = \begin{cases} \Delta\sigma_{x,y} - \Delta\sigma_{x+1,y} & 1 \le x < n_h \\ 0 & x = n_h \end{cases} \quad \textbf{2-36}$$

$$D^{v}_{x,y}(\Delta\sigma) = \begin{cases} \Delta\sigma_{x,y} - \Delta\sigma_{x,y+1} & 1 \le y < n_v \\ 0 & y = n_v \end{cases} \quad \textbf{2-37}$$

where n_h and n_v are the number of pixels in each line and row, respectively.

The TV regularisation is usually solved by the gradient-based recovery method [111, 112] and the split Bregman method [113].

2.4.4.3Combined regularisation algorithms

In recent studies, combined regularisation algorithms which utilise multiple prior knowledge in image reconstruction have been developed. Compared with the single regularisation algorithms, the combined regularisation algorithms can better demonstrate all the features in the true images by introducing

multiple regularisation terms to the objective functions. They can be generally formulated as:

$$\Delta\hat{\sigma} = \arg\min_{\Delta\sigma}\left(\frac{1}{2}\left\|J\Delta\sigma - \Delta V\right\|_2^2 + \sum_{i=1}^{n}\lambda_i R_i(\Delta\sigma)\right) \quad \textbf{2-38}$$

where $R_i(\Delta\sigma)$ and λ_i are the i^{th} regularisation term and regularisation parameter, respectively.

One type of combined regularisation algorithms apply multiple regularisation terms globally and adjusts the contribution of different terms by tuning the regularisation parameters [114]. For example, He et al. [115] combined the Tikhonov and NOSER regularisation to improve the accuracy of EIT in 3D open-field image reconstruction:

$$\Delta\hat{\sigma} = (J^T J + \lambda_1 I + \lambda_2 diag(J^T J))^{-1} J^T \Delta V \quad \textbf{2-39}$$

The other type of combined regularisation algorithms separates the imaging region into sub-domains through prior knowledge and applies different regularisation terms to constrain the solution in the selected regions. Kang et al. [116] developed a sub-domain-based regularisation (SR) method for human thorax imaging. With the thorax structure obtained from the CT image, the regularisation matrix can be modified anisotropically to include sub-domains as prior information:

$$\Delta\hat{\sigma} = (J^T J + (\lambda_1\Gamma_1 + \lambda_2\Gamma_2 + \lambda_3\Gamma_3))^{-1} J^T \Delta V \quad \textbf{2-40}$$

where Γ_1, Γ_2 and Γ_3 only contains the prior knowledge for the corresponding regions Ω_1, Ω_2 and Ω_3. If the j^{th} pixel locates at the surface of Ω_i, the j^{th} row of the regularisation term $\Gamma_{i,j}$ can be formulated as:

$$\Gamma_{i,j} = [0,...,0,-1,0,...,0,-1,0,...,0,2,0,...,0] \quad \textbf{2-41}$$

where 2 locates at the j^{th} column and -1 locate at the columns for the adjacent pixels within Ω_i.

If the j^{th} pixel locates inside the Ω_i, the j^{th} row of the regularisation term $\Gamma_{i,j}$ is the same as the LoG regularisation:

$$\Gamma_{i,j} = [0,...,0,-1,0,...,0,-1,0,...,0,3,0,...,0,-1,0,...,0] \quad \textbf{2-42}$$

Otherwise:

$$\Gamma_{i,j} = [0,...,0] \quad \textbf{2-43}$$

These methods reduce the effect of background disturbance to the conductivity variation in the region of interest (RoI), and it is also helpful in resolving the local characteristics.

2.5 Sensors and instrumentation for tissue culture imaging

An EIT imaging system for biological imaging is mainly composed of three parts: a miniature sensing unit with the size in several millimetre scales, an impedance measurement unit for current injection and voltage measurement and an image reconstruction unit to process the measurement data [117]. Considering the heating effect to cell culture, the injected current from the EIT imaging system and the placement of sensing electrodes should be strictly controlled [118]. In this thesis, experiments were carried out with the miniature EIT sensor [88] and biomedical imaging system [119] developed at the University of Edinburgh.

2.5.1 Miniature EIT sensor

The miniature EIT sensor was designed based on the structure of the 24-well culture dish with 15 *mm* in diameter and height, respectively. 16 working electrodes are evenly distributed at the boundary of the substrate to increase the sensitivity to the tissues cultured at the bottom and to avoid the severe noise caused by the contact impedance between the electrodes and the tissue samples. The length and width of each working electrode are 1.2 *mm* and 0.6

mm, respectively. A 0.4 *mm* ground electrode is integrated into the middle of the substrate to reduce the DC drift of the measurement caused by the highly conductive cell culture medium [88, 120]. The sensor was manufactured on a printed circuit board. All the electrodes were plated with gold, and the chamber of the sensor was made of quartz glass to prevent corrosion during the experiments.

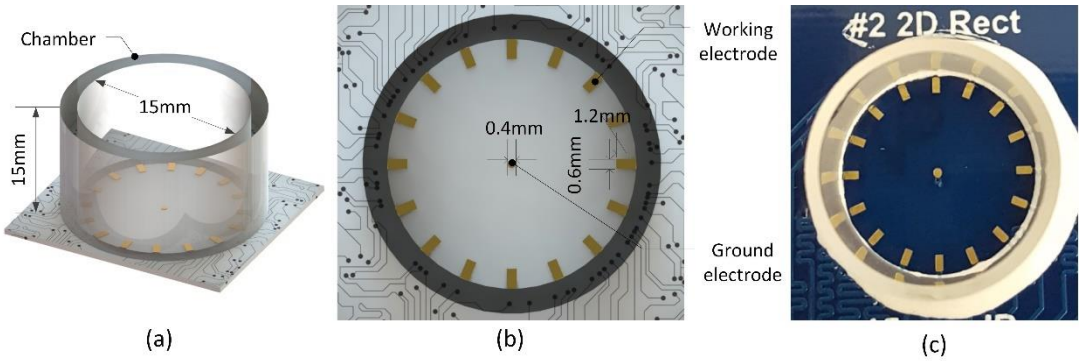

Figure 2-8 Schematic illustration of the miniature EIT sensor

2.5.2 Multi-frequency EIT system with image reconstruction software

The multi-frequency EIT system developed by Yang et al. [121] is an online image reconstruction system specified for biological and biomedical applications. It mainly consists of four parts: the main box utilised for current injection and voltage measurement, a configurable multiplexer array for electrode switching, a 2D/3D imaging software for real-time image reconstruction and data storage and a medical power supply with safety isolation (Figure 2-9).

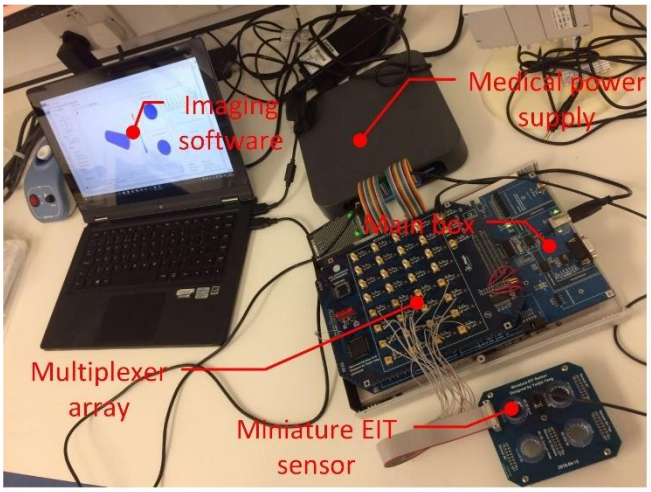

Figure 2-9 Demonstration of the Visual Tomography EIT imaging system

The main box includes an adjustable multi-frequency current source to generate two discrete sinusoidal waveforms with different frequencies from 10 *kHz* to 1 *MHz* and two Analog-to-Digital Converter (ADC) to perform the data acquisition simultaneously. The maximum amplitude of the stimulating current is 10 *mA* peak to peak in order to minimise the effect on the tissue samples.

The configurable multiplexer array is composed of a 32-channel switch array board. In the switch array board, there are 32 dual single pole single throw switches for current injection switching and two cascaded 8×16 crosspoint switch arrays to switch the voltage measuring electrode pairs. The switches are controlled by the imaging software based on EIT's measurement principle (Figure 2-7).

A 2D/3D imaging software, Visual Tomography, is developed for system control and data analysis. It includes a control panel to set the sensing mode and sensing parameters and a window to show the data or reconstructed images for the current measurement. The online image reconstruction is performed with a default sensitivity map and the Tikhonov regularisation method, which are already programmed in the software. For further analysis with different sensitivity matrix or advanced algorithms, the data can be logged to the computer in ".txt" format.

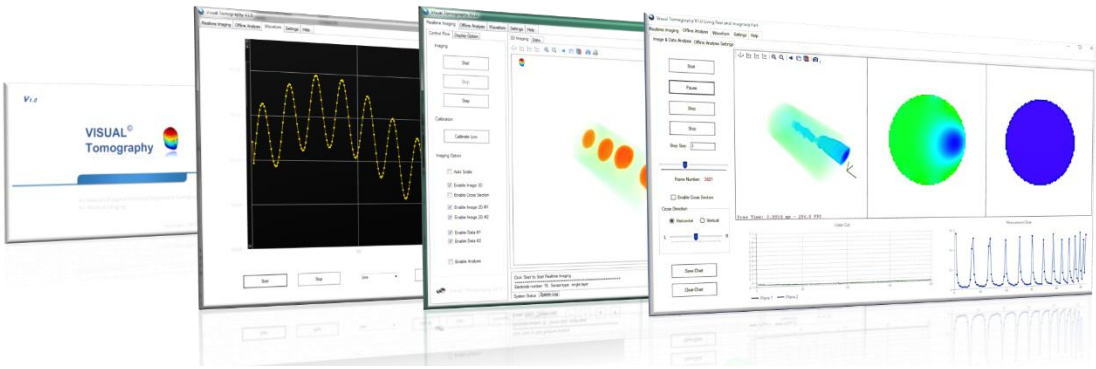

Figure 2-10 Real-time imaging software: Visual Tomography

Phantom tests indicate that the maximum signal to noise ratio (SNR) of this system is 82.82 dB when operating on a 16-electrode sensor with a temporal resolution of more than 100 frames per second (fps). It is, therefore, suitable to be applied in the biological applications to monitor the small conductivity perturbation induced by the transient activities of the biological tissues.

2.6 Summary

This chapter briefly reviewed the theory of bioimpedance measurement and the state-of-the-art impedance techniques for monolayer cellular assays. Considered the limitation of other impedance techniques for 3D tissue characterisation and the advantages of EIT, the need to apply EIT for 3D tissue culture monitoring was highlighted. An overview of the instrumentations for EIT measurement, the measurement schemes as well as the image reconstruction algorithms were then introduced to enable the selection of suitable methods for my study. The innovative work and scientific contributions of the thesis will be presented extensively in the following chapters.

Chapter 3 Miniature EIT for 3D tissue characterisation

3.1 Introduction

Electrical impedance tomography has been widely used in macro tank experiments [77, 122, 123]. It is a convincing technique to separate the biological tissue samples from the background and estimate the electrical properties of the samples [124]. For the purpose of measuring small biological samples, the sizes of the EIT sensors have been reduced to millimetre scale in recent studies [86, 125, 126]. However, most of these sensors were only tested under a single frequency to confirm their ability to show the correct position of the samples. The feasibility of miniature EIT sensors for 3D engineered biological tissue characterisation has not been investigated yet. Compared with the experiments in macro tanks with hundreds millimetre diameter, tissue characterisation in miniature EIT sensor is more challenging due to the limitation of current amplitude and electrode size as well as the effect of high background conductivity and contact impedance [127-129].

This chapter presented a feasibility study of EIT for biological tissue characterisation and image reconstruction. Tissue samples with known conductivity spectra were introduced to the miniature EIT sensor to evaluate the performance of EIT imaging with different measurement modalities, stimulation frequencies and reconstruction algorithms. An improvement has been made to the sub-domain-based regularisation algorithm to increase the accuracy of the sub-domain segmentation. The analysis of the results focused on the image quality and the accuracy of the tissue conductivity in the reconstructed images. The optimal settings of EIT for miniature imaging and the methods to reduce the measuring errors were concluded.

3.2 Methods

3.2.1 Impedance spectroscopy of biological tissues

The electrical properties of tissues samples were measured by EIS using the four-electrode strategy [29]. As shown in Figure 3-1, the samples were cut into

cylinders with 10 *mm* and 40 *mm* in radius and length, respectively. A pair of rectangular stainless-steel electrodes were attached to both sides of the samples as the current stimulation electrodes. The needle-type electrodes were inserted into the samples with a 20mm distance to measure the voltage between the equipotential surfaces [130]. Measurements were carried out with impedance analyser Keysight E4990A, and the frequency range was set between 1 *kHz* and 500 *kHz*. The measured complex impedance is expressed as:

$$Z = Z' + jZ'' \tag{3-1}$$

where Z' and Z'' are the real and imaginary parts of the impedance, respectively.

The complex conductivity of the sample σ was calculated from complex impedance data using the following expression [131]:

$$\sigma = \sigma' + j\sigma'' = |\sigma| \angle \alpha \tag{3-2}$$

$$\sigma' = \frac{l}{A} \cdot \frac{Z'}{Z'^2 + Z''^2} \tag{3-3}$$

$$\sigma'' = \frac{l}{A} \cdot \frac{Z''}{Z'^2 + Z''^2} \tag{3-4}$$

where α is the phase, σ' is the real part, σ'' is the imaginary part, l is the distance between two equipotential surfaces and A is the cross-section area.

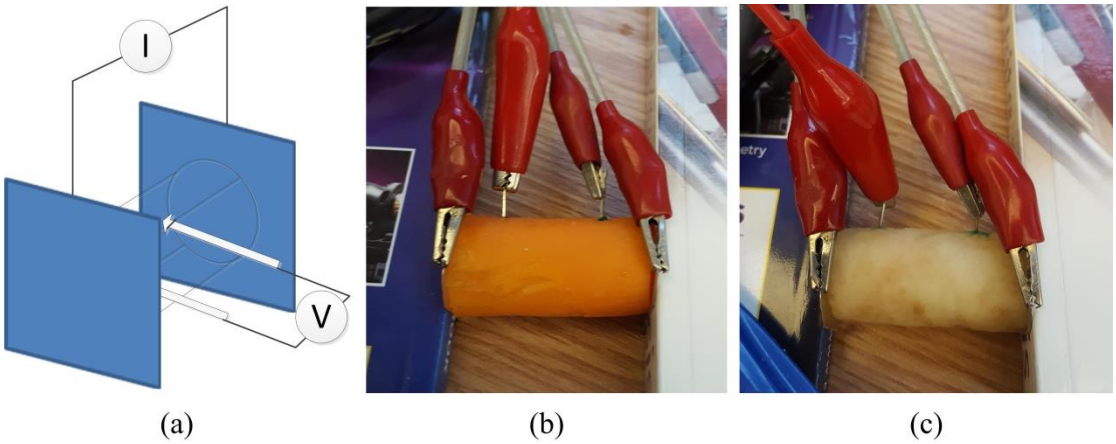

Figure 3-1 The conductivity measurement (a) schematic diagram as well as the experimental setup for (b) carrot tissue measurement and (c) potato tissue measurement

3.2.2 Sensor optimisation

In order to reduce the impedance artefacts in the EIT measurement, the accordion was applied to balance the track impedance between different channels. Figure 3-2 shows two designs of miniature EIT sensor with the same electrode pattern. In the design without the accordion, the trace length was mainly determined by the distance between the socket and the electrode, so the track impedance varied between channels. The accordion minimised the difference in trace length among all 16 channels and resulted in a more identical track impedance (Figure 3-3).

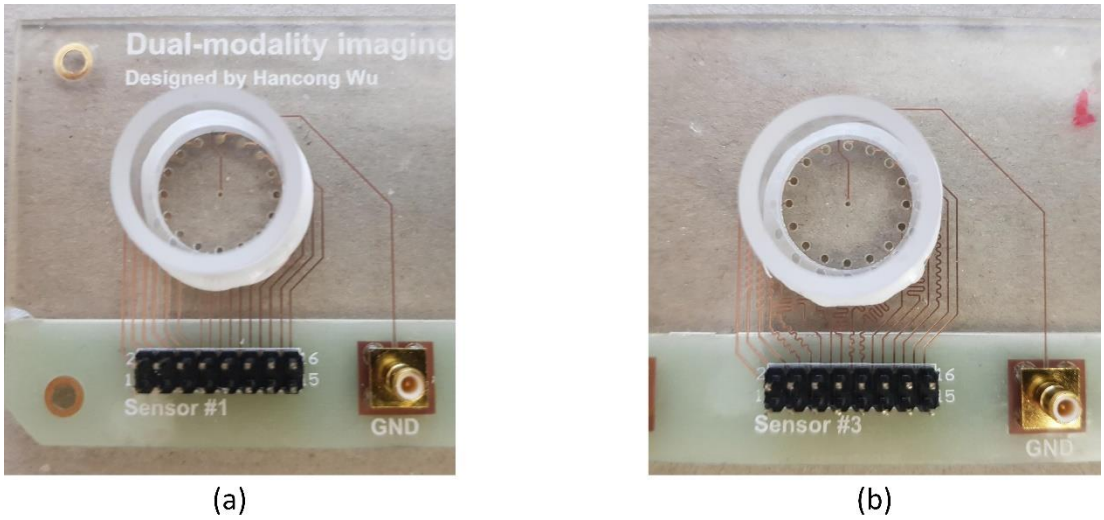

Figure 3-2 Miniature EIT sensor (a) without and (b) with accordion

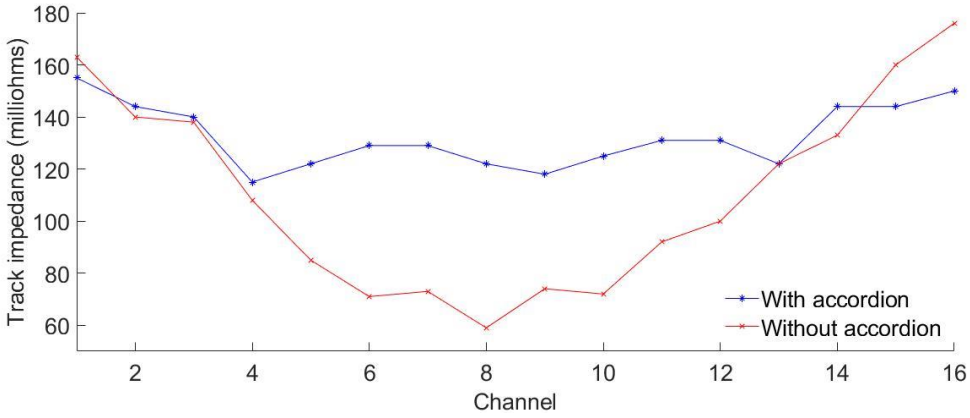

Figure 3-3 The track impedance of each measurement channels on the sensor

3.2.3 Impedance measurements in the miniature EIT sensor

The phantom experiments were carried out with both the miniature EIT sensor demonstrated in Section 2.5.1 and tissue samples with known electrical properties to evaluate the performance of EIT for miniature tissue sample monitoring. The carrot and potato were prepared into small cylindrical samples with 4 *mm* and 7 *mm* in diameter and height, respectively (Figure 3-4(a)). Salt was added to the tap water to prepare the saline with a conductivity of 0.1 *S/m*, which was used as a background reference in the experiment.

During the experiments, a $1\,mA$ current was injected to the sensor using the adjacent drive method. The frequencies were acquired in the range between 10 *kHz* to 100 *kHz* with a 10 *kHz* interval. 1 *ml* saline was first added to the sensor, and the resulting reference voltages were recorded as V_{r1} for 10 *kHz*, V_{r2} for 20 *kHz*, … , and V_{r10} for 100 *kHz*. The tissue samples were then added to the sensor between the electrode 2 to 4 (Figure 3-4(b) (c)). The boundary voltages $V_1, V_2, ..., V_{10}$ were measured under the same frequencies. In time difference imaging, the voltage variation was calculated between the reference voltages and the boundary voltages for the samples under the same frequency using Eq. (2-3). In frequency-difference imaging, the reference was taken from the boundary voltages for the samples at 10 *kHz,* and the voltage variation was calculated between the reference and the boundary voltages for the samples at the selected frequency. In order to eliminate the common modelling error,

the weighted method was adopted [122]. After the calculation, the voltage variation array $[\Delta V_1, \Delta V_2, \cdots, \Delta V_m]$ was obtained.

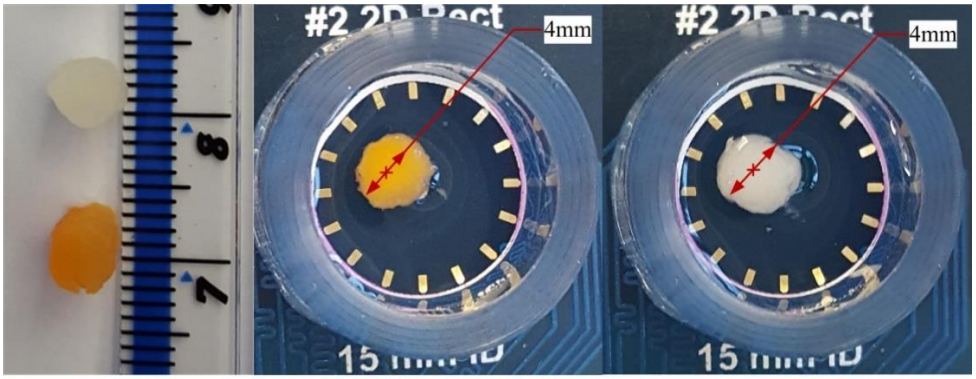

Figure 3-4 (a) Experiment phantom with (b) carrot sample and (c) potato sample

3.2.4 Development of the sensitivity matrix

In the miniature EIT sensor, the currents are stimulated from the bottom electrodes, generating electric fields in the 3D space. If the volume of the culture medium is known, Eq. (2-24) can be modified to the 3D version to calculate the sensitivity of the voxels below the liquid surface.

$$J_k = \frac{\partial V_{i,j}}{\partial \sigma_k} = -\int_{voxel\ k} \nabla u_k(I_i) \cdot \nabla u_k(I_j) dV \qquad \textbf{3-5}$$

where $\nabla u_k(I_i)$ is the real electrical potential at the k^{th} voxel by the injection pattern I_i and $\nabla u_k(I_j)$ is the fictional electrical potential at the k^{th} voxel if the current is stimulated with the pattern I_j.

In this chapter, a cylindrical sensor with 15 *mm* diameter was developed for the sensitivity calculation. Since the introduction of the samples would increase the total volume of inclusion in the sensor, the height of the sensing area was set to 7 *mm* (Figure 3-5 (a)). The sensor was separated by a cuboid mesh while the length and width of the voxel were 0.234 *mm* and the height of the voxel was 0.35 *mm*. Therefore, the sensor was separated into 20 layers with 3228 voxels in each layer (Figure 3-5 (b)). Considered that the samples were

mainly distributed at the bottom of the sensor due to the gravity effect, utilising the sensitivity matrix at the lower layers can better demonstrate the horizontal conductivity distribution of the samples. Therefore, the sensitivity matrix at the bottom layer was applied for the image reconstruction in this study (Figure 3-5 (c)).

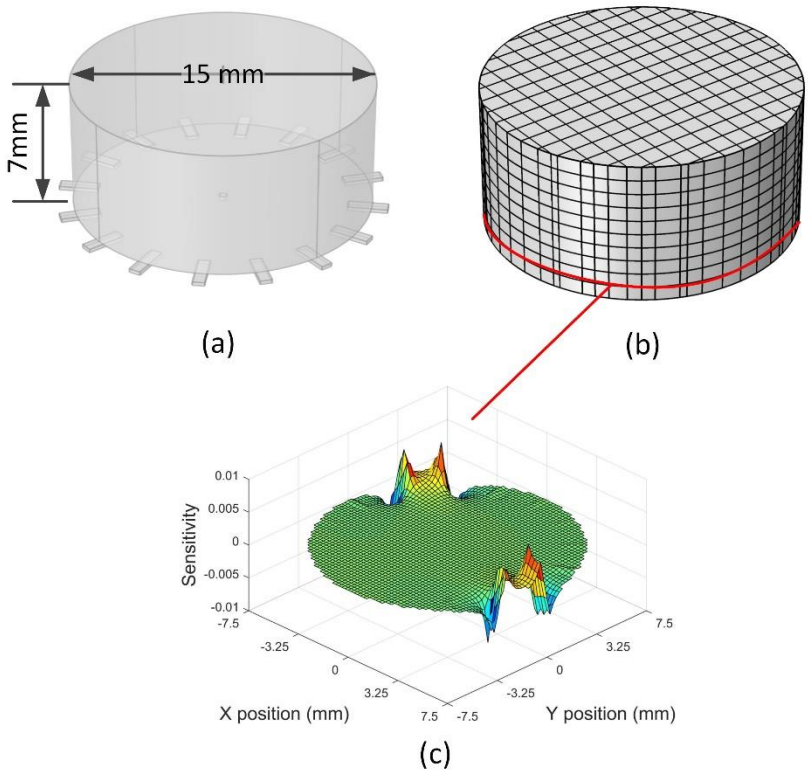

Figure 3-5 The schematic diagram of (a) sensor model, (b) mesh for inverse problem calculation and (c) the sensitivity matrix of opposite impedance measurement

3.2.5 Spectra sub-domain-based regularisation

Images in this chapter were reconstructed with the sub-domain based combined regularisation method. To obtain the structural information, the thresholding method was applied to segment the imaging area into the region of interest (RoI) and the background area. Since the image quality with this method highly depended on the accuracy of the sub-domain, the measurements at all frequencies were utilised for the sub-domain

segmentation, named the spectra sub-domain-based regularisation method (SSR).

The blurred images for conductivity variation spectra were first reconstructed with the one-step Tikhonov regularisation algorithm, which provides the initial information for the location of tissue samples. In each image, the levels of conductivity variation in the rough image with N pixels were sorted in ascending order $[l_1, l_2, ..., l_L]$, and it was separated into two groups A and B, where group A was from $[l_1, l_2, ..., l_k]$ and group B was from $[l_{k+1}, l_{k+2}, ..., l_L]$. Since the probability distribution of the i^{th} level p_i is equal to the number of pixels at that level n_i over the total number of pixels N (Eq. (3-6)), the probability of two groups' occurrence ω_A and ω_B can be represented by Eq. (3-7). Then the class mean level, the class variance and the between-class variance were provided by Eq. (3-8) to Eq. (3-10), respectively. By maximizing the between-class variance [132], the optimal threshold k^* was derived to separate the area with obvious conductivity change from the area with static conductivity. The pixels with obvious conductivity change were defined as the RoI of this image with a weighted parameter $w_{x,y} = 1$, where x indicated the x^{th} frequency and y indicated the y^{th} pixel in the image. The rest of the pixels were considered as the background area with a weighted parameter $w_{x,y} = 0$.

$$p_i = n_i / N,\ p_i > 0, \sum_{i=1}^{L} p_i = 1 \qquad \textbf{3-6}$$

$$\begin{cases} \omega_A = \sum_{i=1}^{k} p_i = \omega(k) \\ \omega_B = \sum_{i=k+1}^{L} p_i = 1 - \omega(k) \end{cases} \qquad \textbf{3-7}$$

$$\begin{cases} \mu_A = \sum_{i=1}^{k} l_i p_i / \omega_A \\ \mu_B = \sum_{i=k+1}^{L} l_i p_i / \omega_B \end{cases} \quad \textbf{3-8}$$

$$\begin{cases} \delta_A^2 = \sum_{i=1}^{k} (l_i - \mu_A)^2 p_i / \omega_A \\ \delta_B^2 = \sum_{i=1}^{k} (l_i - \mu_B)^2 p_i / \omega_B \end{cases} \quad \textbf{3-9}$$

$$\delta_{between}^2 = \omega_A \omega_B (\mu_A - \mu_B)^2 \quad \textbf{3-10}$$

$$k^* = \underset{1 \le k < L}{\operatorname{argmax}} \, \delta_{between}^2 \quad \textbf{3-11}$$

It was assumed that the tissue samples should have different electrical properties with the background solution. Therefore, if a pixel located at the high conductivity variation domain at more frequencies, it was more likely to be the region of samples. In order to avoid the effect of fringe effect and background noise to the selection of the RoI, a filtering method was developed to prevent the pixels, which less likely to be the region of samples, been selected in the RoI

$$r_y = \max\{\sum_{x=1}^{m} w_{x,y} - t, 0\}, \ for \ y = 1, 2, \ldots, N \quad \textbf{3-12}$$

$$\begin{cases} pixel_y \in \Omega_1, \ if \ r_y > 0 \\ pixel_y \in \Omega_2, \ otherwise \end{cases} \quad \textbf{3-13}$$

where $w_{x,y}$ is the weight of the y^{th} pixel at the x^{th} frequency, t is the threshold value, Ω_1 is the RoI and Ω_2 is the background area. If the y^{th} pixel is in the RoI of the image at the x^{th} frequency, $w_{x,y}$ is 1. Otherwise, $w_{x,y}$ is set to 0.

The fine image reconstruction with SSR was then carried out with Eq. (3-14).

Table 3-1 Spectra sub-domain-based regularisation method (SSR)

Input: Voltage variation array $[\Delta V_1, \Delta V_2, \cdots, \Delta V_m]$; threshold value *t*

Step 1: Reconstruct the blurred image $\Delta\tilde{\sigma}_1, \Delta\tilde{\sigma}_2, \cdots, \Delta\tilde{\sigma}_m$ for the voltage variation array using one-step Tikhonov regularisation.

Step 2: Calculate the weighted parameter $w_{x,y}$ for $y = 1, 2, \ldots, N$ pixel at frequency $x = 1, 2, \ldots, m$.

Step 3: Thresholding the imaging area using Eq. (3-12) and Eq. (3-13).

Step 4: Reconstruct the fine images $\Delta\hat{\sigma}_x$, *for* $x = 1, 2, \ldots, m$ using Eq. (3-14)

Output: The fine image spectra $[\Delta\hat{\sigma}_1, \Delta\hat{\sigma}_2, \ldots, \Delta\hat{\sigma}_m]$

$$\Delta\hat{\sigma}_x = (J^T J + \mu_1\Gamma_1 + \mu_2\Gamma_2)^{-1} J^T \Delta V_x, \ for\ x = 1, 2, \cdots, m \qquad \textbf{3-14}$$

where J is the sensitivity matrix, which demonstrates the sensitivity of EIT measurement to the conductivity change at the bottom layer of the sensor at Figure 2-8, $\Gamma_1 = R_1^T R_1$ is the Laplacian operator for quadrate pixels located at RoI Ω_1 and $\Gamma_2 = R_2^T R_2$ is the identity operator for pixels located at the background Ω_2.

$$R_{1,j} = [0, \ldots, 0, -1, 0, \ldots, 0, -1, 0, \ldots, 0, 4, 0, \ldots, 0, -1, 0, \ldots, 0, -1, 0, \ldots, 0] \qquad \textbf{3-15}$$

where 4 is at the j^{th} column if the j^{th} pixel locates at RoI Ω_1 and -1 locate at the columns for its adjacent pixels.

$$R_{2,j} = [0, \ldots, 0, 1, 0, \ldots, 0] \qquad \textbf{3-16}$$

where 1 is at the j^{th} column if the j^{th} pixel locates at RoI Ω_2.

The detailed implementation of SSR is demonstrated in Table 3-1.

3.2.6 Evaluation of image reconstruction performances

To quantitatively evaluate the performance of EIT with different modalities, stimulation frequencies and reconstruction algorithms, the correlation coefficient (CC) and position error (PE) between the true image and the reconstructed conductivity variation are calculated [98, 133].

Position error describes the difference between the centre of the true object R_0 and the centre of the reconstructed object R_r. PE should be as small as possible so that the tissue sample locates closer to its true position.

$$PE = |R_0 - R_r| \qquad \textbf{3-17}$$

Correlation coefficient demonstrates the similarity between the true conductivity distribution and the reconstructed image, which is calculated with the following equation:

$$CC = \frac{\sum_{j=1}^{n}(\Delta\hat{\sigma}_j - \Delta\bar{\hat{\sigma}})(\Delta\sigma_j - \Delta\bar{\sigma})}{\sqrt{\sum_{j=1}^{n}(\Delta\hat{\sigma}_j - \Delta\bar{\hat{\sigma}})^2 \sum_{j=1}^{n}(\Delta\sigma_j - \Delta\bar{\sigma})^2}} \qquad \textbf{3-18}$$

where $\Delta\hat{\sigma}_j$ and $\Delta\sigma_j$ denote the reconstructed and true conductivity variation in the j^{th} pixel while $\Delta\bar{\hat{\sigma}}$ and $\Delta\bar{\sigma}$ are the mean values of $\Delta\hat{\sigma}$ and $\Delta\sigma$, respectively. A higher CC means the shape of the reconstructed image is more similar to that of the true images.

3.3 Results

3.3.1 Conductivity spectra of tissue samples

Figure 3-6 shows the electrical properties of carrot and potato at different frequencies. In general, both the real part of the conductivities of the carrot tissues and potato tissues are relatively invariant at frequencies lower than 10 *kHz*, and they increase exponentially until 500 *kHz*. The imaginary part of the conductivities starts to grow at 4 *kHz* in the sigmoid shape, and the abrupt change regions for both tissues locate between 10 *kHz* and 200 *kHz*. Based

on the dispersion theory, the conductivity variations below 10 *kHz* are mainly associated with the diffusion processes of ionic species, and the conductivity variations between 10 *kHz* and 500 *kHz* are more likely correlated with the cellular membrane potential and the displacement of counter ions surrounding charged membranes [46]. This means the diffusion processes of ionic species only results in the changes in the imaginary part of the conductivities, although the variation in the membrane potential affects both the real and imaginary part of the conductivities. The magnitude of the complex conductivities increases in the exponential shape between 4 *kHz* and 500 *kHz* and their changes are easier to be observed than both the real and imaginary part. Hence, using the complex conductivity not only allows EIT to detect both the diffusion processes of ionic species and changes in cellular membrane potential but also emphasises the changes of the samples. It can be seen that the conductivity of carrot and potato is above 0.1 *S/m* at 80 *kHz* and 38 *kHz*, respectively.

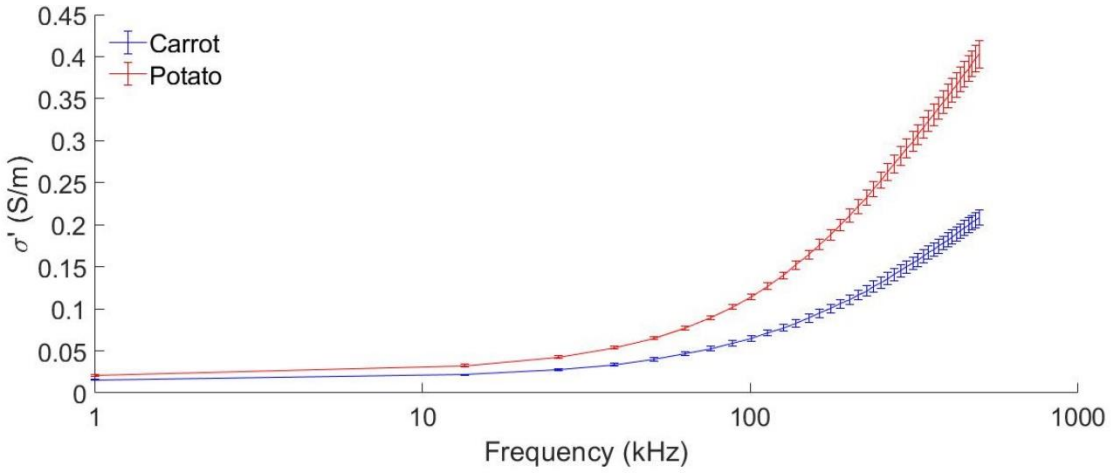

(a)

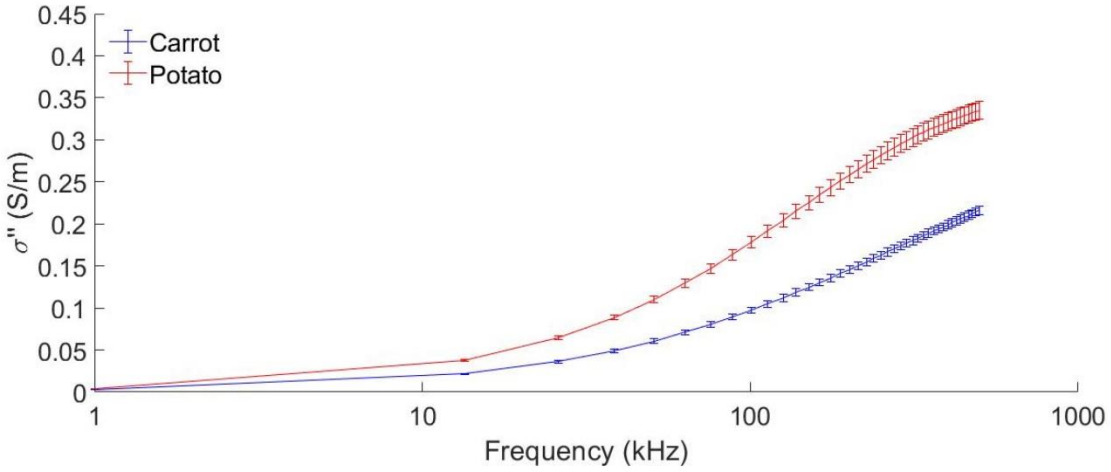

(b)

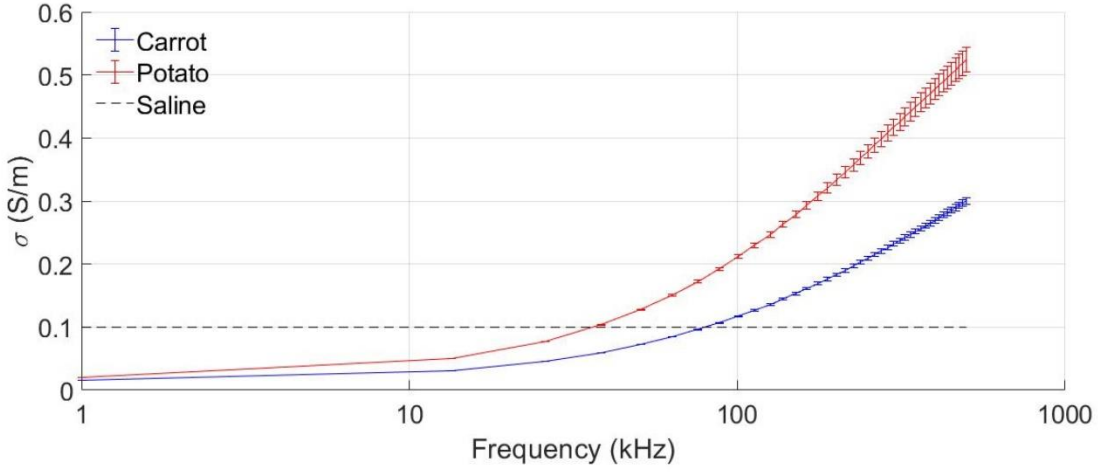

(c)

Figure 3-6 Electrical properties of carrot and potato, the error bar shows the standard variation between samples

3.3.2 Comparison of reconstructed images

Image reconstruction was carried out with the one-step Tikhonov regularisation with LoG filter (TLoG) (Eq. (2-32)), sub-domain regularisation (SR) (Eq. (2-40)) and the proposed spectra sub-domain-based regularisation (SSR)(Eq. (3-14)). The time-difference and frequency-difference images for carrot and potato tissue samples are shown in Figure 3-7 to Figure 3-10, respectively.

In Figure 3-7, the images for carrot tissues show the conductivity of the sample is lower than that of the background below 50 *kHz* with TLoG and SR. At 60 *kHz* and above, the images are blurry and unexpected anomalies are presented in the images. The images reconstructed with SSR correctly indicate the conductivity increase of carrot tissue from 10 *kHz* to 100 *kHz*, but they experience a notable image distortion at 80 *kHz* and above.

Figure 3-8 shows the time-difference images for the potato sample in the saline solution. Compared with the carrot sample, the potato sample has a higher conductivity, and it turns red at 40 *kHz* and above. Images reconstructed with SR and SSR suffer from smaller fringe effect comparing with the images reconstructed with TLoG, but they fail to demonstrate the conductivity of potato sample at 30 *kHz*, where the conductivity of the sample is almost the same as the background conductivity. The most significant conductivity variation of the sample appears at 10 *kHz* and 100 *kHz*.

Figure 3-9 and Figure 3-10 show the frequency-difference images for carrot tissue and potato tissue, respectively. The images show the conductivity variations of the tissues increase when the frequency rises, and the potato tissue sample has a more significant conductivity variation than that of the carrot tissue sample. Compared with the time-difference images, the frequency-difference images have more homogeneous backgrounds, and the deformation of the samples is inconspicuous. It is also noticed that the tissue samples reconstructed in the frequency-difference images are closer to the centre of the sensor than those in the time-difference images.

The images indicate that both tissues are more conductive at higher frequencies, and the potato tissues have a more significant conductivity change than the carrot tissues. The main reason for the conductivity change is the poorly conducting cell membrane, which separates the cytoplasm and extracellular fluid [134]. The cell membrane behaves like a capacitor, and it takes time to charge the membrane placed in the electric field. The time constant of this process is determined by the cell radius, the membrane capacitance and the fluid resistivities, so the conductivities of the cells vary in different frequencies, and different kinds of cells have respective conductivity at the same frequency [45].

In order to show the conductivity spectra of tissues in the images, saline solution with 0.1 *S/m*, whose conductivity is almost frequency independent within my scope [135], was used as the background in the sensor. Uniform colour bars were applied to the images reconstructed at different frequencies to better demonstrate the conductivity changes between frequencies. Overall, most of the images provide the same results as the conductivity spectra measured by the impedance analyser. The key factor determining the image quality is the contrast between the conductivity variation of the tissue samples and the conductivity of the background solution. In TDEIT, the quality of reconstructed images is highly dependent on the conductivity difference between the background and the samples. With a frequency-independent background, the frequency-different images are more accurate when the conductivity variation of the samples are larger.

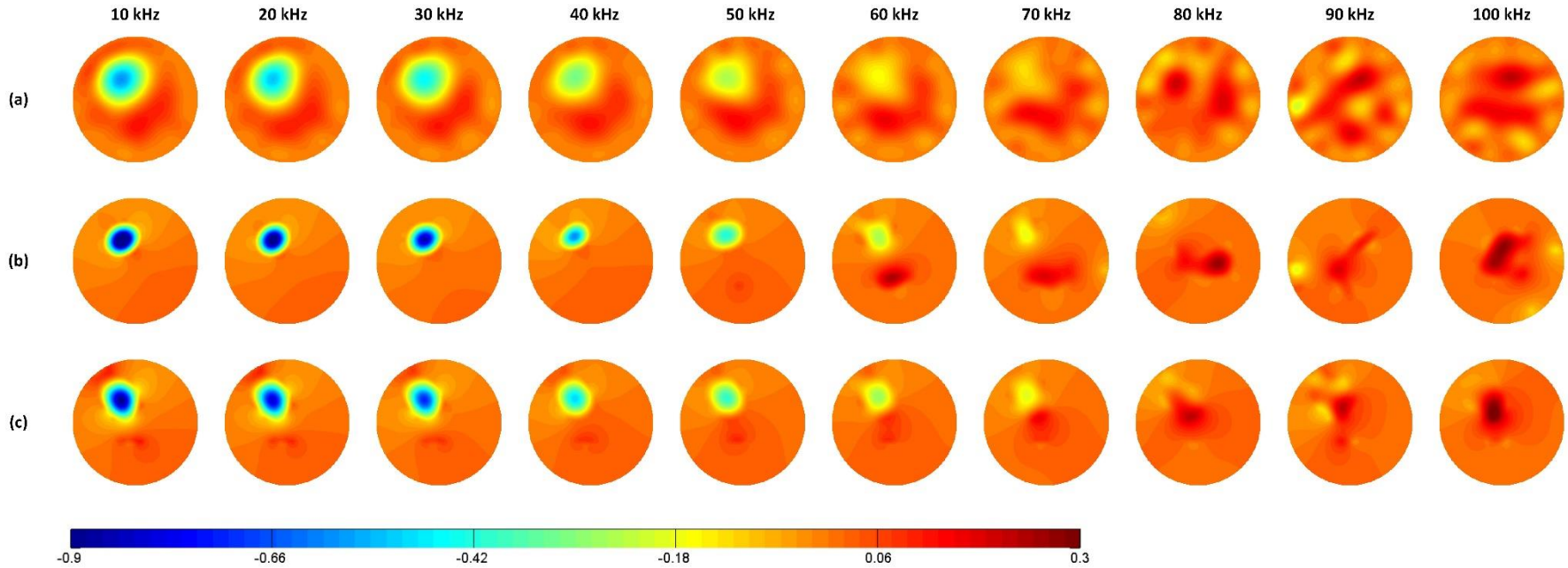

Figure 3-7 Time-difference images for carrot tissue reconstructed with (a) one-step Tikhonov regularisation with LoG filter, (b) sub-domain regularisation and (c) spectra sub-domain-based regularisation

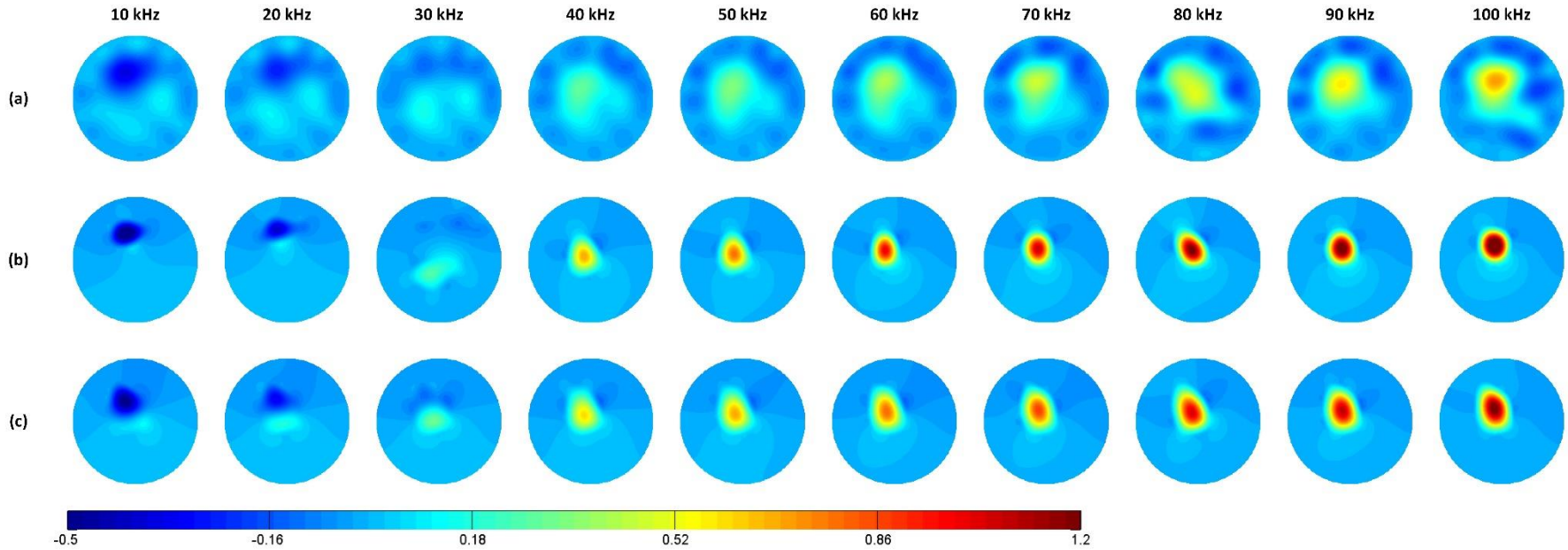

Figure 3-8 Time-difference images for potato tissue reconstructed with (a) one-step Tikhonov regularisation with LoG filter, (b) sub-domain regularisation and (c) spectra sub-domain-based regularisation

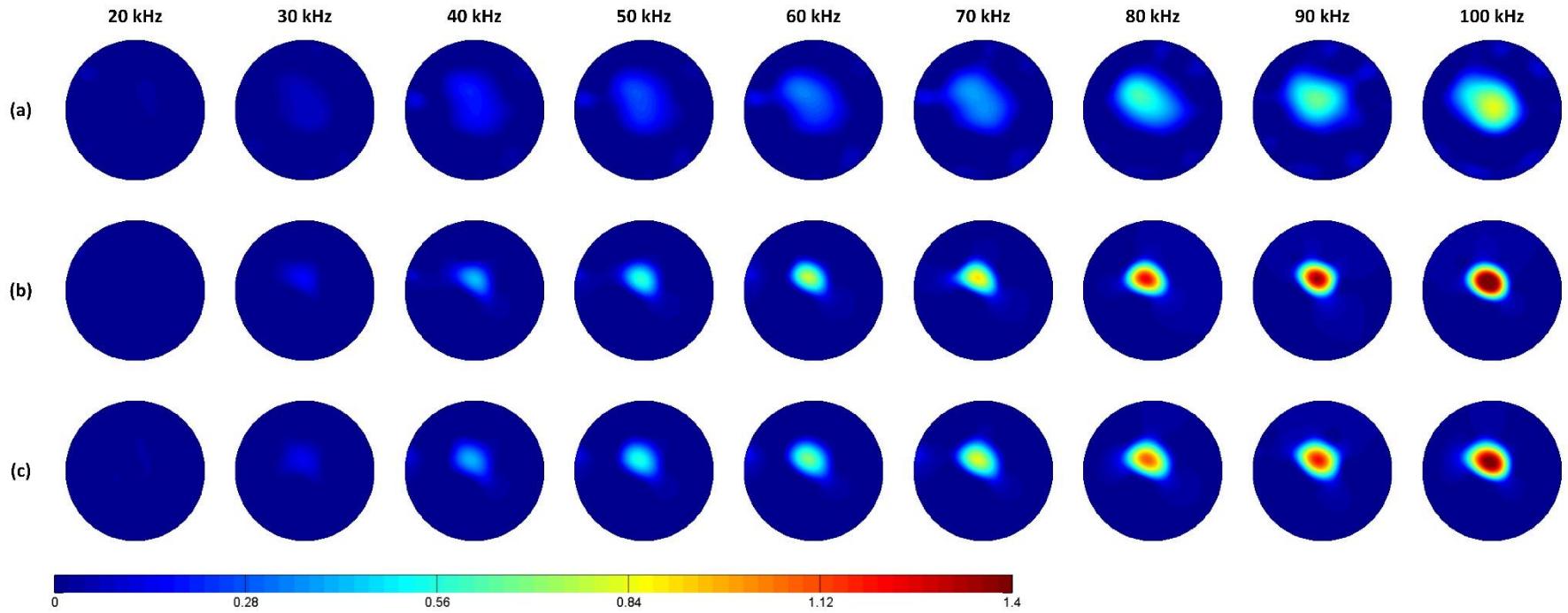

Figure 3-9 Frequency-difference images for carrot tissue reconstructed with (a) one-step Tikhonov regularisation with LoG filter, (b) sub-domain regularisation and (c) spectra sub-domain-based regularisation

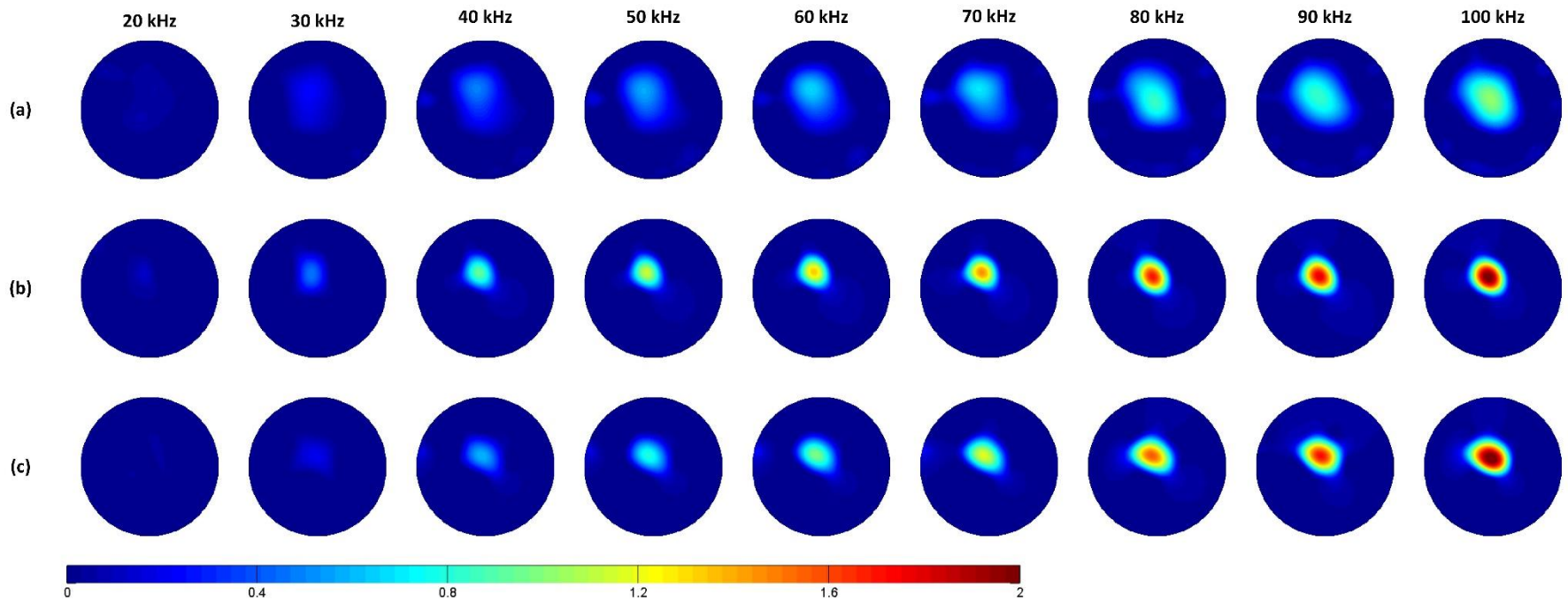

Figure 3-10 Frequency-difference images for potato tissue reconstructed with (a) one-step Tikhonov regularisation with LoG filter, (b) sub-domain regularisation and (c) spectra sub-domain-based regularisation

3.3.3 Evaluation of position error

Figure 3-11 (a) shows the position errors (PEs) of the time-difference images for carrot tissue sample against stimulation frequencies. When the stimulating frequency is lower than 60 *kHz*, the PEs maintain at about 1 *mm* for the image with different reconstruction algorithms. The PEs of the images with TLoG and SR fluctuate between 70 *kHz* and 100 *kHz*, reaching the maximum value at 5.15 *mm* and 3.59 *mm*, respectively. Images with SSR have relatively stable PEs within the measuring scope, and the maximum value is 2.17 *mm* occurring at 80 *kHz*. The PEs below 60 *kHz* are mainly attributed to the modelling errors and the reconstruction errors, so they barely change if the boundary voltage variation corresponding to the carrot tissue sample is much larger than the measurement noise. At a frequency between 70 *kHz* and 100 *kHz*, the conductivity of the carrot tissue is similar to that of the background solution, so the corresponding voltage changes are small, which are easily overwhelmed by the measurement errors. As a consequence, the reconstructed images have poor image quality and large PEs. The accurate sub-domain selection of the SSR helps to penalise part of the background noise and maintain the reconstructed tissue sample at the correct domain, so PE is smaller at the critical frequencies.

The PEs of the time-difference images for potato sample are plotted in Figure 3-11 (b). For the three selected reconstruction algorithms, the PEs are between 1 *mm* and 2 *mm* at all frequencies except 30 *kHz*. Maximum PEs for TLoG, SR and SSR are 3.09 *mm*, 3.71 *mm* and 2.5 *mm*, respectively, and they all occur at 30 *kHz* where the conductivity of the potato tissue is almost the same as the saline. The TLoG provides relatively small PEs between 40 *kHz* and 70 *kHz*, but PEs of the images with SSR have the smallest fluctuation between frequencies. The smallest PE is provided by SSR with the measurement at 10 *kHz*.

Figure 3-11 (c) and Figure 3-11 (d) indicate that the PEs of frequency-difference images are also between 1 *mm* to 2 *mm* when the frequency change is larger than 30 *kHz*. The PEs of the images highly depend on the conductivity

variation of the samples between two measuring frequencies, but the utilisation of the SSR allows relatively lower PEs when the conductivity variation is small.

In summary, these results show that the conductivity variation of the tissue sample between the reference and the measurement is the key factor in reducing the PE. The threshold between high PEs and low PEs of the time-difference images for carrot tissue sample and potato tissue sample locate at 60 *kHz* and 50 *kHz*, respectively. The corresponding conductivity variation between the samples and the saline are 0.018 *S/m* and 0.027 *S/m*, which can be considered as the sensitivity of TDEIT in this miniature EIT sensor. In FDEIT, the lowest frequencies to reconstruct images with low PEs are 40 *kHz* and 30 *kHz* for carrot tissue sample and potato tissue sample, respectively. The conductivities of the samples are 0.035 *S/m* and 0.048 *S/m* higher than their conductivities at 10 *kHz*. Using different one-step algorithms does not significantly affect the PEs when the conductivity variations of the tissue samples are large enough, but a better reconstruction algorithm reduces the PEs at critical frequencies.

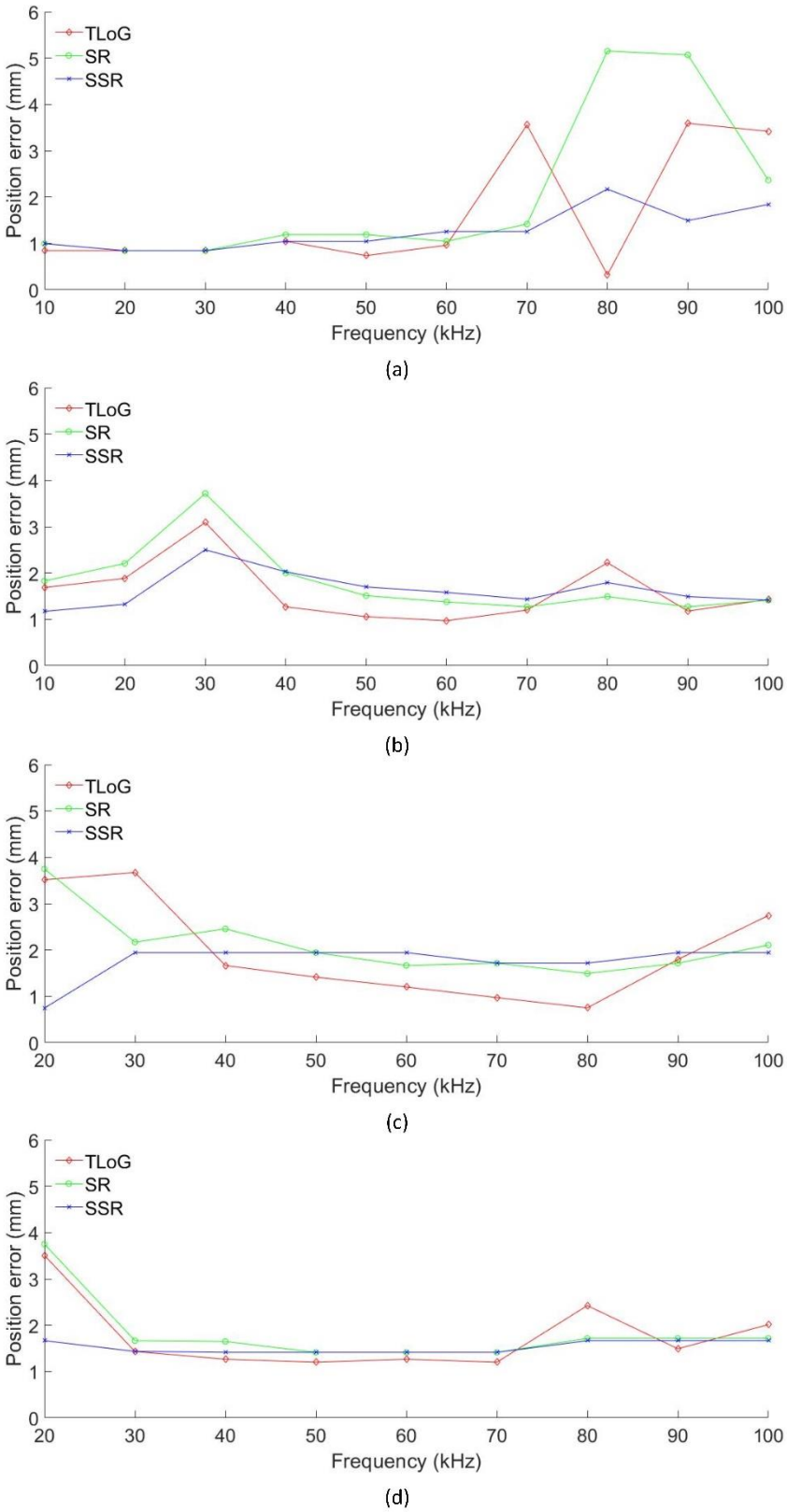

Figure 3-11 Position error of the time-difference images for (a) carrot tissue sample and (b) potato tissue sample, and the frequency-difference images for (c) carrot tissue sample and (d) potato tissue sample

3.3.4 Evaluation of correlation coefficient

The correlation coefficients (CCs) of the reconstructed images are demonstrated in Figure 3-12. For both the time-difference images and frequency-difference images, the frequency that provides a lower PE also allows the image to have a higher CC. SSR provides more stable CCs for images at different frequencies, and the CCs can be maintained above 30% when the conductivity of the potato sample is 0.012 *S/m* lower than that of the saline solution at 30 *kHz*.

With smaller PEs, the CCs of the time-difference images for the carrot tissue sample are higher than the CCs of the time-difference images for the potato tissue samples. However, the CCs of the frequency-difference images for the potato tissue sample are slightly lower than that of the time-difference images for the potato tissue sample, even though they have lower PEs. One of the reasons is the deformation of the sample in the frequency-difference images is larger than that in the time-difference images.

The CCs at most of the frequencies can be only maintained at 60%, which indicates the reconstructed images have distinct differences from the true images. One possible reason is the modelling errors between the sensitivity matrix and the true model. The introduction of tissue samples increased the liquid volume in the sensor, causing modelling errors in the sensitivity matrix. As a consequence, the position of the reconstructed tissue sample deviates from the true position and deformation occurs at the samples. In the future study, the same volume of background solution should be absorbed from the sensor after the introduction of tissue samples, so that the liquid volume can be maintained, and the modelling error is reduced.

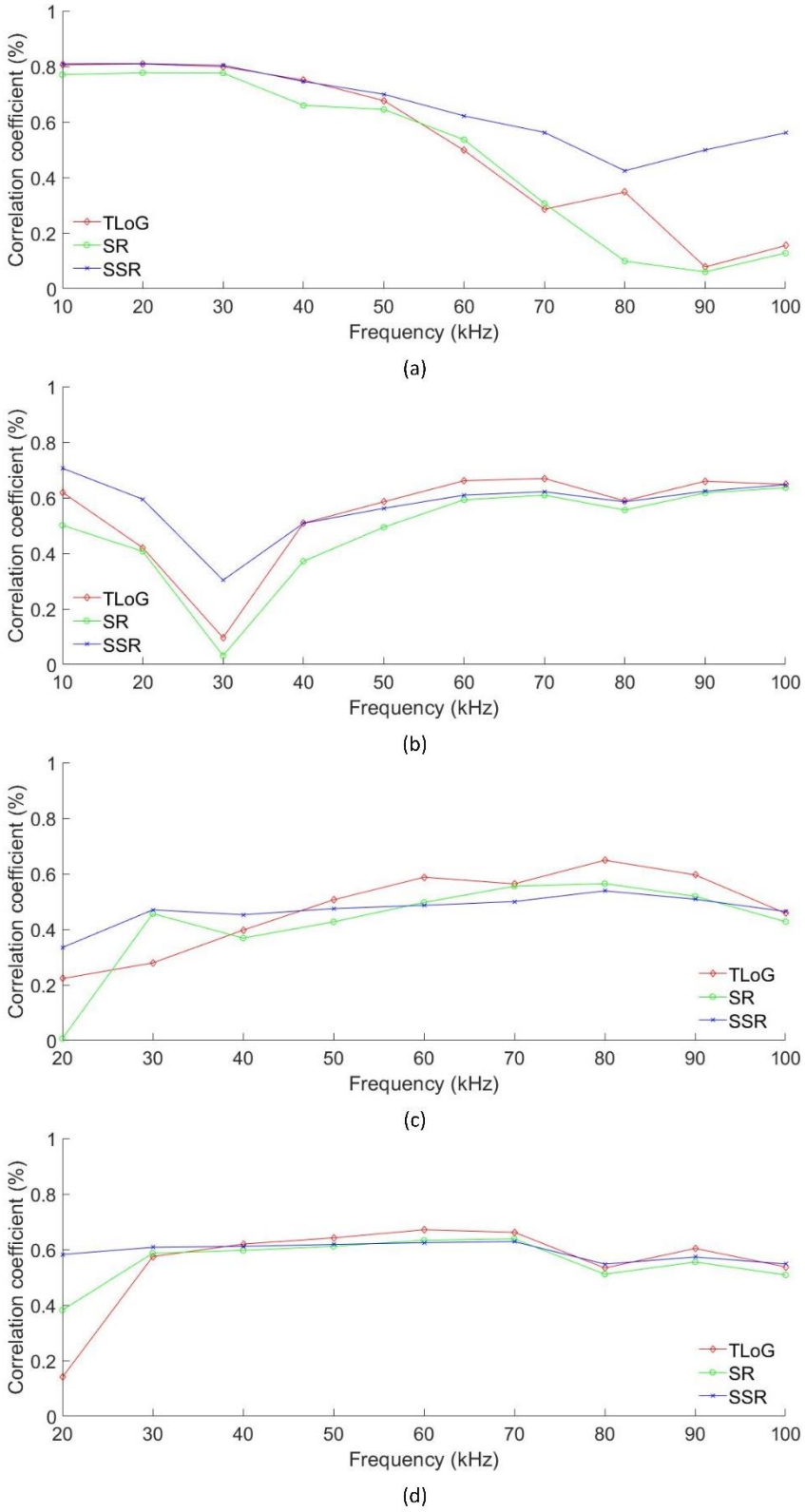

Figure 3-12 Correlation coefficient of the time-difference images for (a) carrot tissue sample and (b) potato tissue sample, and the frequency-difference images for (c) carrot tissue sample and (d) potato tissue sample

3.4 Discussions

The conductivity of tissue depends on the cell composition, geometrical dimension and orientation of the biological cells [124], so different tissues can be distinguished through impedance measurements. The complex conductivity contains the information in both the real and imaginary part. It has more significant changes between different tissues as well as between tissues and the background solution. Hence, it is more suitable to be applied for image reconstruction.

EIT can semi-quantitatively assess the conductivity spectra of the tissue samples cultured in the miniature EIT sensor. The images can measure relative conductivity changes of the tissue samples surrounding by background solution and distinguish different tissue samples by their conductivities at the same frequencies. The conductivity distributions of the samples in the reconstructed images match the conductivity spectra measured by the impedance analyser. To be more precise, the conductivities of the carrot sample and the potato sample in the miniature sensor exceed the conductivity of the saline at 80 kHz and 40 kHz respectively, which is the same as that demonstrated in the conductivity spectra (Figure 3-4). The differences in the multi-frequency conductivity variations between two kinds of tissue samples can be also demonstrated in the reconstructed images.

TDEIT reconstructs the images based on the conductivity variation between the samples and the background solution. The minimum conductivity change should be 0.018 *S/m* in order to improve image quality. Significant PEs and background noises occur when the conductivity of the sample is similar to the conductivity of the background solution. Since the cell membrane can be modelled as a capacitor, the live cells are less conductive at lower frequencies. Considering the high conductivity of culture medium in most of the tissue culture experiments [129], the minimum stimulating frequency of the Agile Tomography system, 10 *kHz*, should be selected as the stimulating frequency for time-difference imaging to maximise the conductivity variation.

FDEIT shows the conductivity variation of the tissue sample between two frequencies, and it is sensitive to the conductivity change of 0.035 *S/m* and above. The impedance spectra in Figure 3-6 show the abrupt conductivity change regions for both tissues located between 10 *kHz* and 200 *kHz*, which is mainly attributed to the polarisation of the cell membranes. To satisfy the sensitivity of FDEIT, the frequency change should be at least 30 *kHz* for highly dense tissue samples. Larger frequency variation is desired for sparsely distributed tissue samples. Therefore, 10 *kHz* and 100 *kHz* are utilised as the stimulating frequencies for FDEIT in this thesis.

Compared with TLoG and SR, SSR has a better performance in critical cases when the SNR is low. The correct sub-domain segmentation helps to reconstruct the position of the sample and to penalise the perturbation in the background, so the image quality has been improved. In other frequencies, the performances of these three algorithms are similar, so the selection of reconstruction algorithms should be based on the measuring data.

With the optimal frequency settings, prominent PEs can be still observed in the reconstructed images, and the CCs of the images maintains at only 60%. This result demonstrates the modelling errors due to the change of liquid volume cannot be neglected. Since the miniature EIT sensor is small, the introduction of tissue samples will significantly change the sensing model. It is important to maintain the liquid volume in the sensing area after each operation.

3.5 Summary

In this chapter, the feasibility of EIT for 3D tissue characterisation in the miniature EIT sensor was proved and its performances with different imaging settings were evaluated. Time-difference imaging and frequency-difference imaging with three reconstruction algorithms were compared in the phantom experiments using carrot samples and potato samples. It was demonstrated that EIT provided the same result as the impedance analyser when operating at proper frequencies. TDEIT, with a stimulation current at 10 *kHz,* could show the conductivity change of the tissue samples when the homogeneous

phantom was used as the reference, so it was suitable to monitor the cellular behaviours which change the tissue conductivity over time. FDEIT between 10 *kHz* and 100 *kHz* showed the polarisation of the cell membranes, which was affected by the radius of the cells and membrane integrity. It would be useful for distinguishing different cell types and monitoring cell viability.

The findings in this chapter help to reduce the errors in the experimental settings for miniature EIT experiments. In Chapter 4 , TDEIT with proposed settings will be applied to monitor the cell mortality in tightly packed tumour spheroids in real-time. The existence of cells in bioscaffolds are evaluated in Chapter 5 and Chapter 6 .

Chapter 4 EIT for real-time and label-free viability assays of 3D tumour spheroids

4.1 Introduction

Three-dimensional (3D) tumour cells in practice are considered to have higher radio- and chemo- resistance than experimental cancer cells cultured in a two-dimensional (2D) environment because of the 3D cell-cell and cell-matrix interactions [136, 137]. It is pointed out as one of the most important reasons for the low success rate in anticancer drug discovery and development [138]. Therefore, there is currently a need to move away from traditional 2D cell culture towards 3D cell culture systems that better mimic the behaviour of in-vivo cells growing in in-vitro experiments [1, 2].

End-point destructive assays, such as histopathology, scanning electron microscopy (SEM) and Transmission electron microscopy (TEM) can be used to evaluate frozen and fixed cell within the 3D structure [5]. But currently, there is no straightforward method to assess cell growth and cell activity in live 3D tissues. Confocal and fluorescence microscopy, the methods of choice for 2D culture, are limited to a penetration depth of less than 50 μm in dense and highly scattering tissues. Consequently, multiphoton microscopy and light-sheet microscopy, in combination with fluorophores, are a better choice to image cells within spheroids [1]. Alternatively, optical coherence tomography can be used to scan large spheroids, and it was recently shown that cell viability could be inferred from the optical signal [139]. However, these techniques required to analyse multiple scans at the same location and therefore have limitations in terms of scanning rate. Phase-contrast imaging, which recorded spheroid drug response by monitoring changes in size and integrity, has been developed to go towards high-throughput imaging [140], but there was no clear indication in regards to change in cell viability.

In order to monitor the drug response in real-time, label-free and a non-destructive manner, a method to apply TDEIT in resolving cell viability for single 3D spheroids was investigated in this chapter. The relationship between

conductivity variation and cell viability was first modelled and evaluated through finite element (FE) simulations. MCF-7 spheroids were then formed with the advanced liquid overlay technique and cultured in the miniature EIT sensor for practical experiments. The lysis buffer Triton X-100, which could cause cell death in a short time, was selected to validate the capability of EIT for drug response monitoring. The concentration of Triton X-100 was chosen through individual factor experiments using ECIS. Finally, the cellular metabolic viability assay was performed on the spheroids to verify the accuracy of the results.

4.2 Methods

4.2.1 Effective medium approximation (EMA) of MCF-7 cell spheroids

The cell is a complex heterogeneous entity and thus can be simplified into a model to calculate its electrical properties [24]. In this study, the MCF-7 cancer cell was fitted into the single-shell model [19] in Figure 4-1. A single cancer cell is composed of the cell membrane and cytoplasm. The cytoplasm can be considered as a homogeneous conductive medium, and the cell membrane separates the cytoplasm from the extracellular culture medium. A tumour spheroid contains several cancer cells, and the culture medium fills the gaps between the cells. The size of the gaps depends on the radius of the tumour spheroid and the number of cells in the spheroid. Based on this model, the relationship between the electrical properties of the spheroids and their physiological characteristics can be accurately controlled. To fit the model into the effective medium approximation theory, the effective complex conductivity σ in Eq. (3-2) is represented by the complex permittivity ε:

$$\sigma = \mathrm{j}\omega\varepsilon_0\varepsilon = \sigma' + \mathrm{j}\omega\varepsilon_0\varepsilon'' \qquad \textbf{4-1}$$

where ε_0 is the permittivity of vacuum and ε'' is the dielectric constant, which contains the same information as the imaginary conductivity demonstrated at Section 3.2.1:

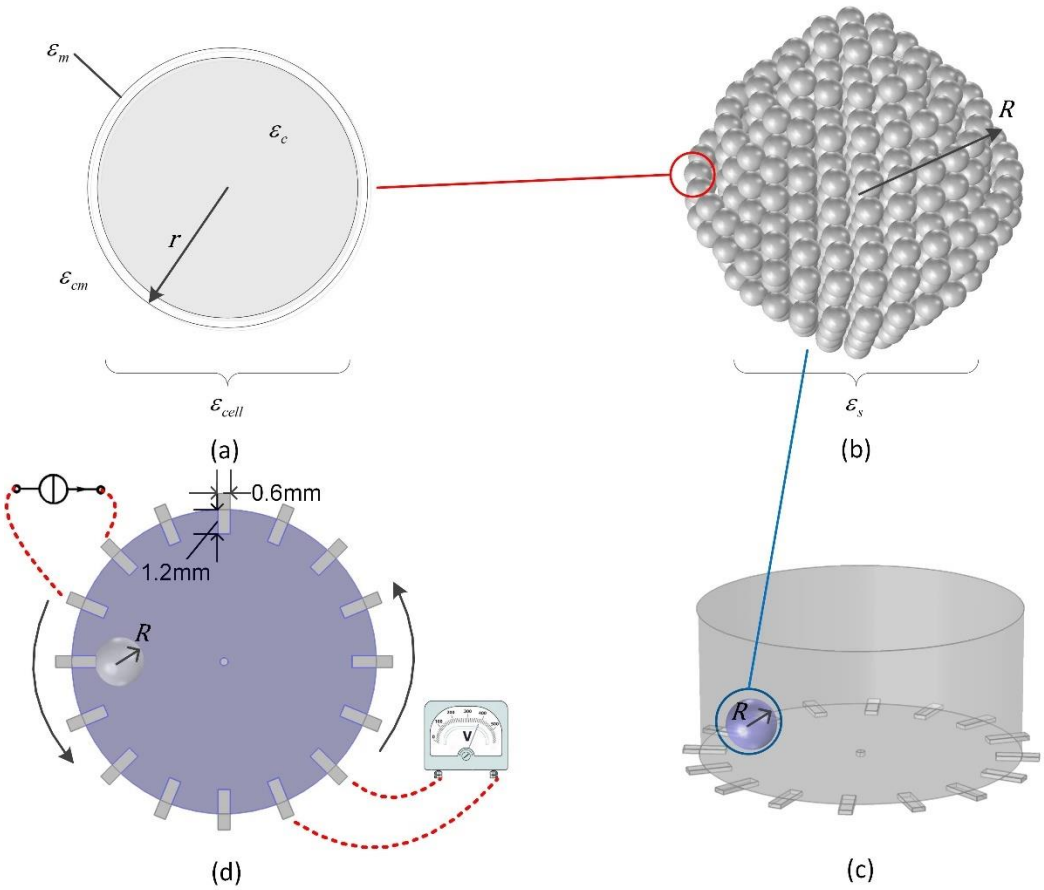

Figure 4-1 Simulation models for (a) a single cell, (b) a tumour spheroid and the EIT sensor in (c) stereo view and (d) top view

$$\sigma'' = \mathrm{j}\omega\varepsilon_0\varepsilon'' \qquad \textbf{4-2}$$

Then, the equivalent homogeneous complex permittivity of the whole cell ε_{cell} can be determined by the Maxwell Garnett equation in Eq. (4-3):

$$\varepsilon_{cell} = \varepsilon_m \frac{2(1-v)\varepsilon_m + (1+2v)\varepsilon_c}{(2+v)\varepsilon_c + (1-v)\varepsilon_m} \qquad \textbf{4-3}$$

where ε_c is the complex permittivity of the cytoplasm, ε_m is the complex permittivity of the cell membrane and $v=\left(1-d_m/r\right)^3$, in which r is the outer radius of the cell and d_m is the thickness of the membrane.

In the multicellular spheroid model, each MCF-7 cell is considered as a sphere. The cells are surrounded by the external culture medium and evenly distributed within the spheroid with the radius of R (Figure 4-1 (b)). The volume fraction P of the cells over the spheroid depends on the number of cells x in the spheroid, which is given by $P=x\left(r/R\right)^3$. To estimate the permittivity of the whole spheroid, Hanai's equation [46] is preferable in the EMA, since it takes the high volume fraction into account and it is suitable for cells in different morphology:

$$\frac{\varepsilon_s-\varepsilon_{cell}}{\varepsilon_{cm}-\varepsilon_{cell}}\left(\frac{\varepsilon_{cm}}{\varepsilon_s}\right)^n=1-P \qquad \textbf{4-4}$$

where ε_{cm} and ε_s are the complex permittivities of the culture medium and the whole spheroid, respectively. The morphology parameter n is set to 1/3 for the spherical MCF-7 cancer cells. Eq. (4-1) to Eq. (4-4) are used to determine the FE simulation parameters in the next section, in particular the effective permittivity of cell spheroid.

4.2.2 Evaluation of EIT for spheroid imaging

The FE simulations to evaluate the performance of EIT in spheroid monitoring were performed in the COMSOL Multiphysics with an AC/DC module in the frequency domain study. A cylindrical EIT sensor model was built with 15 *mm* in diameter and 7 *mm* in height to simulate the sensor filled with 1.2ml culture medium. 16 rectangular electrodes (dimensions: $1.2\times0.6\,mm^2$) were evenly distributed at the boundary of the substrate of the chamber and the circular ground electrode was designed in the centre of the well with a diameter of $0.4\,mm$. A tumour spheroid with the radius of R was placed on the substrate of the sensor (Figure 4-1 (c)). The conductivity and the permittivity of the

culture medium, the cell membrane and the cytoplasm of the viable cell were set as $\sigma'_{cm} = 1.5\,S/m$, $\varepsilon''_{cm} = 80$, $\sigma'_{m} = 0\,S/m$, $\varepsilon''_{cm} = 5$, $\sigma'_{c} = 1.5\,S/m$, $\varepsilon''_{c} = 80$ [9, 129], respectively. The size of the cells and the volume fraction were defined to $r = 10\,\mu m$, $d_m = 5nm$ and $P = 46\%$ based on the characteristics of the MCF-7 breast cancer cells [141] and the tightly packed tumour spheroids [142]. In order to reduce the computational cost, the cell spheroid in Figure 4-1 (b) was considered as a sphere, and its effective permittivity ε_s^* was calculated based on Eq. (4-3) and Eq. (4-4).

In the simulation, the adjacent drive method [15, 17] was adopted for the current stimulation and voltage measurements, which increased the sensitivity to the cellular response near the electrode. A $10kHz$ current with an amplitude of $1mA$ was applied to a pair of the electrode, and the electrical properties of the spheroid were measured from successive adjacent electrode pair (Figure 4-1 (d)). By switching the current stimulation positions, totally 104 independent measurements in total were obtained as a data set for the image reconstruction.

4.2.3 Impedance measurement system

The impedance measurements were carried out in a cylindrical miniature EIT sensor with microelectrode arrays [143] at the substrate (Figure 4-2 (a-b)). The diameter and the height of the chamber were $15\,mm$ while the number and sizes of the gold-plated electrodes were the same as the setting in the FE simulations. The adjacent current stimulations and voltage measurements were performed with the high-speed EIT system (Figure 4-2 (c)) introduced at Section 2.5.2. In this study, the frequency of the stimulation current was set to $10\,kHz$ and the frame rate was 30 frame per second (fps). To test the performance of the miniature sensor, 1.2ml culture medium was added to the sensor, and the boundary voltages on the electrodes were continuously measured through the system for 1 hour. The SNR of each channel can be calculated by (4-5):

$$SNR = 10\log\frac{\sum_{i=1}^{t}(v(i))^2}{\sum_{i=1}^{t}(v(i)-\bar{v})^2} \quad \text{4-5}$$

where $v(i)$ and $\bar{v}$ are the voltage measured at the time i and the mean voltage of this channel, respectively.

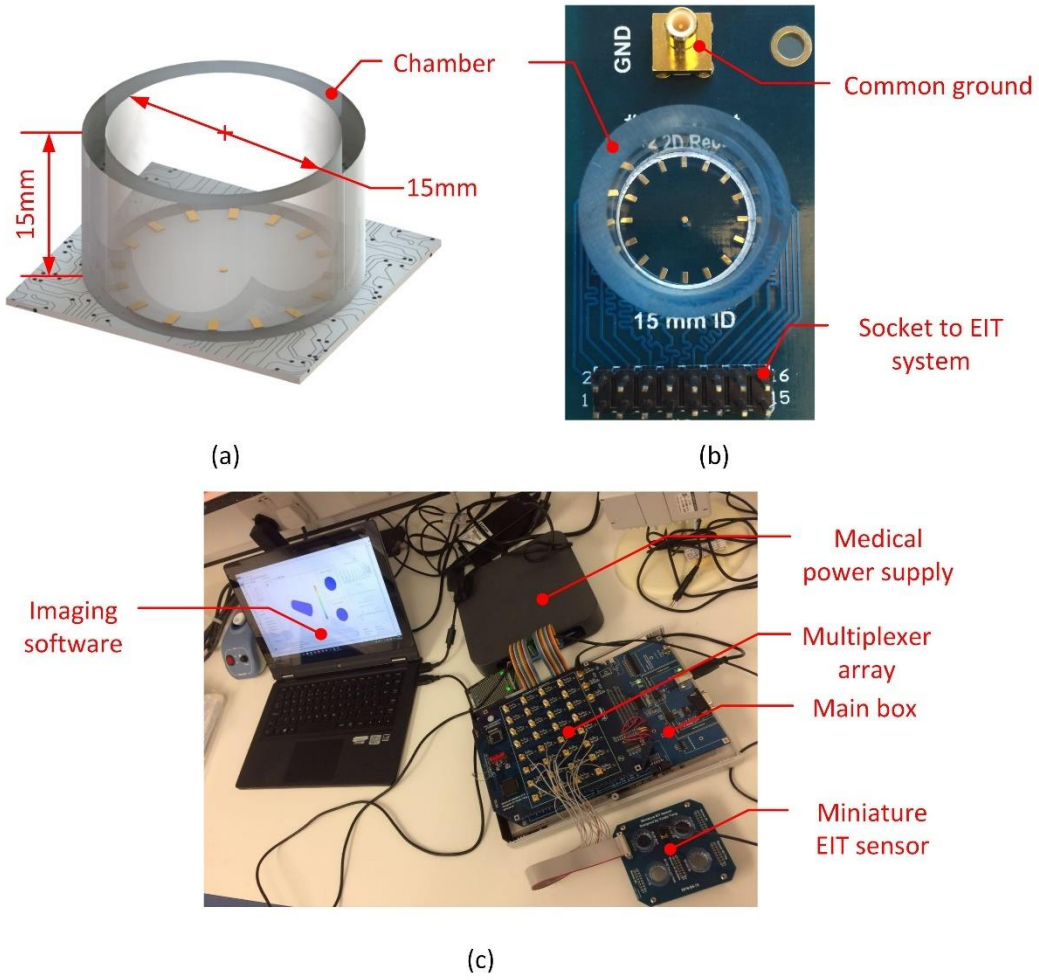

Figure 4-2 Picture of (a) the sensor structure diagram, (b) the manufactured miniature EIT sensor, and (c) the high-speed EIT system

4.2.4 Cell line maintenance

The MCF-7 breast cancer cells were obtained from ATCC (Middlesex, UK) and were routinely grown in T-25 flasks in a humidified 5% CO_2 incubator at 37 ℃. The culture medium was low glucose Dulbecco's Modified Eagle Medium

(DMEM) with glutamax (Thermo Fisher Scientific, Waltham, MA USA) supplemented with 10% (v/v) fetal bovine serum (FBS) and 1% (v/v) penicillin/streptomycin. After cells attained confluence, they were subcultured using 0.25% Trypsin.

4.2.5 Tumour spheroids formation

As can be seen in

Figure 4-3, the liquid overlay technique [144] was adopted and optimised to form cell spheroids. In order to avoid cell attachment, the 24-well plate was first coated with agarose film. 1% (w/v) agarose dissolved in deionized water was sterilised by heating to 120 ℃ under 100 *kPa* for 15 minutes. It was immediately pipetted to the 24-well plate with the volume of 400μl per well and was then placed in room temperature for 20 minutes to form the film. To maintain the temperature of the agarose solution, all the tips were warmed up in 100 ℃ hot water bath before use. Culture medium was removed from the T-25 flasks, and the cells were trypsinised by 0.25% Trypsin for 5 minutes. 1 *ml* fresh culture medium was then added to the flasks and the concentration of the trypsinised cell suspension was counted on the haemocytometer. Extra culture medium was added to the flasks to dilute the trypsinised cell suspension to 10^4 *cells/ml*. To accelerate the cohesion of the spheroid, the culture medium for spheroid culture was optimised to high glucose DMEM based culture medium (HG culture medium). Finally, 1 *ml* of diluted cell suspension was pipetted into the 24-well plate for spheroid formation. The 24-well plate was maintained under horizontal stirring with the Orbi-Shaker BT4000-E (Benchmark Scientific, New Jersey, USA) at 120 *rpm*. The culture period should be last for at least 5 days to increase the toughness of the spheroids. 500 μl HG culture medium was exchanged daily since the fifth day. The size of the spheroids was controlled by the culture period. In this study, the MCF-7 cells were cultured in the incubator for 6 days, and the average radius of the spheroids was around 1.2 *mm* (Figure 4-4).

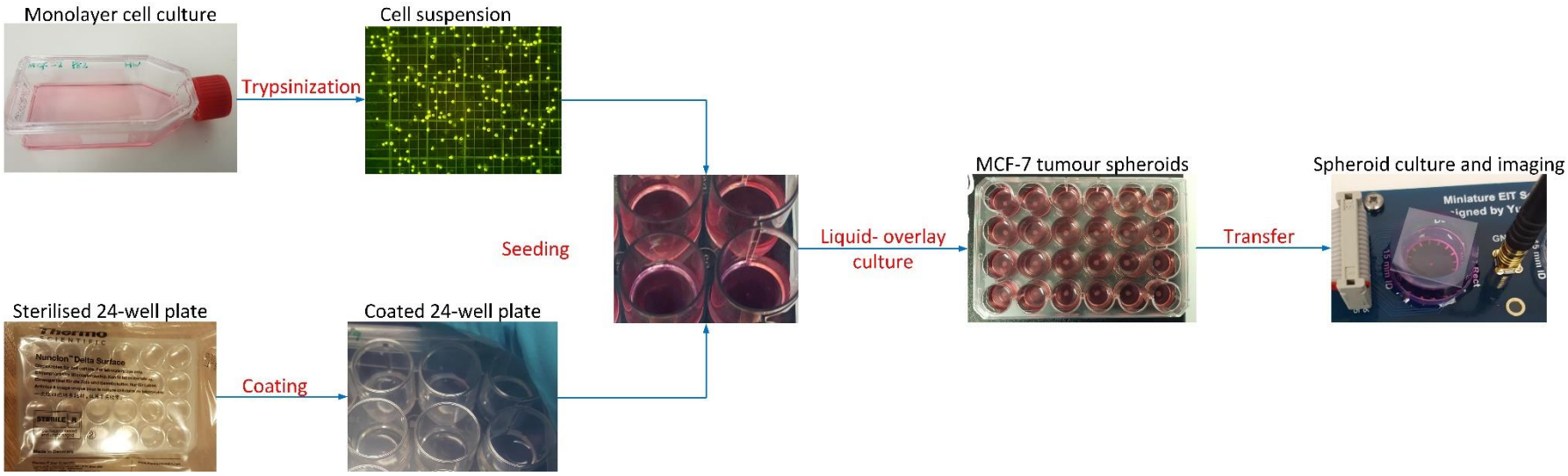

Figure 4-3 Protocol for MCF-7 tumour spheroid formation and imaging in the miniature EIT sensor

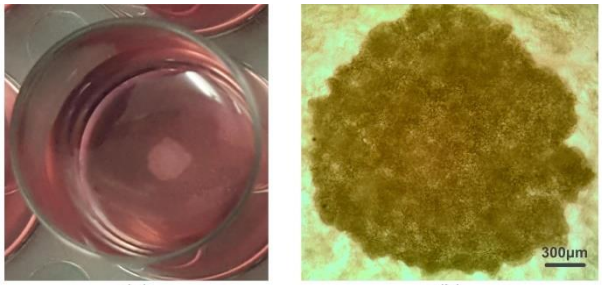

Figure 4-4 MCF-7 spheroid sample cultured in 24-well plate, (a) Digital camera image and (b) optical contrast microscopy image, the scale bar correspond to 300 *μm*.

4.2.6 Chemical insult and the reagent

Triton X-100 is a non-ionic, non-denaturing detergent wildly used in biochemical applications for lysing cells. Triton X-100 can change the live-cell permeability and morphology at low concentration, while a high concentration of the detergent will solubilise the cell membrane proteins, which eventually result in cell death by necrosis [145, 146]. In this study, the Triton X-100 solution is used to study cell viability in a time-lapse fashion. 2% (*v/v*) Triton X-100 solution is prepared by pre-mixing 0.2ml Triton X-100 electrophoresis reagent liquid (Alfa Aesar, Lancashire, UK) with 9.8ml HG culture medium. The conductivity of the Triton X-100 solution and the HG culture medium at room temperature is 2 *S/m* and 2.07 *S/m*, respectively.

4.2.7 Cellular metabolic viability assay

To assess the cellular metabolic viability of the MCF-7 spheroids, Presto-blue Cell Viability Reagent (Thermo Fisher Scientific, Waltham, MA USA) was used in the endpoint study. PrestoBlue assay is a kind of colourimetric assays to evaluate the viability and proliferation of cellular samples. Based on the Beer-Lambert law, the absorbance is proportional to the concentrations of the absorbing materials in the sample when the length of the beam in the sample is fixed [147]. Since the concentration of the PrestoBlue reagent is quickly reduced by metabolically active cells, it can provide a quantitative measure of viability and cytotoxicity of the samples [148, 149].

The spheroid samples treated by 2% Triton X-100 solution for 30 minutes and their blank control without any treatment were transferred to a 96-well plate.

The PrestoBlue reagent was mixed with the HG culture medium in a 1:9 mixing ratio following the product information sheet. 100 μl mixed solution was added to each well and the 96-well plate was then placed into the incubator at 37 ℃ for 60 minutes. 40 μl solution was then sampled from each well and tested in the Modulus™ II Microplate Multimode Reader using 525 nm (EX) / 580-640 nm (EM) fluorescence. The testing results were shown in the relative light unit (RLU), which indicated the amount of light detected by the detector. To remove the background disturbance, the RLU of the HG culture medium was used as the reference. A higher RLU means higher cellular viability of the MCF-7 spheroid under test.

4.3 Results

4.3.1 Finite-element simulations for sensitivity evaluation

Prior to monitor the spheroid viability in real-time, it is important to examine the theoretical detection limit of EIT for the cell spheroids. Hence, two simulations were performed to examine the spatial sensitivity and viability detection limit of EIT, which could be used as a reference for the parameter setting in the real-time cellular assay. In this section and Section 4.3.2, L1-norm regularisation (Eq. (2-33)) was applied in the image reconstruction.

4.3.1.1Spatial sensitivity

The spatial sensitivity of the EIT measurement evaluates the performance of EIT in reconstructing the size and position of the spheroids. The sensor was first filled with culture medium as a reference, and then the spheroids in different sizes were introduced to the substrate of the sensor as shown in Figure 4-1 (c) and (d). Voltage measurements were taken from the electrodes for EIT image reconstruction. Based on the calculation of Eq. (4-5), the average SNR of the system was 52.63dB. Hence, Gaussian noise was added to the boundary voltages to achieve the signal to noise ratio (SNR) of 50dB to simulate the conditions of practical experiments. The spatial sensitivity of the reconstructed image was evaluated by the correlation coefficient (CC) demonstrated in equation (3-18). A higher CC means the similarity between

the actual size and position of the spheroid is closer to the reconstructed value, which means the reconstructed image is a better representation of the spheroid under study. The smallest spheroid that can generate the highest CC values was defined as the spatial sensitivity of the measurement because its signal is strong enough to tolerate the disturbance of the measurement noise.

Figure 4-5 shows the reconstructed images in the presence of MCF-7 cell spheroids with increasing radius. Based on the electrical characteristics of viable cells mentioned in section 4.2.2, the effective conductivity of the viable cell spheroid σ_s is equal to $0.595\ S/m$, which is lower than the conductivity of the culture medium σ_{cm}. Hence, the introduction of the spheroid results in the conductivity drop in the corresponding area. In the presence of spheroids with a small radius (Figure 4-5 (a) and (b)), the resulting disturbance to the boundary voltage is weak, and the signal level is similar to the noise level. In Figure 4-5 (c) and (d), larger spheroids generate stronger signals to the boundary voltages, and better image quality is generated. The correlation coefficient histogram (Figure 4-5 (e)) indicates that the minimum radius of the spheroid maintaining high image quality is 0.8 *mm*. It means that the spatial sensitivity of the measurement is 1.14% of the sensor surface area.

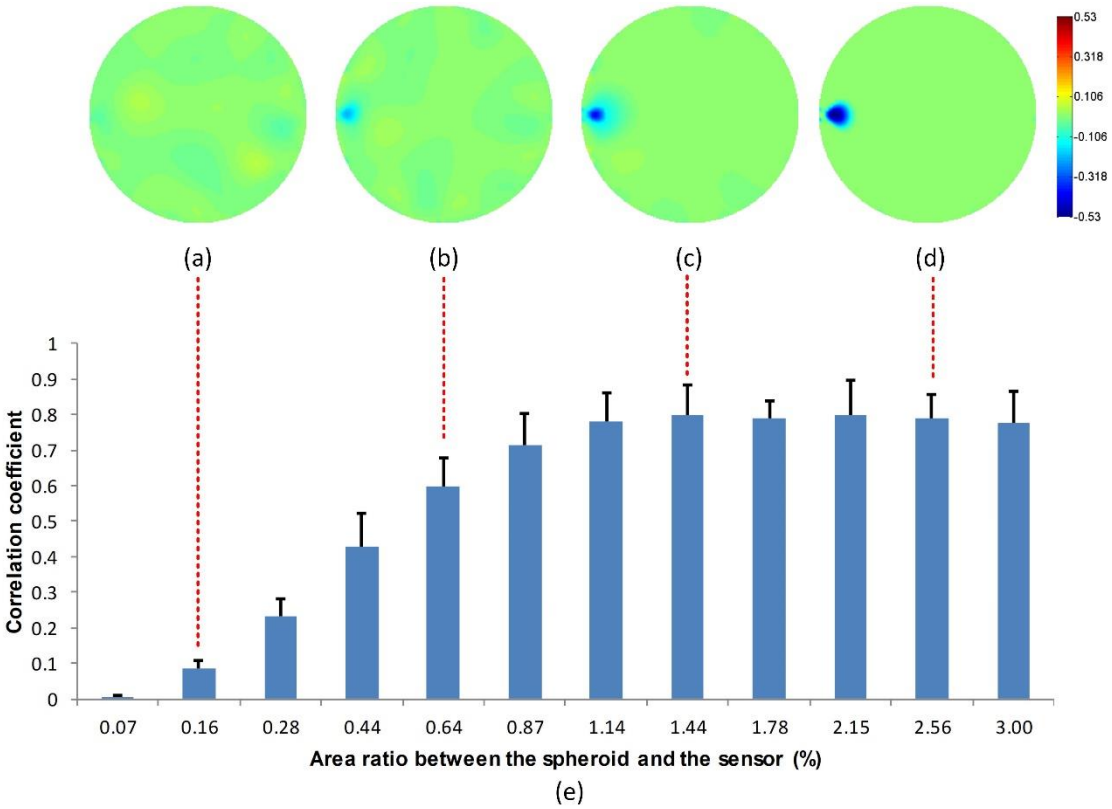

Figure 4-5 Reconstructed images for the spheroids in size of (a) 0.16%, (b) 0.64%, (c) 1.44% and (d) 2.56% of the sensor and (e) their correlation coefficient with the true image based on 20 measurement samples for each size of the spheroid (n=20).

4.3.1.2Detection limits of spheroid viability

The purpose of this simulation is to evaluate the sensitivity of EIT measurement to the conductivity change of the spheroid caused by cell death. A viable cell spheroid with a radius R of 1.2 *mm* (area ratio of 2.56%) was simulated inside the sensor filled with culture medium and a cytotoxic agent as shown in Figure 4-1 (c) and (d). Since the volume of the biochemical agent was far smaller than that of the culture medium, it was assumed that the conductivity of the background solution was equal to the conductivity of the culture medium σ_{cm}. Then, the effect of the cytotoxic agent with a gradual viability loss of the spheroid down to 0% (cell mortality rate increased from 0 to 100%) was simulated by modifying their dielectric properties parameters in the simulation. Since the membrane of dead cells lost the resistance to the low-frequency electric current, its conductivity and permittivity were increased

to $\sigma'_m = 1.5 S/m$ and $\varepsilon''_m = 80$. The conductivity of the spheroid with partial dead cells was updated with Eq. (4-4), and it increased with the cell mortality rate. EIT was used to reconstruct the conductivity change of the spheroid to deduce the cell mortality under 50 dB noise level. A threshold-based conductivity mask was applied to the reconstructed images to locate the spheroid and to calculate the average conductivity change of the spheroid associated with cell death.

According to Figure 4-6, the conductivity variation due to cell mortality can be detected and reconstructed in the correct position when the mortality rate is over 30%. The variation increases with cell mortality as expected. Figure 4-6 (k) shows the relationship between the reconstructed conductivity variation and the cell mortality rate was plotted with 30 spheroid samples. The y-axis on the left is corresponding to the normalised conductivity variation in the reconstructed images and the y-axis on the right is corresponding to the true spheroid conductivity change in the simulation. A good correlation exists between the reconstructed conductivity variation and the cell mortality rate at 20% and above, but the results at 20% mortality rate are not convincing because the conductivity variation in the RoI is almost the same as that at the background area in Figure 4-6 (b). Hence, EIT reconstructed conductivity variation can be used as an indicator of the cell mortality in the spheroids when the mortality rate is over 30%.

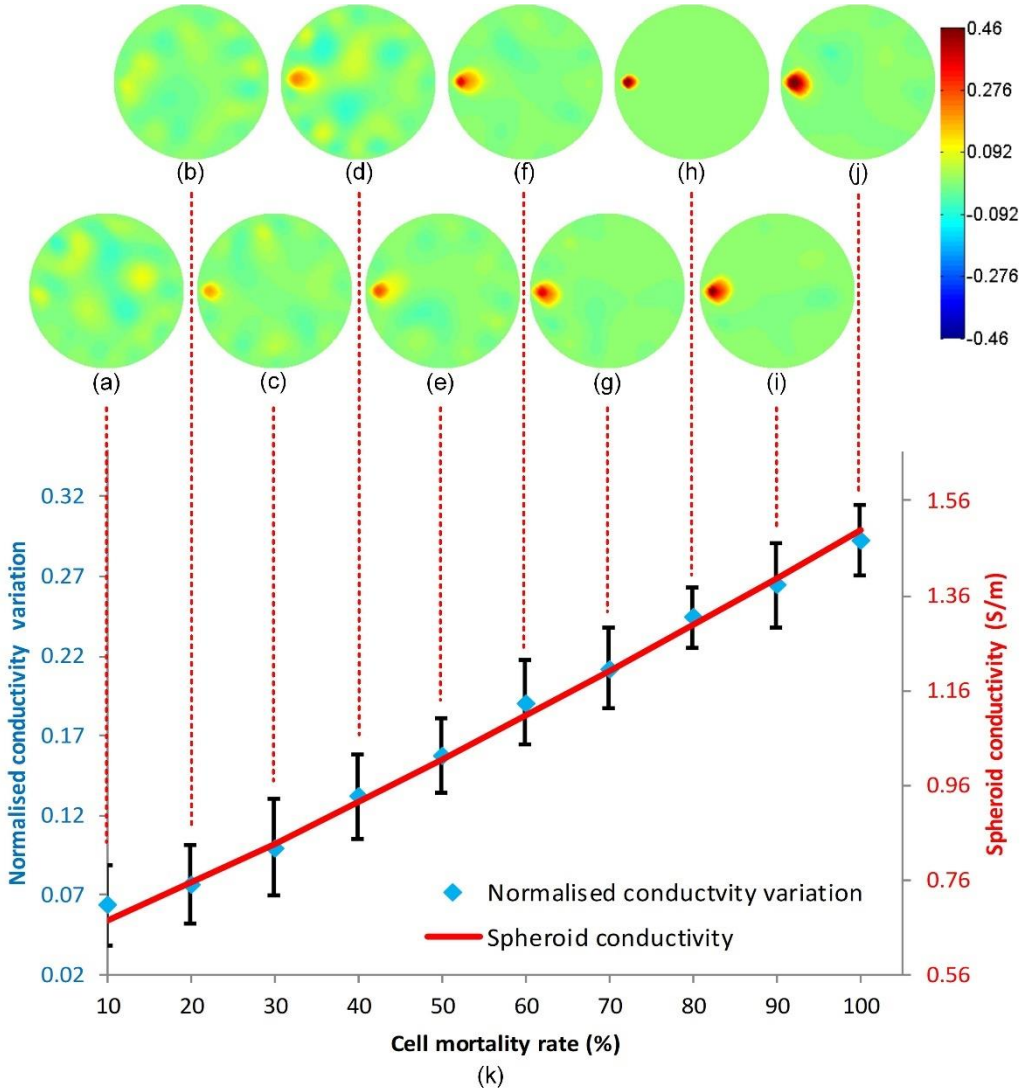

Figure 4-6 Sample images for spheroid at (a) 10%, (b) 20%, (c) 30%, (d) 40%, (e) 50% , (f) 60%, (g) 70%, (h) 80%%, (i) 90% and (j) 100% mortality rate, and (k) the comparison diagram between the reconstructed conductivity variation and the cell mortality rate (n=30).

4.3.2 Real-time imaging of spheroid viability

In this section, experiments with MCF-7 spheroids were carried out to validate the FE simulations and the feasibility of EIT for real-time imaging. In order to monitor the dynamic course of cell death, the spheroids introduced in Section 4.2.5 were introduced into the miniature sensor with 1.2ml 2% Triton X-100 solution (experimental group). In the control group, the spheroids were introduced into the miniature sensor with 1.2ml HG culture medium. Reference

for EIT imaging was taken immediately after that. Both the experimental group and the control group have two samples.

Figure 4-7 (a) shows the reconstructed images for the response of the MCF-7 spheroids in the 2% Triton X-100 solution (experimental group) and the HG culture medium (control group). These images show the difference of conductivity between the reference and the conductivity at the selected time points. 300 images in total were reconstructed for each sample, and the processing time for each image was less than 0.3 second. As expected, the conductivity of the spheroids in the Triton X-100 solution has a significant increase while the conductivity of the spheroids in HG culture medium remains unchanged. In the experimental group, the conductivity of the spheroids started to increase at about 2 minutes until it reaches a plateau between 0.04 and 0.05 at 22 minutes. The increase was caused by the destruction of the insulating cell membranes after cell death. This result was consistent with the previous MCF-7 chemical response data in 2D [150-152], but the longer response time was observed, likely due to the 3D structure of the spheroids. The standard deviation around the mean could be explained by the individual differences between two spheroids in morphological characteristics, cell concentration and initial cell viabilities. In Figure 4-7 (b), the chemical insult over time is reconstructed in real-time with small fluctuation. One reason for the fluctuation is the reconstruction parameter λ of Eq. (2-33) in this experiment is fixed in order to compare the conductivity changes in different groups, so it is not optimised for each group to obtain the best image quality. The comparison of the relative light unit (RLU) in the control group and the experimental group shows that the viability of the MCF-7 spheroids almost drops to zero after a 30-minute treatment in the 2% Triton X-100 solution (Figure 4-8). These data show that EIT can monitor and analyse the cell viability on 3D cell spheroids in real-time.

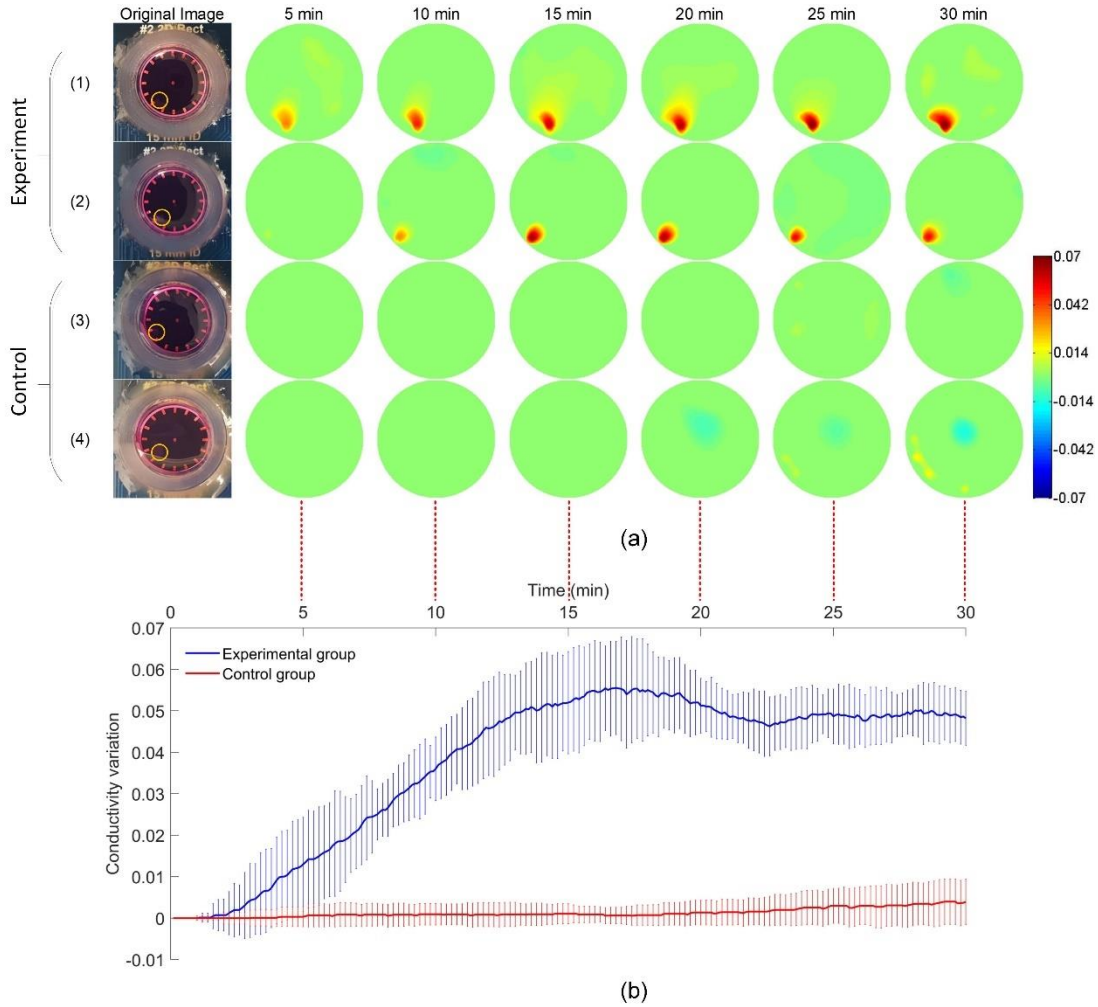

Figure 4-7 Reconstructed images for the spheroid samples in (a1-2) 2% Triton X-100 solution (experimental group) and (a3-4) HG culture medium (control group) and (b) the conductivity variation of the spheroids (n=2).

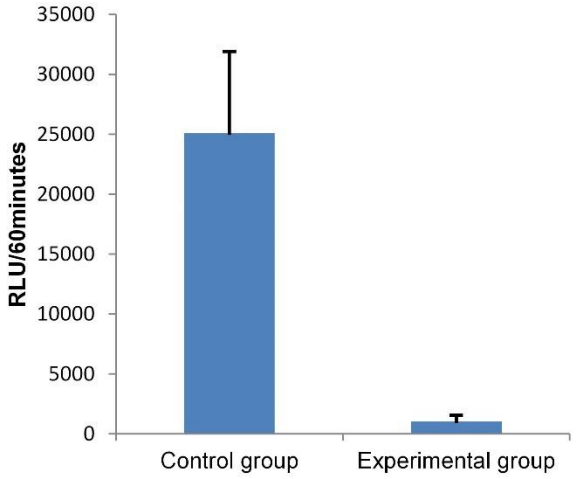

Figure 4-8 The cellular metabolic viability assay for the spheroids (n=5)

4.4 Discussions

In this study, 2D EIT image reconstruction model was applied to reconstruct the conductivity distribution images. This setting projected the change in the sensor into 2D space. This method was chosen because it significantly reduced the computational time required to reconstruct an image when compared to 3D EIT reconstruction [153], and was therefore more suitable for a new technology to monitor in real-time and label-free cellular viability. Since the conductivity of the background medium was almost invariable during the measurement, the conductivity variation in the sensor was mainly attributed to the change of the cells. Therefore, the 2D conductivity distribution in the images could directly reflect the conductivity variation of the 3D cell spheroids.

The selection of the spheroid position in this study was to optimise the signal intensity of the EIT measurements and to improve the image reconstruction with the adjacent drive method. To measure samples located at the centre of the sensor, the polar-offset current drive [126] or opposite current drive [15] should be applied to maintain high sensitivity in the central area. In future studies, optimization could be performed to automatically detect the position of the samples and choose the best current stimulation pattern to increase the sensitivity of the measurements.

Taken together, the results show that the viability and integrity of the 3D cell spheroids can be monitored in real-time and in their cell culture environments with EIT. This method is sensitive to the physiological variation of the cell spheroids. It allows the continuous monitoring of the spheroid integrity and size, which is a parameter of interest alongside the cell viability[140]. Cell mortality caused by a chemical insult can be reconstructed in real-time through its correlated conductivity variations in the spheroid. Monitoring the response of MCF-7 spheroids to the Triton X-100 solution demonstrated the ability of EIT to perform the real-time and label-free cellular assay. Although its spatial resolution is not as high as other imaging techniques, such as confocal and fluorescence microscopy, EIT has several distinct advantages over the existing techniques including cost, non-destruction, portability, high temporal resolution and potential for multiplexing and long-term high throughput screening. Overall, EIT maintains the advantages of other impedimetric measurement techniques while overcoming the lack of spatial resolution.

4.5 Summary

In this chapter, the protocol and associated methodologies of EIT to monitor in real-time and non-destructively cell viability in 3D cell spheroids have been developed. This technique was demonstrated in a single-well format, but it could be easily multiplexed to multi-well plate format. The relationship between cell viability and spheroid conductivity was investigated for the first time through EMA theory. It was then used to evaluate the feasibility of EIT for spheroid imaging in FE modelling simulation. Experiments were performed to evaluate the potential and suitability of EIT to monitor in real-time and label-free transient changes in cell viability induced by a chemical insult within large 3D spheroids. To the best of my knowledge, this is the first study to perform FE simulations with tightly packed tumour spheroids and to demonstrate real-time and label-free monitoring of conductivity variation of 3D cell spheroids following a chemical insult. It takes a step forward towards the miniaturisation of impedance imaging to enable on-line monitoring of the cellular activities in

a 3D environment, and the integration of the EIT technique to drug-screening platforms.

Chapter 5 Exploring the Potential of EIT for Tissue Engineering Applications

5.1 Introduction

Beside drug discovery, tissue engineering is another important topic in biological research. Its purpose is to generate artificial tissues and organs to repair or replace damaged tissues in the human body [154]. It generally uses a combination of cells and biomaterials to manufacture samples several orders of magnitude higher than a single cell volume. Currently, tissue engineering makes use of a variety of biomaterials varying from polymers and hydrogels to decellularized animal tissues [155]. The morphologies of these biomaterials are similar to that of the extracellular matrix, so they can provide the appropriate environment for the regeneration of tissues and organs in 3D.

Monitoring the cell characteristics in the scaffolds and hydrogels provides information for the biologists to better control the cell culture and differentiation processes. However, it is difficult to assess the cell viability and proliferation in large samples with height and diameter at the millimetre scale and composed of non-transparent biomaterials. EIT has successfully been applied to monitor the adhered cell migration [156] and the drug response of cell aggregates that have a relatively high concentration in the local area [157], but its feasibility on sparse cell monitoring has yet to be investigated.

In this chapter, the potential of EIT for tissue engineering applications, where the cells were sparsely distributed within the hosting scaffolds, has been explored. MCF-7 breast cancer cells were first seeded into the microporous scaffolds and the hydrogels. They were then cultured in the miniature EIT sensor. Time-difference imaging and frequency-difference imaging were performed to monitor the cell distribution within the samples. Experiments were also carried out to monitor the conductivity variation of the microporous scaffold when Triton X-100 was added to the sensor. The results were compared with the reconstructed images for the carrot and potato tissues in Chapter 3 and the cell mortality images in Chapter 4 .

5.2 Methods

5.2.1 Cell Line Maintenance

Breast cancer cells, MCF-7, were routinely cultured in a Dulbecco's Modified Eagle's Medium (Life Technologies, Carlsbad, CA, USA) containing 10% fetal bovine serum (Thermo Fisher Scientific, Waltham, MA, USA) and 1% penicillin-streptomycin (Life Technologies, Carlsbad, CA, USA). MCF-7 breast cancer cells were grown in an incubator at 37 °C with 5% CO_2, and the medium was changed every 48 h.

5.2.2 Cell Seeding in Hydrogels and Microporous Scaffolds

96-well AlgiMatrix scaffolds (Life Technologies, CA, USA) and HyStem-HP hydrogel (Sigma-Aldrich, St. Louis, MO, USA) were used to evaluate the feasibility of EIT for sparsely distributed tissue culture imaging. The MCF-7 breast cancer cells were seeded into the hydrogels and scaffolds with a concentration of 5×10^6 cells in each scaffold. This concentration allowed the cells to completely fill the void spaces of the scaffolds [158]. The equivalent volume fraction of the cells in the scaffold was 10.7%, which was lower than that of densely packed cell spheroids with a volume fraction between 46% and 65%, so I considered it as the sparse cell distribution.

The cells were first recovered with 0.25% trypsin (Mediatech, Manassas, VA, USA) so that they can detach from the flasks. 1 *ml* of fresh culture medium was then added to the flasks and the concentration of the trypsinised cell suspension was counted on the haemocytometer. The cell suspension was then transferred to a centrifugation tube and was centrifuged at 259 relative centrifugal forces (RCF) for five minutes to obtain the MCF-7 cell pellets.

To prepare HyStem-HP hydrogel, HyStem-HP, Gelin-S and Extralink 2 powder were dissolved in degassed water and mixed following the standard operation protocol. The cell pellet was then suspended into the mixed solution to achieve the seeding concentration of 5×10^7 *cells/ml*. The hydrogel samples were formed by adding 100 *µl* mixed solution with cells to the 96-well culture dish. Blank controls without cells were also prepared by adding 100 *µl* mixed

solution to the 96-well culture dish. Both the hydrogel samples and the blank controls were then placed at room temperature for ten minutes to facilitate the gelation.

To prepare the AlgiMatrix scaffolds, the supernate in the centrifugation tube was removed, and the fresh culture medium was added to the tube to resolve the cell pellet to the cell suspension with a concentration of 5×10^7 *cells/ml*. The AlgiMatrix sponges were rehydrated with 50% firming buffer for five min in the 96-well culture dish. Rehydrated scaffolds were then transferred to new culture dishes, and 100 *µl* cell suspension was added to each dish for cell seeding. The new culture dishes were placed into the incubator for two hours to allow cell attachment. In the control groups, the rehydrated scaffolds were immersed in the fresh culture medium before being placed into the incubator.

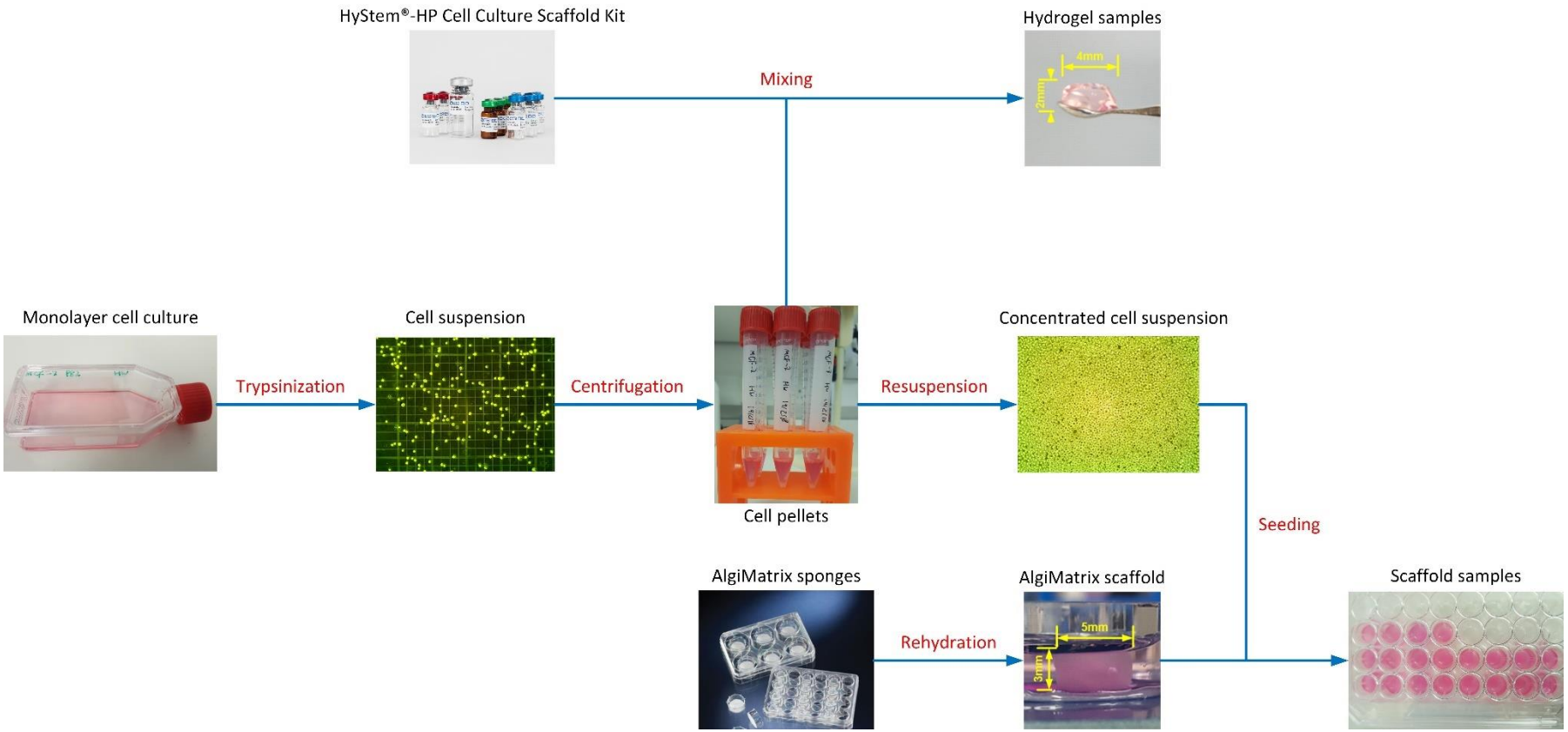

Figure 5-1 Protocol for the formation of hydrogel samples and scaffold samples with MCF-7 breast cancer cells

5.2.3 EIT Measurements in the Miniature Sensor

Experiments were taken at 24 hours after cell seeding. The cell-loaded hydrogel samples, scaffold samples and their blank controls were transferred to the miniature EIT sensor for EIT measurements. The chamber of the sensor was a cylinder with a diameter of 15 *mm*. 1.2 *ml* culture medium was added to the sensor, and the liquid surface was increased to 7 *mm*. The EIT measurements were carried out with the multi-frequency EIT system demonstrated in Section 2.5.2. The adjacent current method was applied, and the measurements were taken from the electrodes evenly distributed at the edge of the sensor.

The settings of EIT was based on the findings in Chapter 3 . Samples and the blank controls were sequentially placed at two positions for the measurement. The first position was between electrodes 6 to 8 and the second position was between electrodes 11 to 13, which can be established in the electrode configuration model at Figure 5-2. In TDEIT, references were taken at 10 *kHz* when the sensor was filled with the culture medium. After adding the sample or the blank control into the sensor, the same volume of culture medium was absorbed using pipette before the measurement. In FDEIT, the sample or the blank control was added to the sensor, and the measurement was taken between 10 *kHz* and 100 *kHz*. This selection can also be explained by the three dispersion mechanisms introduced [22, 134], which illustrated the frequency response of biological tissues and cell suspensions. The α-dispersion appeared below several *kHz* and was not easy to measure due to the interference from the electrode polarisation effects. The β-dispersion distributed between 10 *kHz* to several *MHz* was mainly attributed to the interfacial polarisation due to the existence of the insulating membrane surrounding the cells. By imaging the conductivity distribution at the β-dispersion, the concentration of viable cells in the samples can be estimated [22]. In order to avoid the heating effect, the amplitude of the current was set to 1 *mA* [159].

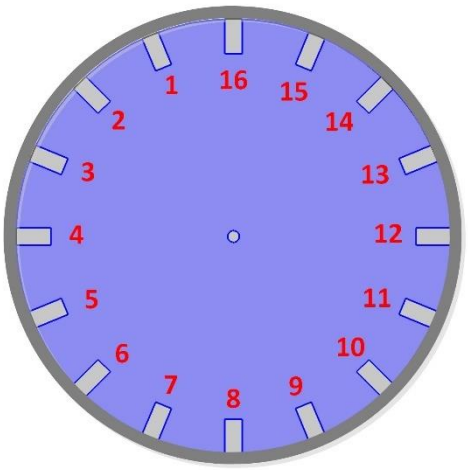

Figure 5-2 The electrode configuration model for the miniature EIT sensor

5.2.4 Cell-drug response monitoring in the microporous scaffold

In Chapter 4 , the experimental results indicate that EIT can monitor cell-drug response in tightly packed tumour spheroids. This method would be useful if it can be further developed for the monitoring of such a transient process in the microporous scaffolds as it is hard for optical-based methods to monitor cell activities in large samples with height and diameter at the millimetre scale [1]. Therefore, the potential of EIT to monitor the chemical insult of Triton X-100 to the sparse cells distributed in the AlgiMatrix scaffolds has been investigated in this subsection.

The schematic illustration of the experimental procedure for cell-drug response imaging is presented in Figure 5-3. Since the Triton X-100 lysis buffer has a different conductivity with the culture medium, its diffusion process resulted in a continuous conductivity variation in the sensing area, which may overlap with the conductivity variation due to the cell-drug response [119]. As a consequence, the culture medium and the Triton X-100 lysis buffer should be mixed before the chemical insult started. At t_0 , $900\mu l$ of the culture medium was added to the sensor. The system then started to take measurement simultaneously. Subsequently, $100\mu l$ of 10% Triton X-100 solution was aspirate to the sensor at t_1. In order to mitigate the influence of drug diffusion, the mixture of culture medium and Triton X-100 was facilitated by stirring at t_2 .

After a few minutes when the solution was stable, the scaffold sample and its blank control were separately transferred from the culture dishes to the second position of the sensor at t_3. According to previous studies [145, 157], Triton X-100 can kill the cancer cells within a few minutes. Therefore, the measurements were terminated at 10 minutes after t_3.

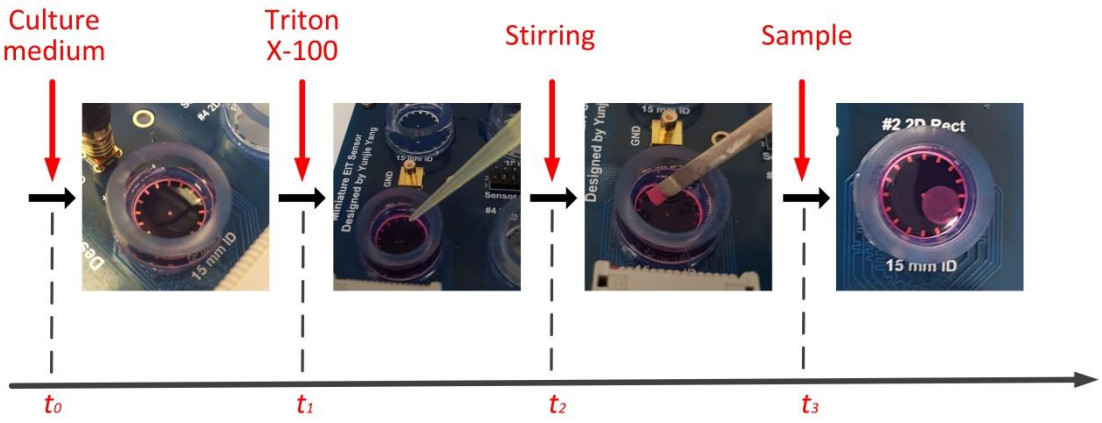

Figure 5-3 Schematic diagram of the experiment protocol

5.2.5 1D thresholding filter for voltage correction

EIT utilises 104 measurements to reconstruct an image. The abnormality in one or a few measurements will result in the unexpected anomalies in the reconstructed image. In order to avoid this problem, which occasionally occurred due to the errors in the data acquisition system, a one-dimensional (1D) thresholding filter was developed to pre-process the measurement data before image reconstruction. Since it would not have abrupt changes in the conductivities of the culture medium and the samples, the boundary voltage measurements should also be continuous in the time-domain. Any sudden changes in the boundary voltages were considered as errors. The filter was performed for each channel separately. The value of measurement v_1 was determined by the measurements in a given period.

$$v = [v_1, v_2, \cdots, v_n] \qquad \text{5-1}$$

where *v* is the voltage array for the measurements in this period, *n* is the size of the window.

If the difference between v_1 and the mean value of v is smaller than the standard deviation of v, v_1 is considered as a normal value and remains unchanged. Otherwise, v_1 is considered as an error and its value is set as the median value of v.

$$v_1 = \begin{cases} v_1 & |v - \bar{v}| < \sigma_v \\ \tilde{v} & otherwise \end{cases} \quad \textbf{5-2}$$

where $\bar{v}$ is the mean value of v, σ_v is the standard deviation of v and $\tilde{v}$ is the median value of v.

The median filter was applied to each frame and each channel of the data.

5.2.6 Total variation regularisation with the 2D median filter

In this chapter, the cells were encapsulated in the hydrogels and the scaffolds. Assuming that the cells were homogeneously distributed within the sample, the samples should have sharp conductivity changes on its boundary. Therefore, total variation regularisation (Eq. (2-34)) was adopted in this chapter for image reconstruction.

In miniature EIT, spike type artefacts commonly exist around the electrodes due to the high sensitivity [160]. These artefacts lead to background noise peaks in the images, and it may overwhelm the scaffold when the conductivity variation of the scaffold is small. In order to eliminate the background noise, a median filter was applied to the reconstructed conductivity distribution, which was formulated as:

$$\Delta\hat{\sigma} = median(\arg\min_{\Delta\sigma}(\frac{1}{2}\|\Delta V - J\Delta\sigma\|^2 + \lambda\|\Delta\sigma\|_{TV})) \quad \textbf{5-3}$$

where $median$ demotes the 5×5 median filter operator (Figure 5-4). The sliding window arranges the pixel value and its neighbours within the window from small to large and replaces the original value with the median value of the sorted array.

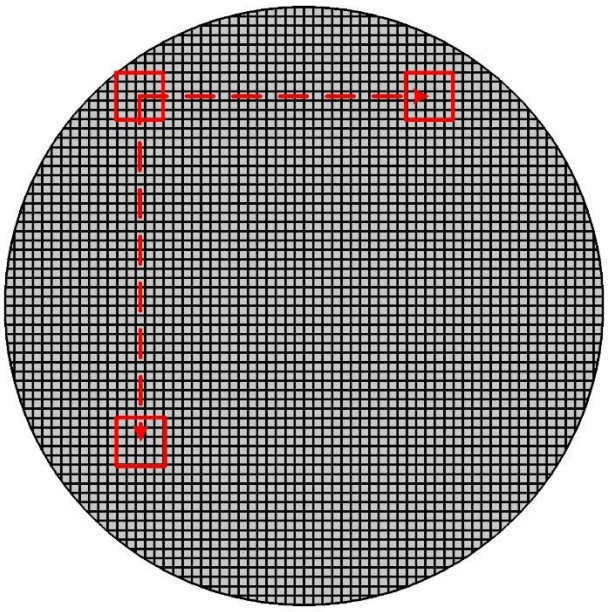

Figure 5-4 The median filter applied to each pixel

5.3 Results

5.3.1 Removal of the abnormal measurements

The voltage measurements for the cell-loaded scaffold sample in the first position were utilised to analyse the necessity and performance of the thresholding filter. The boundary voltages at channel 2, which was taken from electrode pair 5-6 when the current was injected from electrode pair 1-2, were presented in Figure 5-5. 207 measurements and 1198 measurements have been taken in 7 seconds when the frequencies of the stimulating current were 10 *kHz* and 100 *kHz*, respectively. At 10 *kHz*, the boundary voltage at channel 2 was 14.41 *mV* with a 0.09 *mV* variation. No significant error could be observed in the voltage array, so the thresholding filter only set the measurements with large noises, such as the first measurement at 15.18 *mV*, to the median value. The thresholding filter reduced the mean value of the voltage array by 0.003 *mV*, which was relatively small when compared to their original values. At 100 *kHz*, most of the measurements are around 8.08 *mV* with a 0.02 *mV* variation. The measurements occasionally jumped to 25 *mV*, however, they returned to the normal value in the next frame. The application

of thresholding filter removed all the abnormal high voltages and replaced them by the median value of the 1198 measurements. The mean value of the voltage array was therefore reduced by 0.17 *mV*. It shows that the filter helps to increase the accuracy of the measurement, and it is a benefit to EIT using either averaged values or single-frame voltages for image reconstruction.

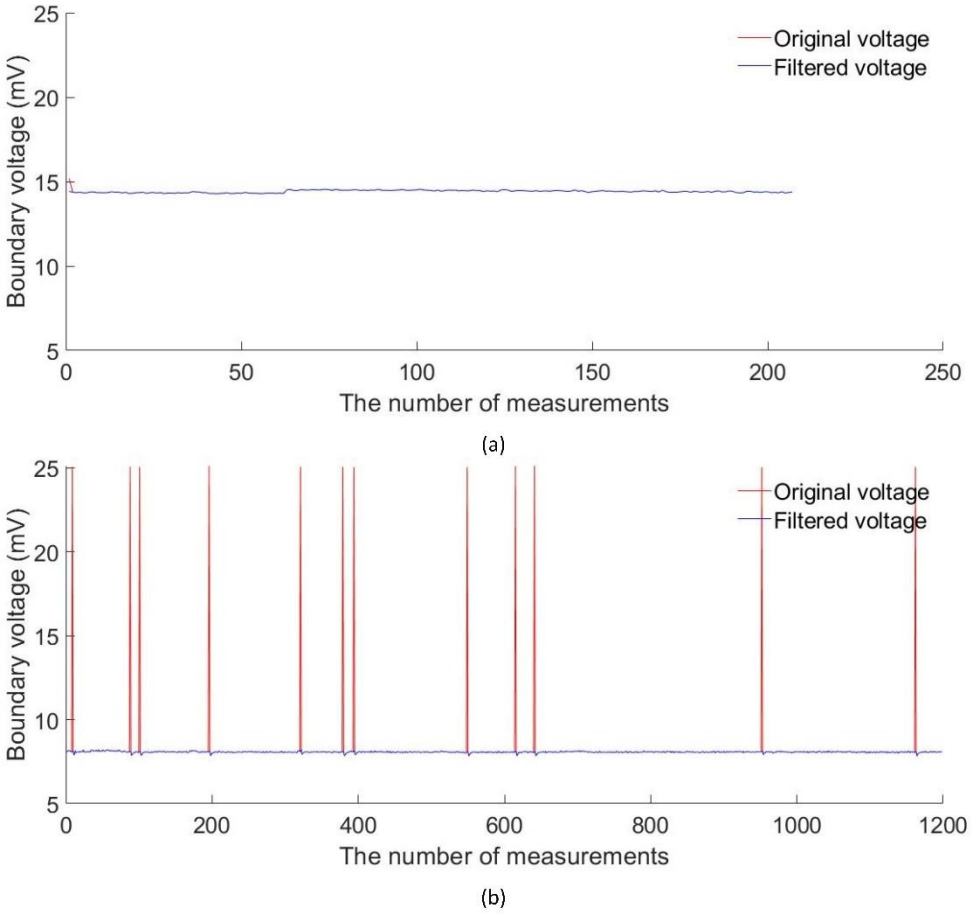

Figure 5-5 The boundary voltages (channel 2) for the scaffold sample in the first position at (a) 10 *kHz* and (b) 100 *kHz*

5.3.2 Time-difference image reconstruction

Figure 5-6 shows the images of the hydrogel sample and its blank control at two different positions. In Figure 5-6 (a) and (b), the positions of the samples are correctly displayed based on the conductivity variation in the related area. When no cells exist, the conductivity of the control group is slightly higher than that of the culture medium ,which can be observed in Figure 5-6 (c) and (d). Since the conductivity of the fresh culture medium is 2.13 *S/m*, the presence

of the cells reduces the local conductivity, and the conductivity of the sample is lower than that of the culture medium.

In Figure 5-7 (a) and (b), the conductivity of the cell-loaded scaffold sample is lower than that of the culture medium as expected. The conductivity variation of the blank scaffold cannot be observed in Figure 5-7 (c) and (d), which indicates that the empty scaffold had the same conductivity as the culture medium. Therefore, the AlgiMatrix Scaffold is more suitable for the applications using EIT as the variation of the local conductivity distribution is mainly attributed to the presence of cells.

Comparing Figure 5-6 with Figure 5-7, the images for the scaffolds have smaller background noise than those in the images for hydrogels. One possible reason is the accuracy of culture medium absorption. Due to the irregular shape of hydrogel samples, it was difficult to calculate their volume accurately, so the culture medium absorption was based on an approximate value. For this reason, the models for the hydrogel imaging were not as accurate as those for the scaffold imaging, and the background errors increased. It once again emphasises the importance of maintaining a constant liquid volume during the miniature EIT measurements.

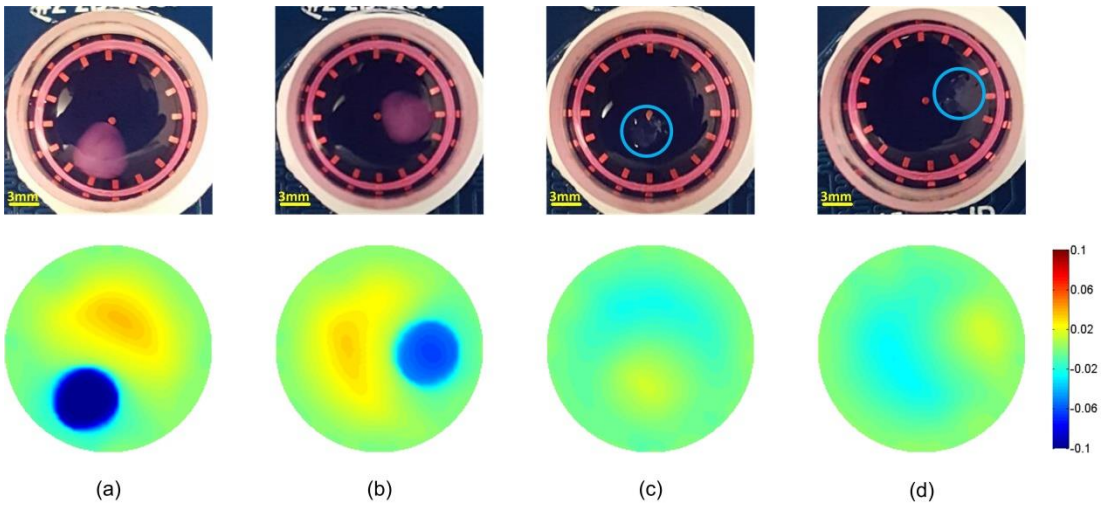

Figure 5-6 Time-difference images for the cell-loaded hydrogel sample at (a) positions 1, (b) position 2 (b) and the blank hydrogel at (c) positions 1 and (d) position 2.

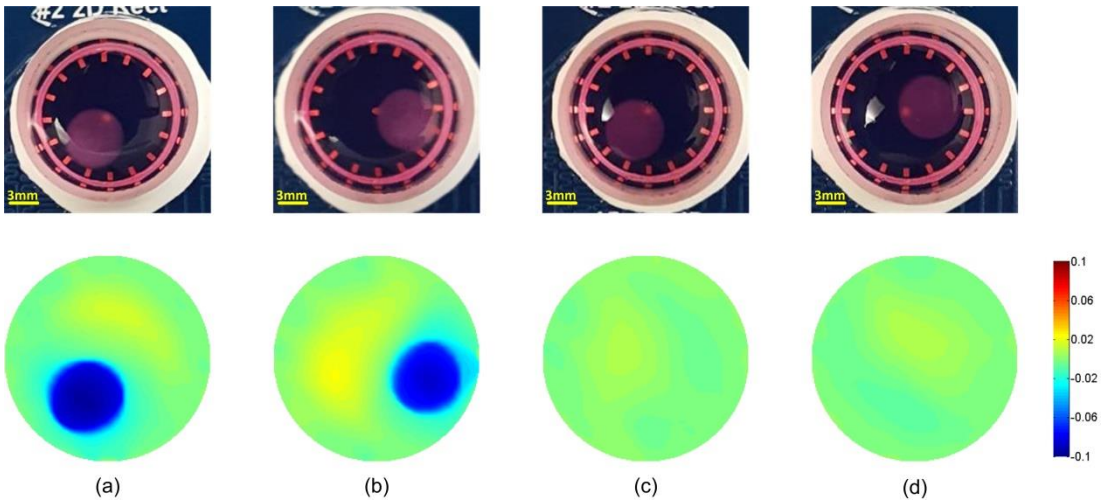

Figure 5-7 Time-difference images for the cell-loaded scaffold sample at (a) positions 1, (b) position 2 (b) and the blank scaffold at (c) positions 1 and (d) position 2.

5.3.3 Frequency-difference image reconstruction

Figure 5-8 and Figure 5-9 show the frequency-difference images for the cell-loaded hydrogel samples and scaffold samples as well as their blank controls, respectively. Surprisingly, the images only show unexpected anomalies near electrode 1 to 3 instead of the conductivity variations in the miniature EIT sensor. Unlike the results in Section 3.3.2, FDEIT fails to distinguish the samples and their blank controls, which should have different electrical properties. A possible explanation for these results may be the small conductivity variation of the samples, which is overwhelmed by the larger measurement errors. As mentioned in Section 2.4.2, the ability of FDEIT to eliminating the common errors is not as good as that of TDEIT. The utilisation of the miniature sensor will increase the measurement errors, so it may result in the failure in image reconstruction if the changes in the samples are relatively small. These results show the limitation of conventional FDEIT for miniature tissue culture monitoring. Hence, the cell-drug response monitoring in the next section will only utilise the TDEIT. A detailed analysis of the measurement errors and methods to improve the FDEIT will be presented in Chapter 6 .

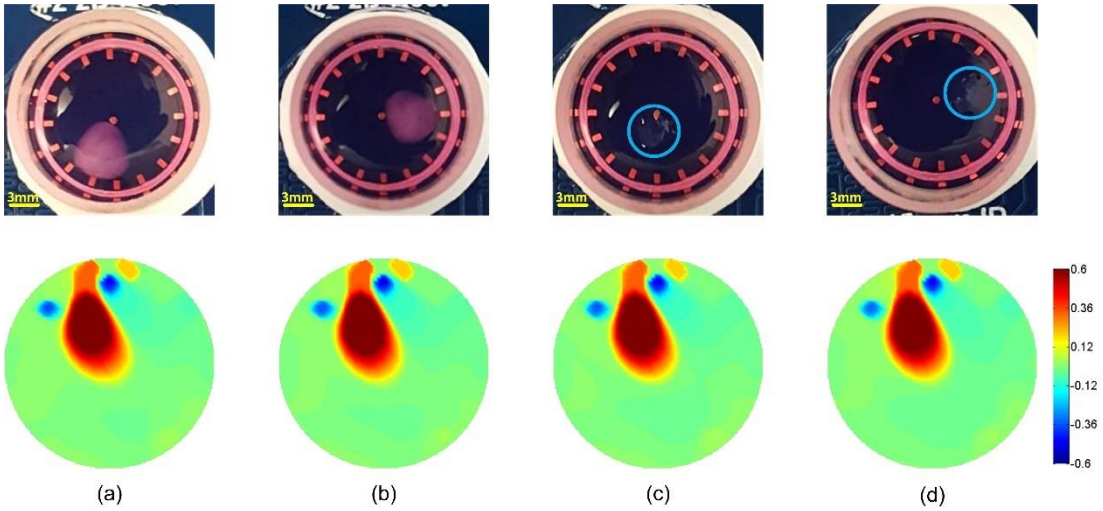

Figure 5-8 Frequency-difference images for the cell-loaded hydrogel sample at (a) positions 1, (b) position 2 (b) and the blank hydrogel at (c) positions 1 and (d) position 2.

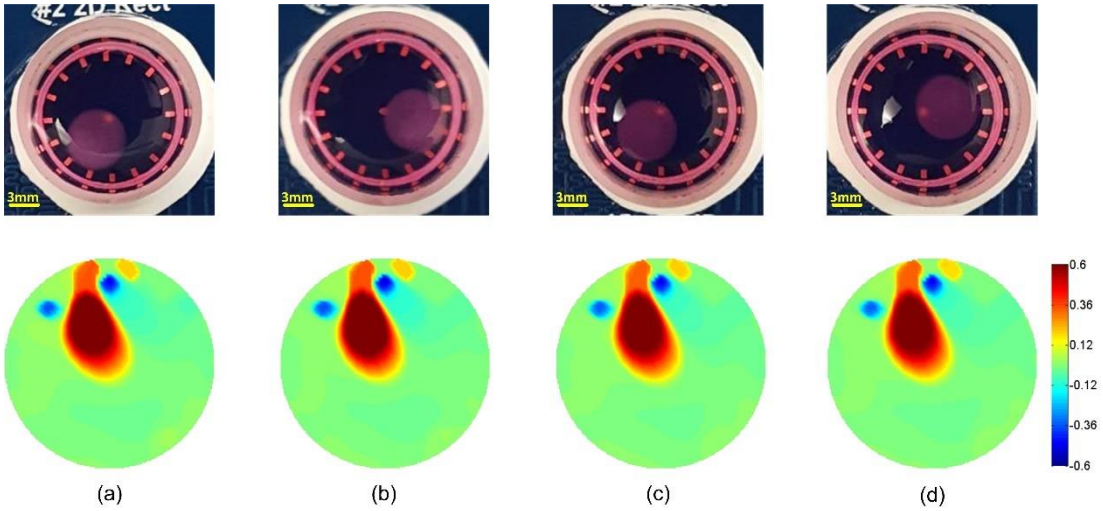

Figure 5-9 Frequency-difference images for the cell-loaded scaffold sample at (a) positions 1, (b) position 2 (b) and the blank scaffold at (c) positions 1 and (d) position 2.

5.3.4 Monitoring the cell-drug response in the microporous scaffold

Figure 5-10 shows the time sequence of the boundary voltages at channel 78, which was taken from electrode pair 10-11 when the current was injected from electrode pair 8-9. In both the cell-loaded scaffold sample and its blank control, the voltage variation was almost the same before the introduction of the scaffold at t_3. After adding Triton X-100 to the sensor, the boundary voltage

dropped for the first time then gradually increased. After the stirring process at t_2, the boundary voltages become stable again. The introduction of the scaffold to the sensor caused a drop on the boundary voltages. In the control group, the boundary voltage remained constant after the voltage drop. However, the boundary voltage for the scaffold sample increased continuously until the end of the experiment.

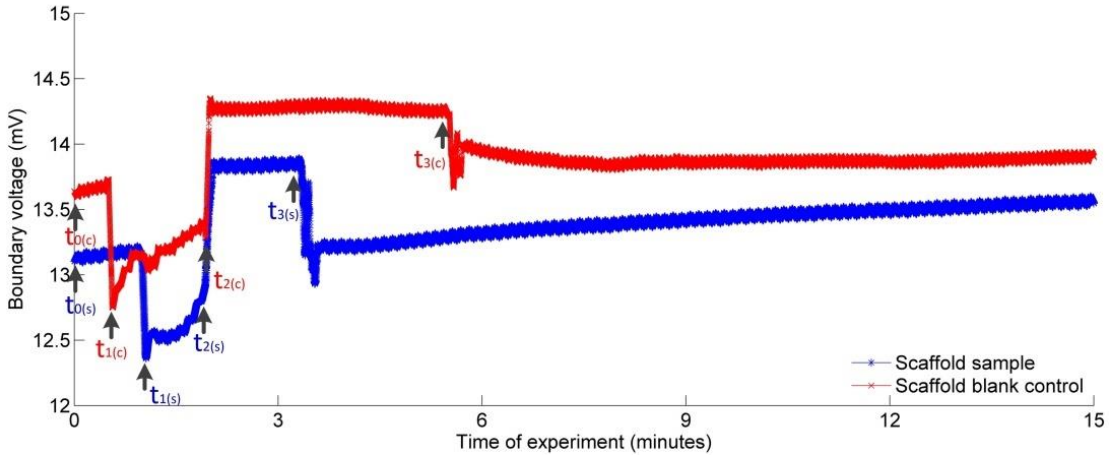

Figure 5-10 Boundary voltages of the 78th measurement (electrode 8- 9 as current injection and electrode 9-10 as measurement)

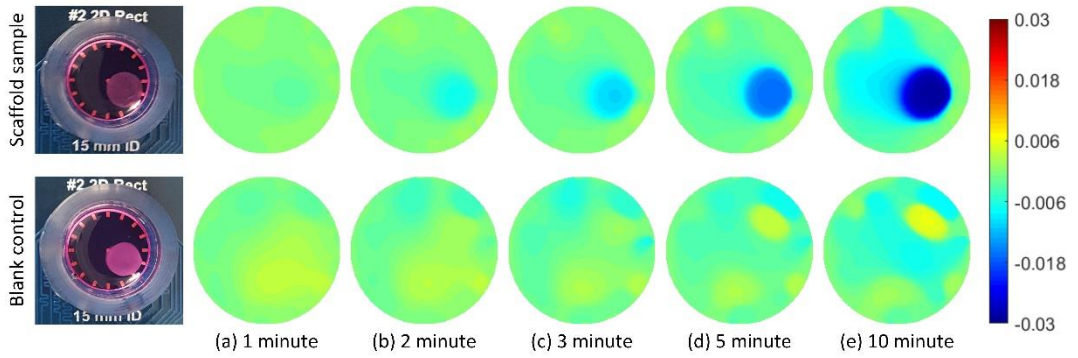

Figure 5-11 Conductivity variations of the cell-loaded scaffold sample and the blank control at (a) 1 minute after t_3, (b) 2 minute after t_3, (c) 3 minute after t_3, (d) 5 minute after t_3 and (e) 10 minute after t_3.

The reconstructed images at selected time points are demonstrated in Figure 5-11. In order to highlight the conductivity variation caused by the cell-drug response, the reference voltages were taken at t_3. In the blank control, the

boundary of the scaffold cannot be identified. The maximum conductivity change in the reconstructed images is about 0.7%, which is most likely due to the measurement noise. It shows that the conductivity of the empty scaffold is almost static after t_3. In the experimental group, a clear conductivity drop occurs at the position of the scaffold sample. The conductivity of the scaffold sample decreases from 0.36% in the first minute to 3.17% after ten minutes.

Although EIT successfully distinguishes the sample from its blank control, the conductivity variation of the sample is different from those observed in Section 4.3.2. The conductivity of the cells should increase when the cell membranes are resolved by Triton X-100, but the overall conductivity of the scaffold sample decreases in this experiment. Therefore, conductivity variations besides the cell mortality simultaneously occurred within the scaffold.

Since there is a continuous nutrient and gas exchange between the cytoplasm and the extracellular culture medium during the cell culture [161], a possible explanation for the unexpected conductivity variation might be the change in background conductivity. In order to verify this factor, the conductivity of the fresh culture medium and the spent culture medium after one-day culture of the scaffold samples were compared. 10 ml fresh culture medium and spent culture medium were collected to the 50 *ml* centrifugation tubes and were measured, respectively, using conductivity meter Sension+EC5. The results showed that the conductivity of the fresh culture medium was 2.13 *S/m* at room temperature. The conductivity of the spent culture medium was 2.20 *S/m* at room temperature, which was 3.28% higher than that of the fresh culture medium. After placing the scaffold sample to the sensor, the molecular in the fresh culture medium would exchange with the spent culture medium in the scaffold, causing a drop in the sample conductivity. If this change is more significant than the conductivity variation caused by the chemical insult, it is possible to observe the decrease of the sample conductivity over time. This is the main reason why the result in Figure 5-11 is different from the conductivity changes in Figure 4-7.

5.4 Discussions

Overall, the conductivity variation due to the cells distributed in hydrogels and scaffolds can be detected by the impedance measurements. Due to the low cell concentration, the conductivity variations of the samples were not as significant as those of the tightly packed cell spheroids. Therefore, the measurement errors and the molecule exchange of the culture medium caused non-neglectable disturbance to the reconstructed images.

The majority of the measurements were corresponding to the conductivities within the sensing area, but abnormal measurements occasionally occur with extremely high voltages. The abnormal measurements were likely to appear at high frequencies although there weren't any rules for their appearance. It was difficult to explain this result, but it might be related to the malfunction of the multiplexer array. In the Agile Tomography system, the temporal resolution was higher at high frequencies and it cannot be controlled manually. Working at a high temporal resolution mode when the speed was over 100 fps, the multiplexer array might fail to switch to the correct channel before the measurement was taken, and it caused the unexpected high voltages in the measurements. The abnormal measurements were much larger than the general boundary voltages, so they could be corrected by the thresholding filter.

The conductivity of the culture medium changed during the cell culture due to cell breathing and metabolism. Since both the conductivity of the cells and the conductivity of the culture medium changed during the experiment, it was difficult for TDEIT to extract the conductivity variation due to the cell mortality from the background disturbance. Therefore, FDEIT should be developed for long-term tissue culture monitoring by directly demonstrating the cell concentration and cell viability through the membrane characteristics. Since the results also show the drawback of FDEIT in common error elimination, an advanced calibration method should be developed to remove the unexpected components in the boundary voltage measurements.

5.5 Summary

The hydrogels and scaffolds provide more physiologically relevant microenvironments for cells to form natural shapes and intercellular contacts. Monitoring the tissue-engineered samples provides information regarding the morphological and functional behaviour of the cell cultures. In this chapter, the EIT method developed for the tumour spheroid imaging has been expanded for the tissue engineering applications. Static imaging results were compared with the phantom study in Chapter 3 and the dynamic cell-drug response monitoring data were compared with the results in Chapter 4 , which proposed to explain the errors in the images for tissue-engineered samples. In the next chapter, equivalent circuit models will be developed to analyse the errors in EIT measurements, and a calibration method will be derived to remove the errors before image reconstruction.

Chapter 6 Calibrated FDEIT for long-term 3D tissue culture monitoring

6.1 Introduction

The field of tissue engineering has been developed in the past 20 years to meet the tremendous need for organs and tissues [154, 162, 163]. In tissue engineering, the human cells are seeded and cultured in a variety of bioscaffolds to generate artificial tissues and organs in vitro, which usually take a couple of weeks until they can be used for transplantation.

Previous studies showed that time-difference EIT could be applied in different biological applications to monitor the transient response of biological tissues. However, this method is only suitable for short-term monitoring due to factors such as temperature variation, evaporation and cellular activities change the conductivity of the background culture medium, which makes the reference unavailable for further image reconstruction [164, 165]. Alternatively, the frequency-difference EIT could be used to reflect the physiological conditions of the biological tissues by reconstructing the conductivity distribution in terms of frequency-dependent behaviour. It does not require a temporal reference, but the frequency-dependent circuitry artefacts introduce different errors to the measurements at two frequencies and the differentiation method is not able to fully eliminate the errors [166, 167]. Recently, a background calibration method has been developed for a relevant technique [168], it is worth to use it as a reference for the development of miniature FDEIT calibration.

In this chapter, an equivalent circuit model was developed to analyse the EIT measurements, and the corresponding equations were derived to indicate the relationship between the boundary voltages and the circuitry errors. Based on the model, the calibrated FDEIT method was developed to eliminate the errors that existed in the boundary voltages and to improve the image quality of the images for 3D tissue culture. A joint simulation method combining FEM EIT modelling and SPICE circuit simulation was developed for the first time to

analyse the measurement errors in EIT. Simulations and experiments with two types of bioscaffolds were carried out to verify the equivalent circuit model and the performance of the proposed method. In order to investigate the feasibility of CFDEIT in long-term tissue culture monitoring, experiments with inaccurate reference were also performed.

6.2 Methods

6.2.1 The voltage measurement of EIT

The measurement of EIT was based on the four-electrode measurement strategy. Using the adjacent current drive method, the current was injected to the sensor through a pair of adjacent electrodes, and the corresponding voltage variation was measured from the other adjacent electrode pairs. The equivalent circuit diagram of a single channel EIT measurement is demonstrated in Figure 5-4. The stimulating current I_0 is generated from the current source and injected into the sensor through channel 1 and 2 while the boundary voltage drop between channel 3 and 4 is measured through the voltmeter in the EIT system. $Z_1 = R_1 // C_1$, $Z_2 = R_2 // C_2$, $Z_3 = R_3 // C_3$ and $Z_4 = R_4 // C_4$ are the contact impedance between electrodes and the culture medium, respectively, where $//$ indicates the parallel connection between two components. $Z_{14} = R_{14} // C_{14}$ and $Z_{23} = R_{23} // C_{23}$ are the edge impedance between the channel 1-4 and 2-3 while $Z_m = R_m // C_m$ is target impedance to be measured. Theoretically, this measurement strategy eliminates the effect of the contact impedance, and the voltage measurement is directly related to the target impedance:

$$V = I_0 Z_m \qquad \textbf{6-1}$$

However, the input of the voltmeter is a virtual ground, and the capacitive coupling between the voltmeter terminals to the virtual ground $Z_x = 1/\, j\omega C_x$ and $Z_y = 1/\, j\omega C_y$ will divert some leakage current around the voltmeter [169, 170]. Hence, in practical measurement, the voltage measurement is not only

determined by the value of target impedance Z_m but also affected by the leakage current and the contact impedance. By applying the Kirchhoff's law to the equivalent circuit in Figure 6-1, the voltage measured at the voltmeter can be calculated as:

$$V = I_2(Z_3 + Z_4 + Z_m) - I_1 Z_4 - I_3 Z_3 \quad \textbf{6-2}$$

where I_1 is the current at Kirchhoff's Loop $Z_1 \to Z_{14} \to Z_4 \to Z_y$, I_2 is the current at Kirchhoff's Loop $Z_4 \to Z_m \to Z_3 \to Z_x \to Z_y$ and I_3 is the current at Kirchhoff's loop $Z_3 \to Z_{23} \to Z_2 \to Z_x$.

The relationship between I_1, I_2 and I_3 can be described by the Kirchhoff's Voltage Law (KVL):

$$I_2(Z_3 + Z_4 + Z_x + Z_y + Z_m) - I_1(Z_4 + Z_y) - I_3(Z_3 + Z_x) = 0 \quad \textbf{6-3}$$

$$I_3(Z_2 + Z_3 + Z_{23} + Z_x) - I_2(Z_3 + Z_x) = 0 \quad \textbf{6-4}$$

The combination of 6-3 and 6-4 can be written as:

$$I_2 = \frac{(Z_3 + Z_x)}{(Z_2 + Z_3 + Z_{23} + Z_x)} I_3 \quad \textbf{6-5}$$

$$I_1 = \frac{(Z_3 + Z_x)(-Z_2 + Z_4 - Z_{23} + Z_y + Z_m)}{(Z_4 + Z_y)(Z_2 + Z_3 + Z_{23} + Z_x)} I_3 \quad \textbf{6-6}$$

Therefore, the voltage measurement in 6-2 can be simplified by 6-5 and 6-6 as below:

$$V = \left(\frac{(Z_3 + Z_x)(Z_3 + Z_4 + Z_m) - Z_4(-Z_2 + Z_4 - Z_{23} + Z_y + Z_m)\dfrac{(Z_3 + Z_x)}{(Z_4 + Z_y)}}{(Z_2 + Z_3 + Z_{23} + Z_x)} - Z_3 \right) I_3 \quad \textbf{6-7}$$

Assuming $Z_x = Z_y$ and the impedance of capacitive coupling is much higher than the contact impedance and edge impedance, 6-7 can be approximated to:

$$V = ((Z_4 - Z_3) + Z_m + \frac{Z_3 Z_3 + Z_3 Z_x - Z_4 Z_4 - Z_4 Z_y}{Z_x}) I_3 \quad \textbf{6-8}$$

6.2.2 Error elimination in frequency-difference EIT measurements

The performance of simple FDEIT is usually poorer than that of simple TDEIT as difference imaging cannot completely remove the measurement errors that vary at different frequencies [122]. As a consequence, weighted FDEIT has been developed to hold the anomaly information while eliminating the background information:

$$\Delta V = V_{m-2} - \alpha V_{m-1} \quad \textbf{6-9}$$

$$\alpha = \langle V_{m-2}, V_{m-1} \rangle / \langle V_{m-1}, V_{m-1} \rangle \quad \textbf{6-10}$$

where V_{m-1} is the voltage at the first frequency f_1, V_{m-2} is the voltage at the second frequency f_2, α is the optimal weight factor and <·,·> is the inner production operator:

$$V_{m-1} = ((Z_{4\text{-}1} - Z_{3\text{-}1}) + Z_{m-1} + \frac{Z_{3-1} Z_{3-1} + Z_{3-1} Z_{x-1} - Z_{4-1} Z_{4-1} - Z_{4-1} Z_{y-1}}{Z_{x\text{-}1}}) I_{3\text{-}1} \quad \textbf{6-11}$$

$$V_{m-2} = ((Z_{4\text{-}2} - Z_{3\text{-}2}) + Z_{m-2} + \frac{Z_{3-2} Z_{3-2} + Z_{3-2} Z_{x-2} - Z_{4-2} Z_{4-2} - Z_{4-2} Z_{y-2}}{Z_{x\text{-}2}}) I_{3\text{-}2} \quad \textbf{6-12}$$

The combination of 6-9, 6-11 and 6-12 shows the relationship between the boundary voltage variation and the changes of conductivity:

$$\Delta V = (Z_{m-1} I_{3\text{-}1} - \alpha Z_{m-2} I_{3\text{-}2}) + ((Z_{4\text{-}1} - Z_{3\text{-}1}) I_{3\text{-}1} - \alpha (Z_{4\text{-}2} - Z_{3\text{-}2}) I_{3\text{-}2}) + \left(\frac{(Z_{3-1} Z_{3-1} + Z_{3-1} Z_{x-1} - Z_{4-1} Z_{4-1} - Z_{4-1} Z_{y-1}) I_{3\text{-}1}}{Z_{x\text{-}1}} - \frac{\alpha (Z_{3-2} Z_{3-2} + Z_{3-2} Z_{x-2} - Z_{4-2} Z_{4-2} - Z_{4-2} Z_{y-2}) I_{3\text{-}2}}{Z_{x\text{-}2}} \right) \quad \textbf{6-13}$$

Due to the capacitive coupling, the subtraction fails to compensate the common errors in the voltage measurement and the boundary voltage variation relates to not only the changes of target impedance but also the changes of the contact impedances at the measuring electrodes, coupling capacitance and the feedback current.

Since the contact impedance and coupling capacitance are identical at the same frequency, performing a system calibration at each selected frequency is a method to cancel out the variation of measurement errors. References are needed to be taken with homogeneous culture medium at f_1 and f_2, giving boundary voltages V_{r-1} and V_{r-2}:

$$V_{r-1} = ((Z_{4\text{-}1} - Z_{3\text{-}1}) + Z_{m-3} + \frac{Z_{3-1} Z_{3-1} + Z_{3-1} Z_{x-1} - Z_{4-1} Z_{4-1} - Z_{4-1} Z_{y-1}}{Z_{x\text{-}1}}) I_{3\text{-}1} \quad \textbf{6-14}$$

$$V_{r-2} = ((Z_{4\text{-}2} - Z_{3\text{-}2}) + Z_{m-4} + \frac{Z_{3-2} Z_{3-2} + Z_{3-2} Z_{x-2} - Z_{4-2} Z_{4-2} - Z_{4-2} Z_{y-2}}{Z_{x\text{-}2}}) I_{3\text{-}2} \quad \textbf{6-15}$$

where Z_{m-3} and Z_{m-4} are the target impedance for the homogeneous culture medium at f_1 and f_2,respectively.

The variation of measurement errors between f_1 and f_2 can therefore be calculated by the subtraction between V_{r-1} and V_{r-2}, so subtraction between V_m and V_r gives the boundary voltages without measurement errors:

$$
\begin{aligned}
\Delta V &= (V_{m-2} - V_{r-2}) - (V_{m-1} - V_{r-1}) \\
&= (((\mathrm{Z}_{4\text{-}2} - Z_{3\text{-}2}) + Z_{m-2} + \frac{\mathrm{Z}_{3-2}Z_{3-2} + Z_{3-2}\mathrm{Z}_{x-2} - Z_{4-2}Z_{4-2} - Z_{4-2}Z_{y-2}}{\mathrm{Z}_{x\text{-}2}})I_{3\text{-}2} \\
&\quad - ((\mathrm{Z}_{4\text{-}2} - Z_{3\text{-}2}) + Z_{m-4} + \frac{\mathrm{Z}_{3-2}Z_{3-2} + Z_{3-2}\mathrm{Z}_{x-2} - Z_{4-2}Z_{4-2} - Z_{4-2}Z_{y-2}}{\mathrm{Z}_{x\text{-}2}})I_{3\text{-}2}) \\
&\quad - (((\mathrm{Z}_{4\text{-}1} - Z_{3\text{-}1}) + Z_{m-1} + \frac{\mathrm{Z}_{3-1}Z_{3-1} + Z_{3-1}\mathrm{Z}_{x-1} - Z_{4-1}Z_{4-1} - Z_{4-1}Z_{y-1}}{\mathrm{Z}_{x\text{-}1}})I_{3\text{-}1} \\
&\quad - ((\mathrm{Z}_{4\text{-}1} - Z_{3\text{-}1}) + Z_{m-3} + \frac{\mathrm{Z}_{3-1}Z_{3-1} + Z_{3-1}\mathrm{Z}_{x-1} - Z_{4-1}Z_{4-1} - Z_{4-1}Z_{y-1}}{\mathrm{Z}_{x\text{-}1}})I_{3\text{-}1}) \\
&= (Z_{m-2} - Z_{m-4})I_{3\text{-}2} - (Z_{m-1} - Z_{m-3})I_{3\text{-}1}
\end{aligned}
\qquad \textbf{6-16}
$$

6-16 shows the boundary voltage variation only relates to the changes in the target impedance after error compensation. Although the conductivity variation between the medium of the sample and the reference may generate background error, it can be reduced by the normalisation of the boundary voltages, which gives the equation of calibrated frequency-difference EIT (CFDEIT):

$$
\Delta V = \frac{(V_{m-2} - (V_{r-2} - V_{r-1})) - V_{m-1}}{V_{m-1}} \qquad \textbf{6-17}
$$

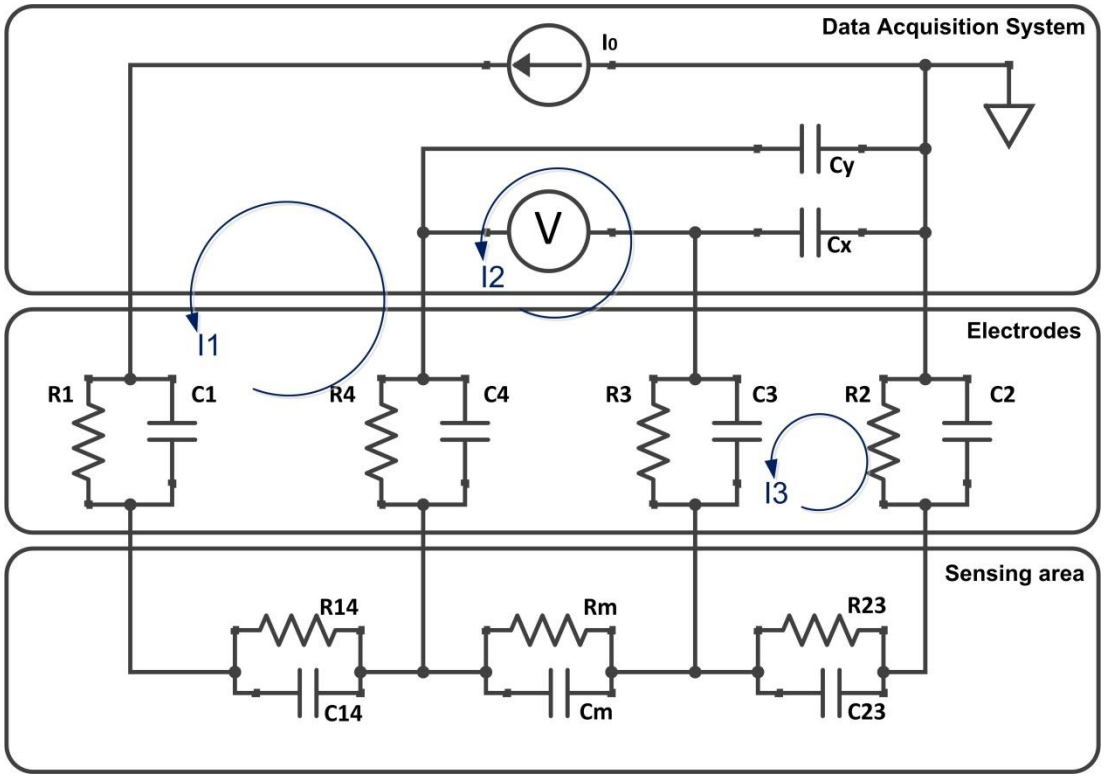

Figure 6-1 Equivalent circuit model for a single channel EIT measurement with the adjacent current drive method

6.2.3 Evaluation of calibration performance

To evaluate the performance of the calibration methods, correlation coefficient (CC) of the reconstructed images were calculated, which quantifies the similarity between the true images and the reconstructed images:

$$CC = \frac{\sum_{i=1}^{n}(\hat{\sigma}_i - \bar{\hat{\sigma}})(\sigma_i - \bar{\sigma})}{\sqrt{\sum_{i=1}^{n}(\hat{\sigma}_i - \bar{\hat{\sigma}})^2 \sum_{i=1}^{n}(\sigma_i - \bar{\sigma})^2}} \qquad \text{6-18}$$

where $\hat{\sigma}$ and σ are the reconstructed and true conductivity variation while $\bar{\hat{\sigma}}$ and $\bar{\sigma}$ are their mean value, respectively. A higher CC means the reconstructed image is more similar to the true image and therefore has a higher image quality.

6.2.4 Tissue sample formation

MCF-7 breast cancer cells were used as the samples in this study. The cells were routinely cultured in monolayer in the culture medium introduced in Section 5.2.1. They were then seeded to the 96-well AlgiMatrix scaffolds (Life Technologies, CA, USA) and HyStem-HP hydrogel (Sigma-Aldrich, St. Louis, MO, USA) using the methods demonstrated in Section 5.2.2 at one day prior to the experiment. Blank hydrogels and scaffolds without cells were also prepared as the control group. Microscopic images were taken for the samples and blank controls using VisiCam 3.0. Figure 6-2 shows that the cells were successfully seeded into both the hydrogel samples and the pores of the scaffold samples.

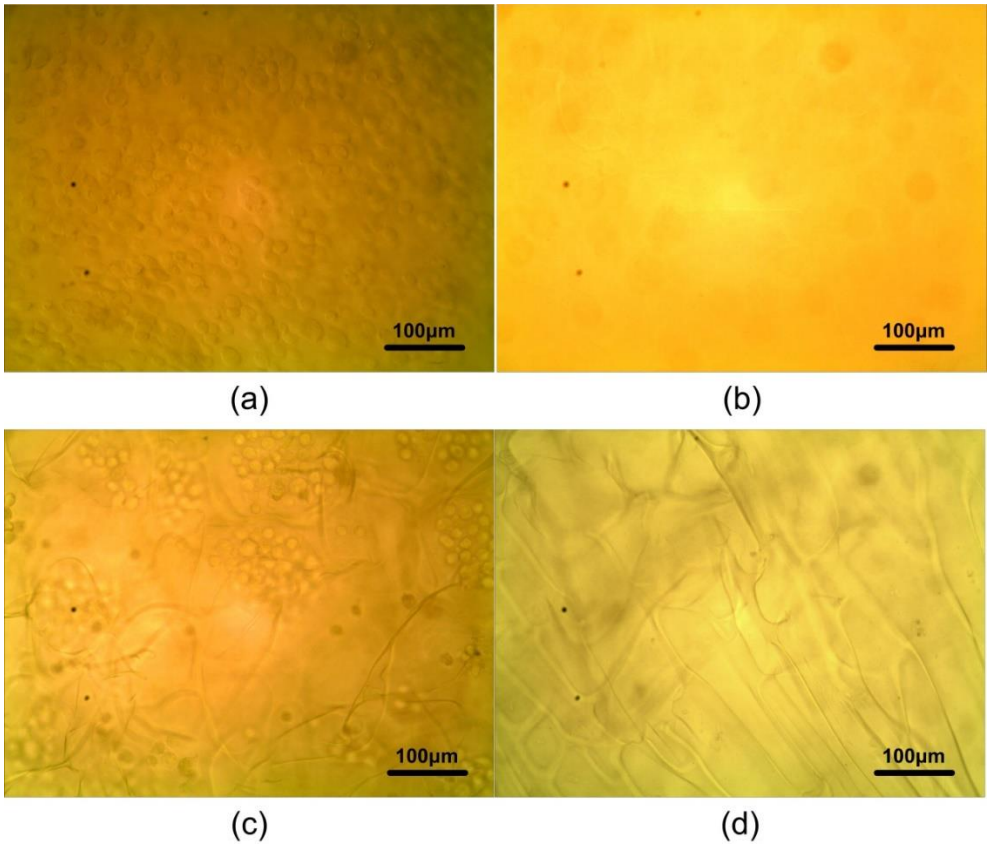

Figure 6-2 The microscopic images for HyStem-HP hydrogel (a) with and (b) without cells, and AlgiMatrix scaffold (c) with and (d) without cells

6.2.5 Phantom modelling

The miniature EIT sensor model was built for the simulations using COMSOL Multiphysics. As shown in Figure 6-3, the model was developed based on the size and the structure of the sensor. Considering that only 1.2 *ml* culture medium was added to the chamber during cell culture, the height of the chamber was set to 7 *mm*. A cylindrical scaffold sample with 4 *mm* and 2 *mm* in diameter and height, respectively, was introduced to the bottom of the sensor at position (11.5, 7.5), where position (x, y) was the horizontal coordinate. In this study, I assumed the cells were evenly distributed inside the scaffold, so the conductivity of the sample was homogeneous.

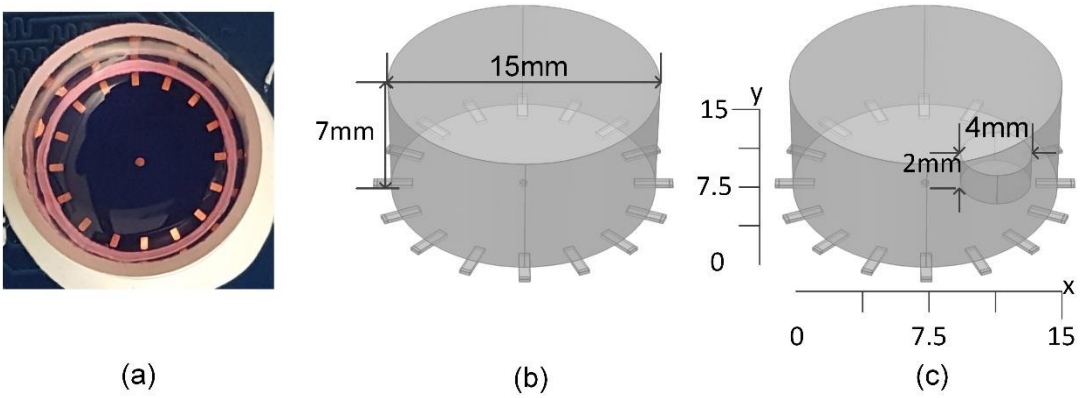

Figure 6-3 Picture of (a) the manufactured miniature EIT sensor, (b) the homogeneous sensor model and (c) the position of the tissue sample in this simulation

6.2.6 EIT measurement through FEM modelling and circuit simulation

Conventional EIT simulations are mainly carried out with EIT simulators or Multiphysics software, such as EIDORS [171, 172] and COMSOL Multiphysics [173, 174]. With the input of the structure of sensing area, sensor location and the conductivity distribution within the sensing area, these kinds of software help to calculate the boundary voltages corresponding to the stimulating currents through finite element method (FEM) modelling. Ideal current sources and voltmeters are adopted in these simulations, and the boundary voltages only relate to the conductivity distribution in the sensing area. It provides preliminary data to evaluate the feasibility of EIT for new applications, but the effect of measurement errors introduced by the system are neglected in these

studies. Circuit simulation tools, such as SPICE tools, are capable of noise performance simulations on linear elements (RLC components) and complex semiconductor devices. However, these tools are only designed for the simulations of circuit components, so they have not yet been used for EIT simulations.

In fact, the subject for EIT experiments can be considered as a passive impedance network composed of linear elements [175]. The equivalent impedance between two electrodes can be obtained through the conventional EIT simulations. In order to evaluate the circuitry errors to the EIT measurements, a joint simulation method combining FEM EIT modelling and SPICE circuit simulation was developed in this study. A FEM mesh was first constructed for the sensor and the scaffold sample through COMSOL Multiphysics. The equivalent impedance network for the sensor was calculated using Ohm's Law by injecting the unit current to the sensor and measuring the corresponding boundary voltages. The measuring circuit shown in Figure 6-1 was then developed in LTspice and the edge impedance and target impedance Z_{14}, Z_{23} and Z_m were replaced by the equivalent impedance network. This process is demonstrated in Figure 6-4. The errors in the measurements can be introduced to the simulation by adjusting the contact impedance and coupling capacitance.

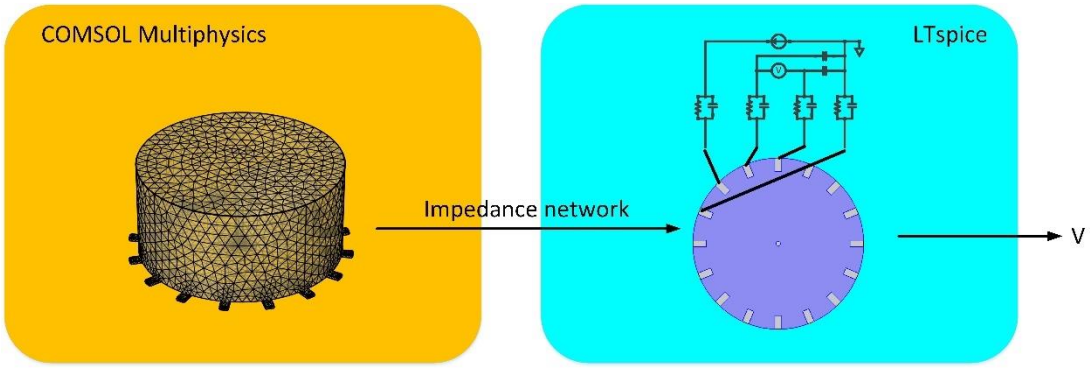

Figure 6-4 Proposed joint simulation using COMSOL Multiphysics and LTspice

6.2.7 Experiment settings for the evaluation of CFDEIT

Experiments were taken at 24 hours after cell seeding. 1.2 *ml* culture medium was added to the sensor, and the references were taken at 10 *kHz* and 100 *kHz*, respectively. The cell-loaded hydrogel samples, scaffold samples and their blank controls were transfer to the miniature EIT sensor, respectively, and the same volume of culture medium was absorbed using the pipette to maintain the liquid volume in the sensor. The measurements for the samples and their blank controls were taken with the FDEIT method demonstrated in Section 5.2.3. In order to evaluate the performance of CFDEIT in long-term tissue culture monitoring, another reference group was taken when the sensor was filled with 1.2 *ml* phosphate-buffered saline (PBS) to simulate the change of background conductivity due to the cell breathing and metabolism.

6.3 Results

6.3.1 Simulation results

Simulations were performed in the miniature sensor model to evaluate the effect of leakage current to the voltage measurement and the performance of the proposed CFDEIT method. The model of the sensor was developed in COMSOL Multiphysics as demonstrated at Section 6.2.5. The frequency-independent background conductivity was set to $\sigma_{bg} = 2\,S/m$ and the conductivity of the scaffold sample was 1 *S/m* and 1.2 *S/m* at $f_1 = 10kHz$ and $f_2 = 100kHz$, respectively. The contact impedances were set to the same ($R_1 = R_2 = R_3 = R_4 = 20\Omega$) and the coupling capacitances were identical ($C_x = C_y$).

6.3.1.1Single-channel evaluation

The single-channel evaluation was performed at $100kHz$ in the sensor model with a scaffold sample (Figure 6-3(c)). $I_0 = 1\,mA$ was injected into the sensor through electrode pair 9-10 while the boundary voltage was measured at electrode pair 16-1, where the target impedance $Z_m = 19.519\,\Omega$. By changing

the value of contact impedance and the coupling capacitance, the corresponding boundary voltage is shown in Table 1. The red numbers indicate the significant changes referred to the default setting in the second row.

When coupling capacitance did not exist, the boundary voltage was equal to the product of stimulation current and the target impedance as expected. As can be seen in row 2 and 5, the presence of coupling capacitances reduces the boundary voltages, and larger coupling capacitances cause more significant effects. Row 3 shows the increase of contact impedance Z_3 results in the increase of the boundary voltage *V*, but *V* is almost invariable if Z_3 and Z_4 has the same change. Finally, changing the contact impedance of Z_1 and Z_2 didn't cause an apparent variation in the boundary voltage.

Overall, the results match the proposed equation (6-8). The current travelled through the impedance network through channel 1 and channel 2 when coupling capacitance did not exist, so there was no current that went through contact impedance Z_3 and Z_4. Hence, boundary voltage was equal to the product of stimulation current and the target impedance. When coupling capacitances were presented in the circuit, some current was diverted to ground through the measuring channel 3 and 4, resulting in the drop of I_3. Therefore, the boundary voltage was lower than the expected value. The increase of contact impedance Z_3 changed the total impedance measured by the voltmeter, so the boundary voltage became higher than the expectation. However, this change would be compensated by the increase of contact impedance Z_4, so the boundary voltage measurement was almost invariable if Z_3 and Z_4 had the same change. The change of contact impedances Z_1 and Z_2 didn't affect the boundary voltage as they did not exist in Eq. (6-8).

Table 6-1 Single channel boundary voltage measurement corresponding to different impedance artefacts

$Z_1(\Omega)$	$Z_2(\Omega)$	$Z_3(\Omega)$	$Z_4(\Omega)$	$Z_{14}(\Omega)$	$Z_{23}(\Omega)$	$Z_m(\Omega)$	$C_x(nF)$	$C_y(nF)$	$I_3(\mu A)$	$V(mV)$
20	20	20	20	270.022	230.73	19.519	0	0	1000	19.519
20	**20**	**20**	**20**	**270.022**	**230.73**	**19.519**	**5**	**5**	**508.677**	**13.054**
20	20	50	20	270.022	230.73	19.519	5	5	500.744	23.136
20	20	50	50	270.022	230.73	19.519	5	5	491.901	12.962
20	20	20	20	270.022	230.73	19.519	2	2	828.057	17.085
50	20	20	20	270.022	230.73	19.519	5	5	508.677	13.054
20	50	20	20	270.022	230.73	19.519	5	5	468.925	12.619

6.3.1.2 Image reconstruction under the effect of leakage current

In this section, the coupling capacitances were set to $C_x = C_y = 5nF$, and four boundary voltage sets were collected: V_{m-1} and V_{m-2} were corresponding to the heterogeneous model (Figure 6-3 (c)) while V_{r-1} and V_{r-2} were corresponding to the homogeneous model (Figure 6-3 (b)) at f_1 and f_2 , respectively. A 50 dB Gaussian noise was added to each voltage set to simulate the measurement noise during practical experiments [157]. The calibration of FDEIT measurements was performed with the conventional FDEIT method and the proposed CFDEIT.

As can be seen in Figure 6-5 (a), the boundary voltage measurements change with the frequency in both the homogeneous sensor model and the heterogeneous model with the scaffold sample. Since the background conductivity is frequency independent, these variations should be blamed for the leakage current, which changes the voltage drops on the contact impedance and the target impedance. In the homogeneous model, the voltage variation on the electrode pairs near the current stimulation is around 5.4 *mV*. However, this value only increases to 7 *mV* when the scaffold sample is placed near the electrodes. Therefore, the voltage variation induced by the conductivity change of the tissue sample may be overwhelmed by the errors induced by the leakage current.

Figure 6-5 (b) shows there is a significant variation between the raw voltages at f_1 and f_2 . This voltage variation cannot be used in the image reconstruction directly as it emphasises the modelling errors in the image reconstruction. In FDEIT, the optimal weight factor minimises the voltage variation by compensating the in-phase term between V_{m-1} and V_{m-2} [122]. This method eliminates most of the errors introduced by the leakage current, but it also reduces the variation introduced by the conductivity change of the tissue

sample and the voltage variation near the scaffold sample is less than 0.4 *mV* after calibration. As a consequence, it may easily be affected by the noise and the errors introduced by the leakage current. The proposed CFDEIT maintains the 1.52 *mV* voltage variation near the tissue sample while compensating the errors in the measurements through subtraction. This value is similar to the voltage variation introduced by the scaffold sample in Figure 6-5 (a). Hence, the boundary voltages maintain small changes in the background area and the changes introduced by the scaffold sample are highlighted.

The images reconstructed for the sensor model with the scaffold sample are shown in Figure 6-6. In Figure 6-6 (a), not only the scaffold sample at position (10.8, 7.2) but also an unexpected anomaly appears in the image with FDEIT. The unexpected anomaly locates at position (5.7, 12), and its conductivity variation is similar to the scaffold sample. One reason for the unexpected anomaly is the inapplicability of the four-electrode reciprocity theorem [15] when leakage current exists. Due to the leakage current, the interchange of injection and measurement pairs are two independent measurements. Hence, omitting the interchanged measurement causes errors in the image unless the effect of leakage current can be compensated. In Figure 6-6 (b), the image with CFDEIT has a clear background and the scaffold sample is reconstructed at position (11.4, 7.5) with a sharp boundary. This position is close to the true position of the scaffold sample, and the CC of Figure 6-6 (b) is also smaller than that of Figure 6-6 (a). Hence, CFDEIT provides a better image quality regarding tracking the position of the tissue sample and monitor its conductivity variation.

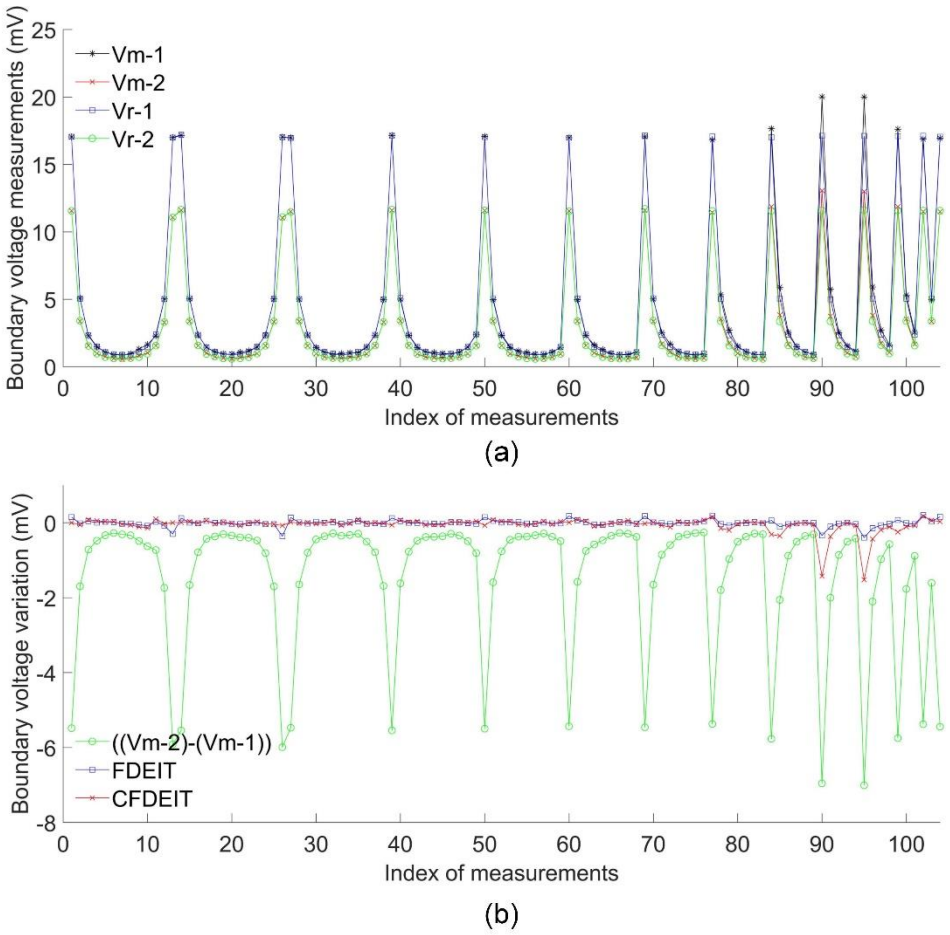

Figure 6-5 Boundary voltages corresponding to the miniature EIT sensor models

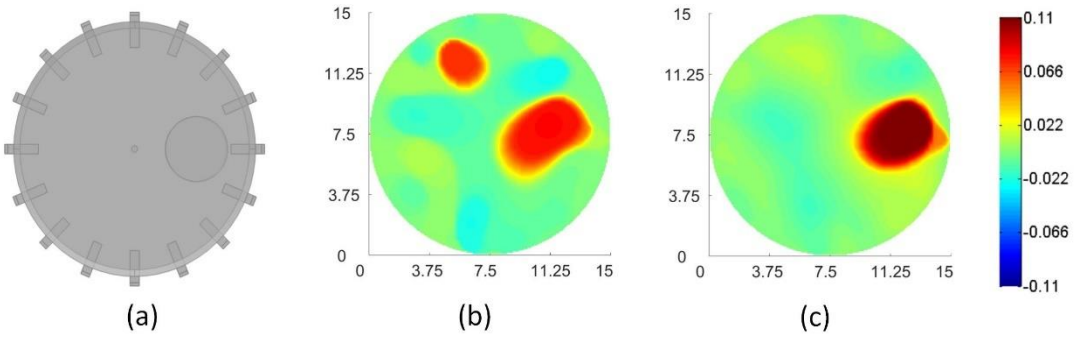

Figure 6-6 The true image of the model and the reconstructed images with (b) FDEIT and (c) CFDEIT

Table 6-2 Correlation coefficients of the reconstructed images in simulations

Methods	FDEIT	CFDEIT
CC	0.6494	0.8781

6.3.2 Experimental results

6.3.2.1Boundary voltage evaluation

Figure 6-7 illustrates the boundary voltages for hydrogel sample and scaffold sample as well as their blank controls. In both cases, the boundary voltages change with the frequency. The differences between the samples and their blank controls are not apparent, which are much smaller than the voltage variation between two frequencies.

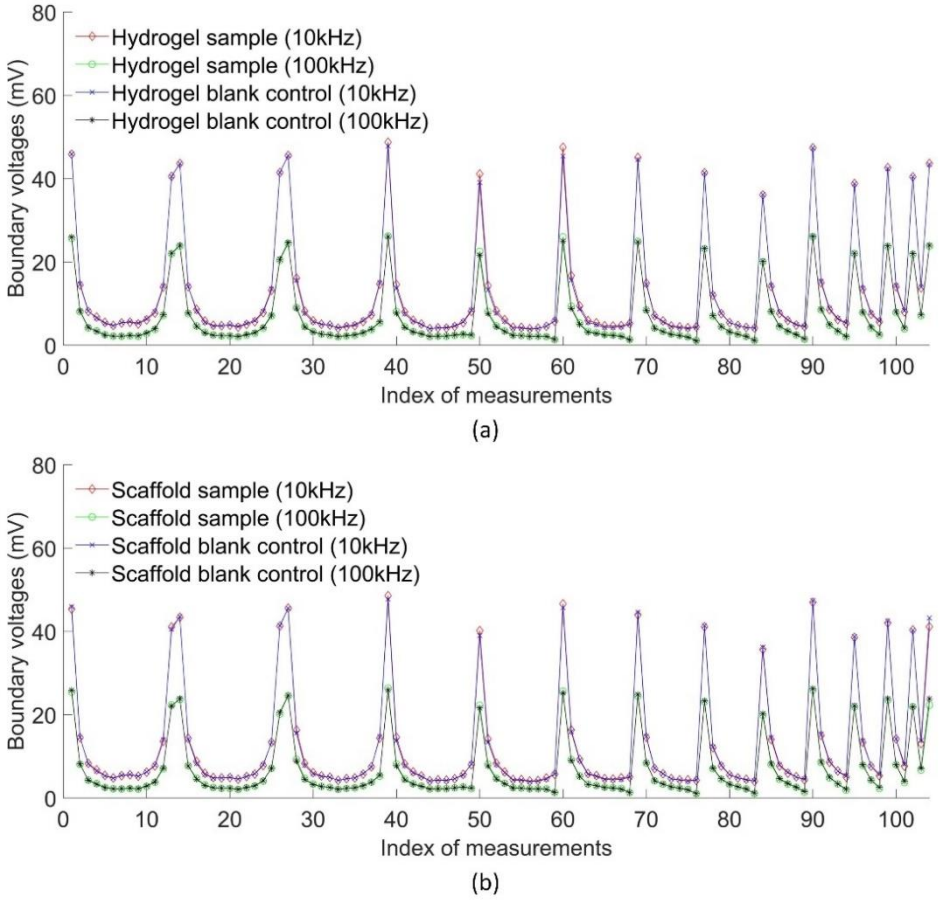

Figure 6-7 Boundary voltages for (a) hydrogel sample and its blank control and (b) scaffold sample and its blank control

6.3.2.2Image reconstruction with accurate reference

The boundary voltage variations processed by FDEIT and CFDEIT are shown in Figure 6-8. The sensor with culture medium was used as the reference for the calibration of FDEIT. It can be seen that the boundary voltage variations processed with FDEIT have a more significant fluctuation than those processed with CFDEIT. Compared with the control groups, the voltage variations for the hydrogel sample and the scaffold sample have an obvious drop when processed with CFDEIT. However, it is hard to distinguish the control groups and the sample groups using FDEIT. Using CFDEIT, the nadir of the voltage variations occurs at the 50^{th} measurements where the current was injected from electrode pair 5-6 and voltage was measured from electrode pair 7-8. However, the valleys of the voltage variations with FDEIT occur when an unexpected voltage drops exist in the boundary voltages, which can be observed in Figure 6-7.

Figure 6-9 and Figure 6-10 show the images for hydrogel sample, scaffold sample and their blank controls. In the image reconstructed with FDEIT, only an unexpected anomaly is reconstructed on the top of the images and noise occurs around position (6.2, 11.2). There is no obvious difference between these images, so FDEIT fails to distinguish the sample from the blank control for both the hydrogel and the scaffold. In Figure 6-9 (c) and Figure 6-10 (c), the conductivity distribution increases in the circles located at position (6, 4) and position (6.3, 4.2), respectively. They are the same as the true position of the hydrogel sample and the scaffold sample, and it consists of the fact that the viable cells have a higher conductivity when frequency increases. Figure 6-9 (f) and Figure 6-10 (f) indicate that the conductivity of the hydrogel blank control is slightly lower than that of the culture medium and the conductivity of the blank scaffold control has the same conductivity with the culture medium. Both of them show a distinct difference from the images for the samples, therefore, CFDEIT can be used to monitor the cell growth and cell viability in the 3D bioscaffolds based on the conductivity variation.

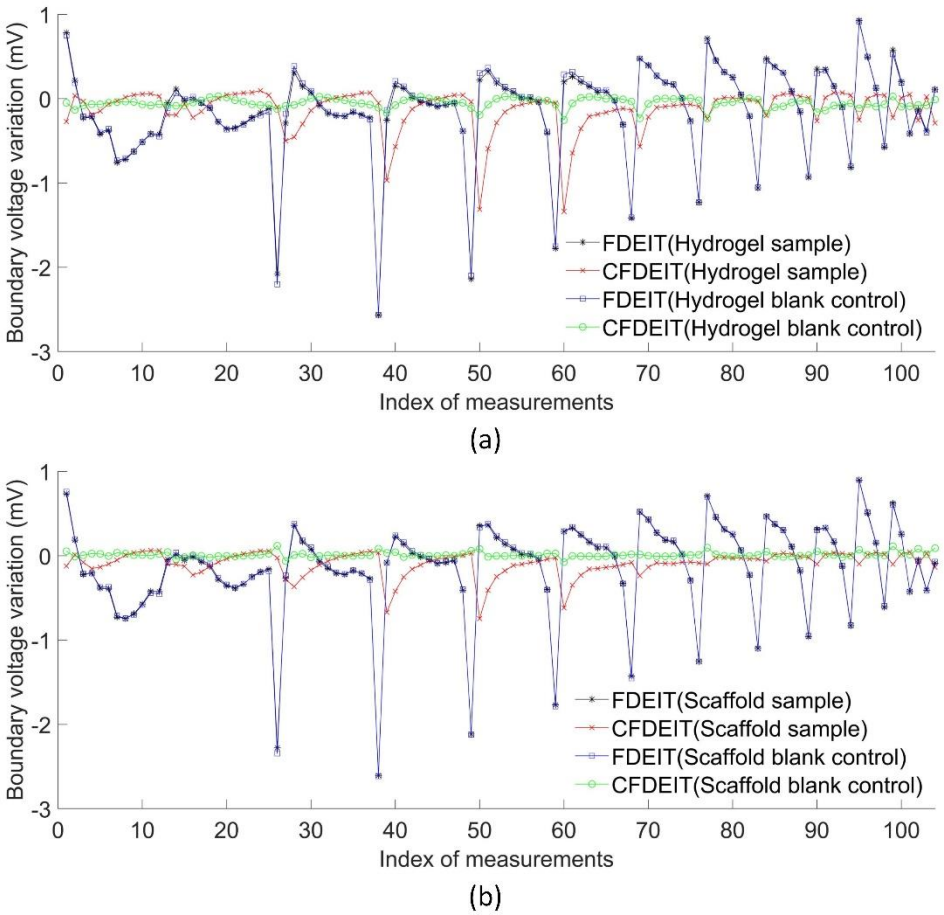

Figure 6-8 Boundary voltage variations for (a) hydrogel sample and (b) scaffold sample

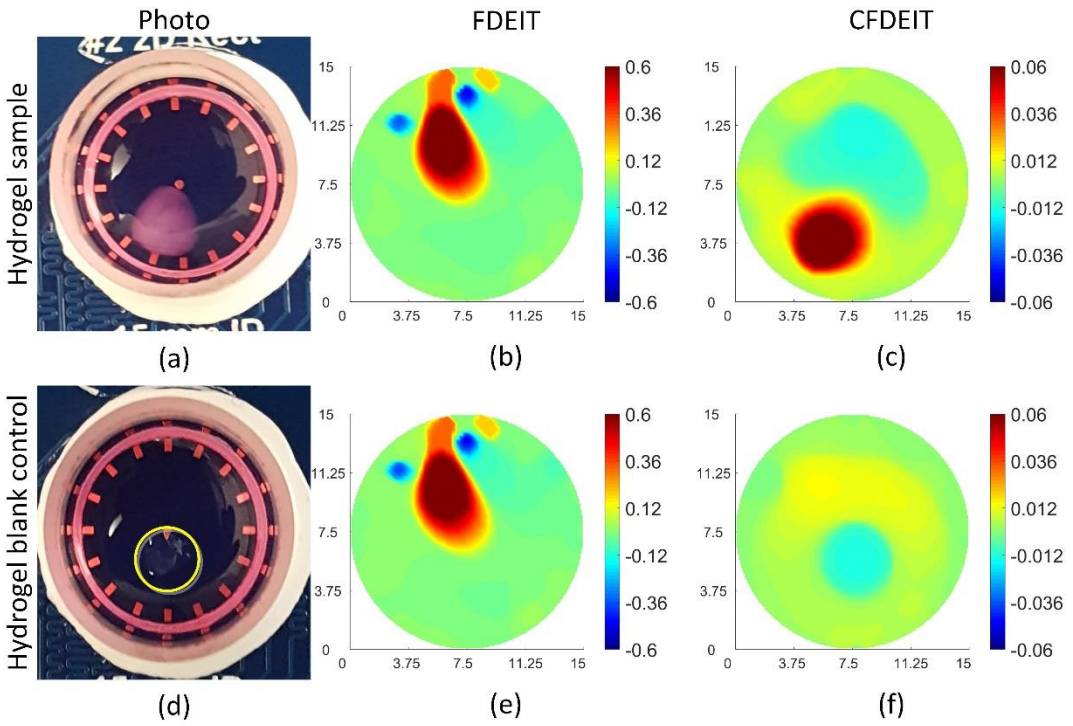

Figure 6-9 The true image and the reconstructed images for the hydrogel sample

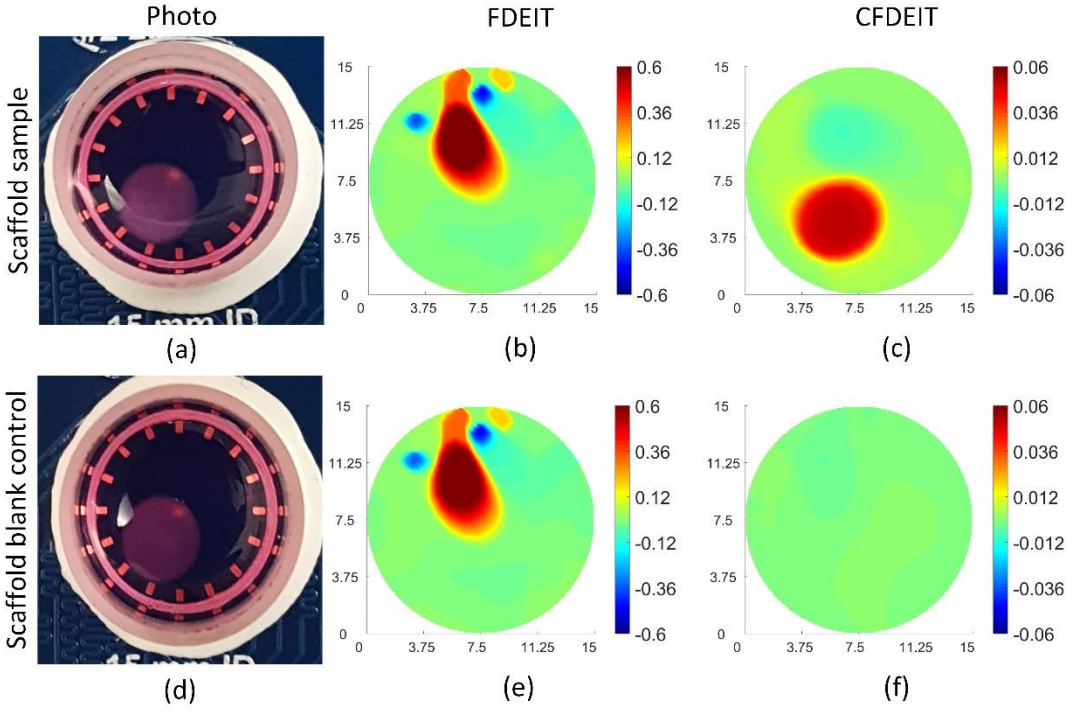

Figure 6-10 The true image and the reconstructed images for the scaffold sample

6.3.2.3Image reconstruction with inaccurate reference

The conductivity of the culture medium may change during the cell culture due to cell activities. Therefore, in practical cases, the background reference with an accurate conductivity is not always available. In order to evaluate the robustness of FDEIT to the background changes, the reference for FDEIT calibration was replaced by the boundary voltages taken from PBS, which has a different conductivity with the culture medium. Image reconstruction with and without normalisation was compared.

Figure 6-11 shows the images reconstructed with inaccurate reference (PBS). The centres of the hydrogel sample and the scaffold sample are position (6, 5.55) and position (6, 6.2), respectively, which have been shifted towards the middle of the sensor due to modelling errors. Compared with the images reconstructed with an accurate reference (culture medium) in Figure 6-9 and Figure 6-10, the images with an inaccurate reference has a slightly lower CC value as well. However, the drop of CC is mainly caused by the shift of the sample and the background noise, so the image in Figure 6-11 still correctly reflect the true conductivity changes of the sample and maintain their clear boundaries. As a consequence, CFDEIT is robust to the background conductivity change during the cell culture.

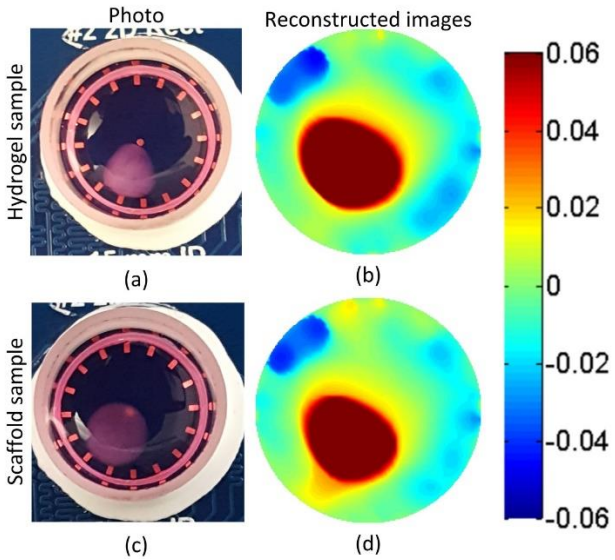

Figure 6-11 Image reconstruction for tissue samples with inaccurate reference

Table 6-3 Correlation coefficients of the reconstructed images in experiments

	With accurate reference	With inaccurate reference
Hydrogel sample	0.8655	0.6751
Scaffold sample	0.8930	0.7207

6.4 Discussions

The equivalent circuit analysis demonstrates the measurement errors in FDEIT are mainly contributed by the presence of coupling capacitance. Leakage current is diverted through the coupling capacitance, resulting in the decrease of current going through the target impedance and the voltage drops on the contact impedances. Therefore, the measured target impedance is usually lower than that of the true value, and it is also affected by the contact impedances if the contact impedances between two measuring electrodes are not identical.

Conventional FDEIT is widely used in macro EIT imaging to extract the anomaly from the background [123, 176, 177], but its performance for miniature tissue culture monitoring is poor. Due to the presence of coupling capacitances, the boundary voltages related to not only the target impedance but also the leakage current, contact impedance and edge impedance. The weight factor in FDEIT eliminated the projection terms in these errors, but it failed to reduce the orthogonal terms, which were assumed to contain the core information [122]. In miniature EIT imaging where voltage variations introduced by the samples were lower than the measurement errors, the calculation of the weight factor was mainly affected by the errors. Hence, the unexpected anomaly occurred between electrode 16-1 in the reconstructed images.

Based on the equivalent circuit, the CFDEIT method has been developed to compensates the measurement errors in miniature EIT imaging. By subtracting the error terms, the boundary voltages maintained the same value if conductivity distribution wasn't changed in the sensing area. In order to evaluate the performance of this method, a joint simulation method to perform error analysis in EIT measurements has been developed using COMSOL Multiphysics and LTspice. It proves that the change of boundary voltage corresponding to the variation of each component is the same as that demonstrated in the equation for CFDEIT (6-8). In both the simulations and the experiments, the centres of the bioscaffolds can be correctly demonstrated in the reconstructed images with the position error of 0.1 *mm*. It is also feasible to differentiate the samples with cells from their blank controls.

When the conductivity of the background solution is not available, PBS can be used as the reference for CFDEIT. Although the image qualities are reduced by 17%-19% in terms of CC, the conductivity variations of the bioscaffolds, which are related to the cell characteristics, are similar to those in the images reconstructed with accurate reference. Therefore, CFDEIT can demonstrate the cell characteristics without accurate references, and it is suitable for long-term cell culture monitoring where the conductivity of culture medium changes over time.

Cells in suspensions or sparse adherent culture have a different dielectric cell response than in a tissue-like structure as interconnected cells oppose an intercellular resistance to the electrical field in addition to their individual dielectric properties. By applying the effective medium theory [157], the conductivity variation of the bioscaffolds not only indicates the cell concentration but also other cellular activities, such as cell differentiation, in future studies.

6.5 Summary

In this study, the errors in FDEIT measurements have been analysed through equivalent circuit analysis. A joint simulation combining FEM EIT modelling

and SPICE circuit simulation has been developed to evaluate the effect of each component to the boundary voltage. Based on the equivalent circuit, the CFDEIT method has been developed to eliminate measurement errors. The following conclusions can be drawn from the numerical simulations and experimental results:

- Measurement errors in miniature FDEIT are mainly introduced by the leakage current through coupling capacitances to the ground.
- In 3D tissue culture experiments, the measurement error between 10 *kHz* and 100 *kHz* is 20.3 *mV*, which is 19.6 *mV* larger than the voltage variations introduced by the presence of cells in the bioscaffolds.
- CFDEIT can eliminate the measurement errors and increase the image quality by 23% in terms of the correlation coefficient. It penalises the background noises and unexpected anomaly in the images while maintaining the information of the bioscaffolds. It also helps to distinguish the samples from their blank controls.
- It demonstrates that CFDEIT can work with an inaccurate reference, so it is suitable for long-term tissue culture monitoring where the conductivity of the culture medium is time-dependent.

To the best of my knowledge, this is the first study to evaluate the effect of leakage current in biological FDEIT imaging and to monitor 3D tissue culture using FDEIT. It provides a new tool for long-term tissue culture monitoring with the advantages of high temporal resolution, label-free, non-toxic and non-destructive.

Chapter 7 Conclusions and future work

The focus of this thesis was on the development of methods and theoretical foundation for the application of EIT on 3D tissue culture monitoring. The protocols of EIT to monitor the 3D cell culture in tightly packed spheroids, hydrogels and bioscaffolds with sparse cell distribution had been developed. A 3D tissue model was developed based on the single shell theory to demonstrate the relationship between the cell concentration, cell viability and the conductivity of the entire tissue. The limitation and resolution of EIT for cellular assays were therefore calculated through the model and examined by numerical simulations and biological experiments. As one of the most important factors affecting the accuracy of the EIT image, the measurement errors were analysed by developing a joint simulation method using Multiphysics software and circuit simulation software. A calibration method was then derived to eliminate the measurement errors in 3D tissue culture monitoring.

7.1 Summary of findings

In Chapter 3 , a feasibility study to investigate the potential of miniature EIT for 3D biological tissue monitoring was presented. Both TDEIT and FDEIT were tested in the miniature EIT sensor with plant tissue samples. The results were then evaluated by the true conductivity spectra measured on the samples directly. It showed the potential of EIT to semi-quantitatively assess the conductivity of tissues cultured in the sensor, which were surrounded by conductive background solution. The optimal settings for miniature EIT in 3D biological tissue monitoring and the protocols to avoid artificial measurement errors were concluded by considering the results and the performance of the Agile Tomography system. An improvement was also made to the sub-domain-based regularisation algorithm to evaluate the effect of image reconstruction algorithms to the quality of the reconstructed images. This chapter acted as the foundation of the thesis for designing the numerical simulations and biological experiments in miniature scale.

In Chapter 4 , a method was proposed for the real-time monitoring of cell spheroid drug response using time-difference EIT. A 3D tissue model based on single shell theory was developed for calculating its conductivity from the cell concentration, cell viability and electrical properties of the cells. The theoretical resolution of EIT for cellular imaging was then estimated through this model. In the experiment, an improved liquid overlay method was developed to form viable tumour spheroids in the miniature EIT sensor with updated coating and culture medium. The first study to monitor the conductivity variation of 3D cell spheroids following a chemical insult using EIT was performed with the time-difference imaging. It was shown that my method could reconstruct the small conductivity variation due to the change of cell viability in a temporal resolution over 3.3 fps in real-time. It quantitatively estimated the conductivity change in real-time, providing more detailed information for the transient changes in cell viability within large 3D spheroids.

In Chapter 5 , the real-time monitoring method was extended for the applications of tissue engineering, where cells were sparsely distributed in 3D bioscaffolds. The performance of time-difference imaging and frequency-difference imaging were compared. The results showed the conductivity variation of cells in the bioscaffolds were easier affected by unexpected disturbances than those of the plant tissues and spheroids where cells were connected tightly. The time-difference method had higher image quality in static imaging, but it was difficult to separate the conductivity variation due to cell death and that introduced by the culture medium. Frequency-difference imaging can be utilised to solve this problem, but a proper calibration method should be developed to reduce the measurement errors introduced by the impedance measurement system.

In Chapter 6 , an equivalent circuit model was developed for the single-channel measurement of EIT to demonstrate the measurement errors contributed by each component in the circuitry. A calibration method for FDEIT was derived based on the model to eliminate the circuitry errors, and its robustness to background disturbance was improved by the implementation of normalisation.

A novel simulation method combining Multiphysics simulation and analogue circuit simulation was then developed to evaluate the performance of the calibration method, and it could be extended for other EIT applications to analyse the effect of circuitry errors to the boundary voltage measurements. The results showed that the CFDEIT method significantly improved the image quality of frequency-difference images, and it successfully solved the problem demonstrated in Chapter 5 It extended the application of FDEIT for long-term tissue culture monitoring by improving the robustness of FDEIT to the disturbance of background conductivity.

7.2 Future work

This thesis made a step forward in the development of EIT for 3D tissue culture monitoring. It came up with new protocols and new models to monitor the in-vitro 3D tissue samples, but some limitations occurred in the analysis of the data, which should be resolved in future studies:

7.2.1 Validation of EIT data

Technology validation confirms that EIT can reconstruct the cell viability correctly and it can be further incorporated into the existing biological monitoring system to provide extra information for the researches. In this thesis, the EIT images of the tissue viability were validated by the cellular metabolic viability assays at the endpoint of the experiment. However, the accuracy of the images during the chemical insult still needed to be determined by other measuring techniques due to the low temporal resolution of the metabolic assays. EIS measurement may be used for the validation when the spheroids are cultured in a system with background calibration [8]. Alternatively, dual-modality imaging combining EIT and optical-based imaging can be carried out on a transparent EIT sensor (Figure 3-2).

7.2.2 Sensor design and modelling

The simulations and experiments in this thesis were based on the planar miniature EIT sensor with 16 working electrodes on its substrate. Although this design provided a good horizontal resolution of the tissue samples located on

the bottom of the sensor and avoided the impedance artefacts due to the contact between the sample and the electrode surface, it had a limited vertical resolution in 3D image reconstruction [178]. As a consequence, the tissue sample reconstructed in 3D suffered from severe deformation and displacement when modelling errors existed, which may be introduced by the change of liquid surface or liquid volume. In order to reduce the errors and the computational cost, my studies were based on the sensitivity matrix for the bottom layer of the sensor, which aimed to better demonstrate the horizontal position and cellular activities of the samples in a 2D plane. Further studies should be carried out to optimise the sensor structure and the location of electrodes; so that the conductivity variation within each voxel can be correctly reconstructed.

7.2.3 Image reconstruction using spatiotemporal information

Conventional algorithms utilise the spatial regularisation to stabilise the cost function when solving the inverse problem. These approaches constrain the conductivity to the desired distribution, but the images reconstructed for different time points are independent. Hence, the random noises during the measurement will cause unexpected disturbances in the reconstructed conductivity of the tissue sample, which increases the difficulty in the sample analysis. Considered the continuity of the conductivity in time domain, the spatiotemporal regularisation methods [109, 179] could be applied in the future study to visualise the dynamic change of tissue conductivity with improved accuracy.

7.2.4 Wideband spectro-tomography

In single-frequency TDEIT or dual-frequency FDEIT, the images can only demonstrate limited features of the tissue samples. For example, the measuring frequencies in this thesis locate at β-dispersion, where the conductivity of the cells is mainly affected by the interfacial polarisation across the cell membranes. The results, therefore, reflected the corresponding features, such as cell concentration and cell viability. To analyse the interaction

between adjacent cells and the features of cytoplasm and cell nucleus, the information on other frequencies are required.

It has previously been proposed in the literature to use the wideband signal as the stimulating current so that the conductivity spectra of the tissue sample can be measured simultaneously [180]. The idea is to generate a chirp signal that sweeps the desired frequency range from the current source, and the boundary voltages corresponding to each frequency is resolved through wavelet analysis before image reconstruction. The reconstructed images can be further utilised to develop the dielectric relaxation model for the tissue samples [181], which also provides the electrical characteristics of the tissue samples out of the measuring frequency range.

Reference

[1] F. Pampaloni, E. G. Reynaud, and E. H. Stelzer, "The third dimension bridges the gap between cell culture and live tissue," *Nature reviews Molecular cell biology,* vol. 8, no. 10, p. 839, 2007.

[2] K. Bardsley, A. J. Deegan, A. El Haj, and Y. Yang, "Current State-of-the-Art 3D Tissue Models and Their Compatibility with Live Cell Imaging," in *Multi-Parametric Live Cell Microscopy of 3D Tissue Models*: Springer, 2017, pp. 3-18.

[3] T. Xu *et al.*, "7 - Bioprinting for constructing microvascular systems for organs," in *Rapid Prototyping of Biomaterials*, R. Narayan, Ed.: Woodhead Publishing, 2014, pp. 201-220.

[4] N. J. Martucci *et al.*, "Nondestructive Optical Toxicity Assays of 3D Liver Spheroids with Optical Coherence Tomography," *Advanced Biosystems,* vol. 2, no. 3, p. 1700212, 2018.

[5] L. E. Smith, R. Smallwood, and S. Macneil, "A comparison of imaging methodologies for 3D tissue engineering," *Microscopy research and technique,* vol. 73, no. 12, pp. 1123-1133, 2010.

[6] F. A. Alexander, D. T. Price, and S. Bhansali, "From cellular cultures to cellular spheroids: is impedance spectroscopy a viable tool for monitoring multicellular spheroid (MCS) drug models?," *IEEE reviews in biomedical engineering,* vol. 6, pp. 63-76, 2013.

[7] W. Gamal, H. Wu, I. Underwood, J. Jia, S. Smith, and P. Bagnaninchi, "Impedance-based cellular assays for regenerative medicine," *Phil. Trans. R. Soc. B,* vol. 373, no. 1750, p. 20170226, 2018.

[8] P. M. Misun, J. Rothe, Y. R. Schmid, A. Hierlemann, and O. Frey, "Multi-analyte biosensor interface for real-time monitoring of 3D microtissue spheroids in hanging-drop networks," *Microsystems & Nanoengineering,* vol. 2, p. 16022, 2016.

[9] J. Daoud, K. Heileman, S. Shapka, L. Rosenberg, and M. Tabrizian, "Dielectric spectroscopy for monitoring human pancreatic islet differentiation within cell-seeded scaffolds in a perfusion bioreactor system," *Analyst,* vol. 140, no. 18, pp. 6295-6305, 2015.

[10] K. F. Lei, M.-H. Wu, C.-W. Hsu, and Y.-D. Chen, "Real-time and non-invasive impedimetric monitoring of cell proliferation and chemosensitivity in a perfusion 3D cell culture microfluidic chip," *Biosensors and Bioelectronics,* vol. 51, no. Supplement C, pp. 16-21, 2014/01/15/ 2014.

[11] J. Yun *et al.*, "Electrical impedance spectroscopy for biotissue differentiation using bipolar electrodes positioned at the end of a hypodermic needle," in *2015 Transducers-2015 18th International Conference on Solid-State Sensors, Actuators and Microsystems (TRANSDUCERS)*, 2015, pp. 1533-1536: IEEE.

[12] R. P. Henderson and J. G. Webster, "An impedance camera for spatially specific measurements of the thorax," *IEEE Transactions on Biomedical Engineering*, no. 3, pp. 250-254, 1978.

[13] D. S. Holder, *Electrical impedance tomography: methods, history and applications*. CRC Press, 2004.

[14] B. H. Brown, "Electrical impedance tomography (EIT): a review," *J Med Eng Technol*, vol. 27, no. 3, pp. 97-108, May-Jun 2003.

[15] R. Harikumar, R. Prabu, and S. Raghavan, "Electrical Impedance Tomography (EIT) and Its Medical Applications: A Review," *International Journal of Soft Computing Engineering*, vol. 3, no. 4, pp. 2231-2307, 2013.

[16] T. Hiraga, S. Nebuya, and M. Ujihira, "Basic study on visualization of a cell during freezing using electrical impedance tomography," *Transactions of Japanese Society for Medical and Biological Engineering*, vol. 51, no. Supplement, pp. R-253-R-253, 2013.

[17] T. Sun, S. Tsuda, K.-P. Zauner, and H. Morgan, "On-chip electrical impedance tomography for imaging biological cells," *Biosensors and Bioelectronics*, vol. 25, no. 5, pp. 1109-1115, 2010.

[18] H. Fricke and S. J. T. J. o. g. p. Morse, "The electric resistance and capacity of blood for frequencies between 800 and 4½ million cycles," vol. 9, no. 2, p. 153, 1925.

[19] K. Asami, "Characterization of biological cells by dielectric spectroscopy," *Journal of Non-Crystalline Solids*, vol. 305, no. 1, pp. 268-277, 2002/07/01/ 2002.

[20] C. Prodan, F. Mayo, J. Claycomb, J. Miller Jr, and M. Benedik, "Low-frequency, low-field dielectric spectroscopy of living cell suspensions," *Journal of applied physics*, vol. 95, no. 7, pp. 3754-3756, 2004.

[21] R. D. Stoy, K. R. Foster, H. P. J. P. i. M. Schwan, and Biology, "Dielectric properties of mammalian tissues from 0.1 to 100 MHz; a summary of recent data," vol. 27, no. 4, p. 501, 1982.

[22] Y. Xu, X. Xie, Y. Duan, L. Wang, Z. Cheng, and J. Cheng, "A review of impedance measurements of whole cells," *Biosensors and Bioelectronics*, vol. 77, pp. 824-836, 2016/03/15/ 2016.

[23] Z. Jiang *et al.*, "Development of a Portable Electrochemical Impedance Spectroscopy System for Bio-Detection," *IEEE Sensors Journal*, vol. 19, no. 15, pp. 5979-5987, 2019.

[24] K. Heileman, J. Daoud, and M. Tabrizian, "Dielectric spectroscopy as a viable biosensing tool for cell and tissue characterization and analysis," *Biosensors and Bioelectronics*, vol. 49, pp. 348-359, 2013.

[25] H. Schwan, "Electrical properties of tissues and cell suspensions: mechanisms and models," in *Engineering in Medicine and Biology Society, 1994. Engineering Advances: New Opportunities for Biomedical Engineers.*

Proceedings of the 16th Annual International Conference of the IEEE, 1994, vol. 1, pp. A70-A71 vol. 1: IEEE.

[26] T. J. K.-Z. Hanai, "Theory of the dielectric dispersion due to the interfacial polarization and its application to emulsions," journal article vol. 171, no. 1, pp. 23-31, July 01 1960.

[27] P. K. Kauppinen, J. A. Hyttinen, T. Kööbi, and J. Malmivuo, "Lead field theoretical approach in bioimpedance measurements: towards more controlled measurement sensitivity," *Ann N Y Acad Sci*, vol. 873, 1999.

[28] M. Böttrich, J. M. A. Tanskanen, and J. A. K. Hyttinen, "Lead field theory provides a powerful tool for designing microelectrode array impedance measurements for biological cell detection and observation," *BioMedical Engineering OnLine*, journal article vol. 16, no. 1, p. 85, June 26 2017.

[29] R. Bragos *et al.*, "Four versus two-electrode measurement strategies for cell growing and differentiation monitoring using electrical impedance spectroscopy," in *Engineering in Medicine and Biology Society, 2006. EMBS'06. 28th Annual International Conference of the IEEE*, 2006, pp. 2106-2109: IEEE.

[30] R. Szulcek, H. J. Bogaard, and G. P. van Nieuw Amerongen, "Electric cell-substrate impedance sensing for the quantification of endothelial proliferation, barrier function, and motility," *JoVE (Journal of Visualized Experiments)*, no. 85, pp. e51300-e51300, 2014.

[31] R. Pradhan, M. Mandal, A. Mitra, and S. Das, "Monitoring cellular activities of cancer cells using impedance sensing devices," *Sensors and Actuators B: Chemical*, vol. 193, pp. 478-483, 2014.

[32] P. O. Bagnaninchi and N. Drummond, "Real-time label-free monitoring of adipose-derived stem cell differentiation with electric cell-substrate impedance sensing," *Proceedings of the National Academy of Sciences*, vol. 108, no. 16, pp. 6462-6467, 2011.

[33] I. Miccoli, F. Edler, H. Pfnür, and C. J. J. o. P. C. M. Tegenkamp, "The 100th anniversary of the four-point probe technique: the role of probe geometries in isotropic and anisotropic systems," vol. 27, no. 22, p. 223201, 2015.

[34] F. J. J. o. t. W. A. o. S. Wenner, "A method for measuring earth resistivity," vol. 5, no. 16, pp. 561-563, 1915.

[35] H. Chandra, S. Allen, S. Oberloier, N. Bihari, J. Gwamuri, and J. J. M. Pearce, "Open-source automated mapping four-point probe," vol. 10, no. 2, p. 110, 2017.

[36] S. Yoshimoto *et al.*, "Four-point probe resistance measurements using PtIr-coated carbon nanotube tips," vol. 7, no. 4, pp. 956-959, 2007.

[37] L. B. J. P. o. t. I. Valdes, "Resistivity measurements on germanium for transistors," vol. 42, no. 2, pp. 420-427, 1954.

[38] A. McEwan, G. Cusick, and D. J. P. m. Holder, "A review of errors in multi-frequency EIT instrumentation," vol. 28, no. 7, p. S197, 2007.

[39] E. Sarro *et al.*, "Electrical impedance spectroscopy measurements using a four-electrode configuration improve on-line monitoring of cell concentration in adherent animal cell cultures," *Biosensors and Bioelectronics,* vol. 31, no. 1, pp. 257-263, 2012.

[40] C. Canali *et al.*, "An impedance method for spatial sensing of 3D cell constructs–towards applications in tissue engineering," *Analyst,* vol. 140, no. 17, pp. 6079-6088, 2015.

[41] X. Liu, J. Yao, T. Zhao, H. Obara, Y. Cui, and M. Takei, "Image Reconstruction Under Contact Impedance Effect in Micro Electrical Impedance Tomography Sensors," *IEEE transactions on biomedical circuits and systems,* 2018.

[42] S. Behkami, J. Frounchi, F. G. Pakdel, and T. Stieglitz, "Simulation of effects of the electrode structure and material in the density measuring system of the peripheral nerve based on micro-electrical impedance tomography," *Biomedical Engineering/Biomedizinische Technik,* vol. 63, no. 2, pp. 151-161, 2018.

[43] K. S. Cole and H. J. J. T. J. o. g. p. Curtis, "Electric impedance of single marine eggs," vol. 21, no. 5, pp. 591-599, 1938.

[44] K. S. Cole and R. M. J. T. J. o. g. p. Guttman, "Electric impedance of the frog egg," vol. 25, no. 5, pp. 765-775, 1942.

[45] H. P. Schwan, "Electrical properties of tissue and cell suspensions," in *Advances in biological and medical physics*, vol. 5: Elsevier, 1957, pp. 147-209.

[46] K. Asami, "Characterization of heterogeneous systems by dielectric spectroscopy," *Progress in Polymer Science,* vol. 27, no. 8, pp. 1617-1659, 2002/10/01/ 2002.

[47] J. E. Yardley, D. B. Kell, J. Barrett, and C. L. Davey, "On-line, real-time measurements of cellular biomass using dielectric spectroscopy," (in eng), *Biotechnology & genetic engineering reviews,* vol. 17, pp. 3-35, 2000 2000.

[48] P. Ducommun, A. Kadouri, U. Von Stockar, and I. Marison, "On‐line determination of animal cell concentration in two industrial high‐density culture processes by dielectric spectroscopy," *Biotechnology and bioengineering,* vol. 77, no. 3, pp. 316-323, 2002.

[49] J. P. Carvell and J. E. Dowd, "On-line measurements and control of viable cell density in cell culture manufacturing processes using radio-frequency impedance," *Cytotechnology,* vol. 50, no. 1-3, pp. 35-48, 2006.

[50] D. Holmes *et al.*, "Leukocyte analysis and differentiation using high speed microfluidic single cell impedance cytometry," vol. 9, no. 20, pp. 2881-2889, 2009.

[51] H. Morgan, T. Sun, D. Holmes, S. Gawad, and N. G. J. J. o. P. D. A. P. Green, "Single cell dielectric spectroscopy," vol. 40, no. 1, p. 61, 2006.

[52] D. Kloß, M. Fischer, A. Rothermel, J. C. Simon, and A. A. Robitzki, "Drug testing on 3D in vitro tissues trapped on a microcavity chip," *Lab on a Chip*, vol. 8, no. 6, pp. 879-884, 2008.

[53] D. Kloß *et al.*, "Microcavity array (MCA)-based biosensor chip for functional drug screening of 3D tissue models," *Biosensors and Bioelectronics*, vol. 23, no. 10, pp. 1473-1480, 2008.

[54] I. Giaever and C. R. J. P. o. t. N. A. o. S. Keese, "Monitoring fibroblast behavior in tissue culture with an applied electric field," vol. 81, no. 12, pp. 3761-3764, 1984.

[55] C. Tiruppathi, A. B. Malik, P. J. Del Vecchio, C. R. Keese, and I. J. P. o. t. N. A. o. S. Giaever, "Electrical method for detection of endothelial cell shape change in real time: assessment of endothelial barrier function," vol. 89, no. 17, pp. 7919-7923, 1992.

[56] C. R. Keese, I. J. I. E. i. M. Giaever, and B. Magazine, "A biosensor that monitors cell morphology with electrical fields," vol. 13, no. 3, pp. 402-408, 1994.

[57] J. Wegener, J. J. C. Seebach, and t. research, "Experimental tools to monitor the dynamics of endothelial barrier function: a survey of in vitro approaches," vol. 355, no. 3, pp. 485-514, 2014.

[58] C.-M. Lo, C. R. Keese, and I. J. B. j. Giaever, "Impedance analysis of MDCK cells measured by electric cell-substrate impedance sensing," vol. 69, no. 6, pp. 2800-2807, 1995.

[59] Y. Zhang, L. Wang, J. Zhu, Y. Hu, W. Xing, and J. J. B. l. Cheng, "Real-time monitoring of extracellular matrix-mediated PC12 cell attachment and proliferation using an electronic biosensing device," vol. 34, no. 2, pp. 397-404, 2012.

[60] A. Rahman, J. Register, G. Vuppala, and S. Bhansali, "Cell culture monitoring by impedance mapping using a multielectrode scanning impedance spectroscopy system (CellMap)," *Physiological measurement*, vol. 29, no. 6, p. S227, 2008.

[61] D. C. Lovelady, J. Friedman, S. Patel, D. A. Rabson, C.-M. J. B. Lo, and Bioelectronics, "Detecting effects of low levels of cytochalasin B in 3T3 fibroblast cultures by analysis of electrical noise obtained from cellular micromotion," vol. 24, no. 7, pp. 2250-2254, 2009.

[62] F. Atienzar, H. Gerets, K. Tilmant, G. Toussaint, and S. J. B. Dhalluin, "Evaluation of impedance-based label-free technology as a tool for pharmacology and toxicology investigations," vol. 3, no. 1, pp. 132-156, 2013.

[63] D. Opp *et al.*, "Use of electric cell–substrate impedance sensing to assess in vitro cytotoxicity," vol. 24, no. 8, pp. 2625-2629, 2009.

[64] W. Gamal *et al.*, "Real-time quantitative monitoring of hiPSC-based model of macular degeneration on Electric Cell-substrate Impedance Sensing

microelectrodes," *Biosensors and Bioelectronics,* vol. 71, pp. 445-455, 9/15/ 2015.

[65] C. L. Liu *et al.*, "Electric cell-substrate impedance sensing as a screening tool for wound healing agents," in *Electric cell-substrate impedance sensing and cancer metastasis*: Springer, 2012, pp. 203-216.

[66] W. G. Jiang, L. Ye, G. Patel, K. G. J. W. r. Harding, and regeneration, "Expression of WAVEs, the WASP (Wiskott–Aldrich syndrome protein) family of verprolin homologous proteins in human wound tissues and the biological influence on human keratinocytes," vol. 18, no. 6, pp. 594-604, 2010.

[67] S. Lieb, S. Michaelis, N. Plank, G. Bernhardt, A. Buschauer, and J. J. P. r. Wegener, "Label-free analysis of GPCR-stimulation: The critical impact of cell adhesion," vol. 108, pp. 65-74, 2016.

[68] N. Yu *et al.*, "Real-time monitoring of morphological changes in living cells by electronic cell sensor arrays: an approach to study G protein-coupled receptors," vol. 78, no. 1, pp. 35-43, 2006.

[69] C. R. Keese, K. Bhawe, J. Wegener, and I. J. B. Giaever, "Real-time impedance assay to follow the invasive activities of metastatic cells in culture," vol. 33, no. 4, pp. 842-850, 2002.

[70] B. H. Brown, D. C. Barber, A. H. Morice, and A. D. Leathard, "Cardiac and respiratory related electrical impedance changes in the human thorax," *IEEE Transactions on Biomedical Engineering,* vol. 41, no. 8, pp. 729-734, 1994.

[71] B. Brown *et al.*, "Multi-frequency imaging and modelling of respiratory related electrical impedance changes," *Physiological measurement,* vol. 15, no. 2A, p. A1, 1994.

[72] B. Brown *et al.*, "Blood flow imaging using electrical impedance tomography," vol. 13, no. A, p. 175, 1992.

[73] V. Cherepenin *et al.*, "Preliminary static EIT images of the thorax in health and disease," vol. 23, no. 1, p. 33, 2001.

[74] T.-P. Jung, S. Makeig, M. J. McKeown, A. J. Bell, T.-W. Lee, and T. J. Sejnowski, "Imaging brain dynamics using independent component analysis," *Proceedings of the IEEE,* vol. 89, no. 7, pp. 1107-1122, 2001.

[75] T. Oh, O. Gilad, A. Ghosh, M. Schuettler, and D. S. Holder, "A novel method for recording neuronal depolarization with recording at 125-825 Hz: implications for imaging fast neural activity in the brain with electrical impedance tomography," *Med Biol Eng Comput,* vol. 49, no. 5, pp. 593-604, May 2011.

[76] K. Y. Aristovich, G. S. dos Santos, B. C. Packham, and D. S. Holder, "A method for reconstructing tomographic images of evoked neural activity with electrical impedance tomography using intracranial planar arrays," *Physiological measurement,* vol. 35, no. 6, p. 1095, 2014.

[77] Y. Lin, X. Canhua, D. Meng, F. Feng, S. Xuetao, and D. Xiuzhen, "A novel multi-frequency electrical impedance tomography spectral imaging algorithm for early stroke detection," *Physiological Measurement*, vol. 37, no. 12, p. 2317, 2016.

[78] L. Yang *et al.*, "The Frequency Spectral Properties of Electrode-Skin Contact Impedance on Human Head and Its Frequency-Dependent Effects on Frequency-Difference EIT in Stroke Detection from 10Hz to 1MHz," *PloS one*, vol. 12, no. 1, p. e0170563, 2017.

[79] L. Fabrizi, A. McEwan, T. Oh, E. Woo, and D. Holder, "A comparison of two EIT systems suitable for imaging impedance changes in epilepsy," *Physiological measurement*, vol. 30, no. 6, p. S103, 2009.

[80] T. Dowrick, G. S. Dos Santos, A. Vongerichten, and D. Holder, "Parallel, multi frequency EIT measurement, suitable for recording impedance changes during epilepsy," *Journal of Electrical Bioimpedance*, vol. 6, no. 1, pp. 37-43, 2015.

[81] D. N. Huu, D. Kikuchi, O. Maruyama, A. Sapkota, and M. Takei, "Cole-Cole analysis of thrombus formation in an extracorporeal blood flow circulation using electrical measurement," *Flow Measurement and Instrumentation*, 2016.

[82] B. Eker, R. Meissner, A. Bertsch, K. Mehta, and P. Renaud, "Label-free recognition of drug resistance via impedimetric screening of breast cancer cells," *PloS one*, vol. 8, no. 3, p. e57423, 2013.

[83] G. Sze, "Detection of breast cancer with electrical impedance mammography," University of Sussex, 2012.

[84] T. Sun, S. Tsuda, N. Green, K. Zauner, and H. Morgan, "On-Chip Electrical Impedance Tomography for monitoring the kinetics in the cell culture," in *Twelfth International Conference on Miniaturized Systems for Chemistry and Life Sciences, San Diego, California, USA*, 2008, pp. 973-975.

[85] X. Liu, Y. Cui, J. Yao, H. Obara, T. Zhao, and M. Takei, "Development of electrical impedance tomography system for cell sedimentation detection in electrode-multilayered microchannel," in *Micro-NanoMechatronics and Human Science (MHS), 2016 International Symposium on*, 2016, pp. 1-6: IEEE.

[86] Q. Liu, H. Wi, T. I. Oh, E. J. Woo, and J. K. Seo, "Development of a prototype micro-EIT system using three sets of 15× 8 array electrodes," in *Journal of Physics: Conference Series*, 2010, vol. 224, no. 1, p. 012161: IOP Publishing.

[87] Q. Liu, T. I. Oh, H. Wi, E. J. Lee, J. K. Seo, and E. J. Woo, "Design of a microscopic electrical impedance tomography system using two current injections," *Physiological measurement*, vol. 32, no. 9, p. 1505, 2011.

[88] Y. Yang, J. Jia, S. Smith, N. Jamil, W. Gamal, and P.-O. Bagnaninchi, "A miniature electrical impedance tomography sensor and 3-D image reconstruction for cell imaging," *IEEE Sensors Journal*, vol. 17, no. 2, pp. 514-523, 2017.

[89] T. I. Oh *et al.*, "Validation of a multi-frequency electrical impedance tomography (mfEIT) system KHU Mark1: impedance spectroscopy and time-difference imaging," *Physiological measurement,* vol. 29, no. 3, p. 295, 2008.

[90] K. J. Bathe, *Finite element method*. Wiley Online Library, 2008.

[91] N. Polydorides, "Image reconstruction algorithms for soft-field tomography," University of Manchester: UMIST, 2002.

[92] W. Lionheart, N. Polydorides, and A. Borsic, "The reconstruction problem," *Electrical impedance tomography: methods, history and applications,* vol. 750309520, pp. 3-64, 2005.

[93] M. F. Jehl, "A Novel Framework for Head Imaging with Electrical Impedance Tomography," UCL (University College London), 2016.

[94] E. R. Malone, "Multifrequency methods for Electrical Impedance Tomography," Doctor of Philosophy Thesis (Doctoral), Department of Medical Physics and Biomedical Engineering, University College London, 2014.

[95] K. Paulson, W. Breckon, and M. Pidcock, "Electrode modelling in electrical impedance tomography," *SIAM Journal on Applied Mathematics,* vol. 52, no. 4, pp. 1012-1022, 1992.

[96] K.-S. Cheng, D. Isaacson, J. Newell, and D. G. Gisser, "Electrode models for electric current computed tomography," *IEEE Transactions on Biomedical Engineering,* vol. 36, no. 9, pp. 918-924, 1989.

[97] E. Somersalo, M. Cheney, and D. Isaacson, "Existence and uniqueness for electrode models for electric current computed tomography," *SIAM Journal on Applied Mathematics,* vol. 52, no. 4, pp. 1023-1040, 1992.

[98] W. Yang and L. Peng, "Image reconstruction algorithms for electrical capacitance tomography," *Measurement Science and Technology,* vol. 14, no. 1, p. R1, 2003.

[99] Z. Cui *et al.*, "A review on image reconstruction algorithms for electrical capacitance/resistance tomography," vol. 36, no. 4, pp. 429-445, 2016.

[100] W. R. Lionheart, "EIT reconstruction algorithms: pitfalls, challenges and recent developments," *Physiological measurement,* vol. 25, no. 1, p. 125, 2004.

[101] P. C. Hansen, *Discrete inverse problems: insight and algorithms*. Siam, 2010.

[102] Y. Yang, J. Jia, N. Polydorides, and H. McCann, "Effect of structured packing on EIT image reconstruction," in *Imaging Systems and Techniques (IST), 2014 IEEE International Conference on*, 2014, pp. 53-58: IEEE.

[103] Q. Wang *et al.*, "Image reconstruction based on L1 regularization and projection methods for electrical impedance tomography," *Review of scientific instruments,* vol. 83, no. 10, p. 104707, 2012.

[104] J. Zhao, F. Dong, C. Tan, and Y. Xu, "Sparse regularization for small objects imaging with electrical resistance tomography," in *Imaging Systems and*

Techniques (IST), 2013 IEEE International Conference on, 2013, pp. 25-30: IEEE.

[105] A. Borsic, B. M. Graham, A. Adler, and W. R. Lionheart, "In vivo impedance imaging with total variation regularization," *IEEE transactions on medical imaging,* vol. 29, no. 1, pp. 44-54, 2010.

[106] I. Daubechies, M. Defrise, and C. De Mol, "An iterative thresholding algorithm for linear inverse problems with a sparsity constraint," *Communications on pure and applied mathematics,* vol. 57, no. 11, pp. 1413-1457, 2004.

[107] T. Blumensath and M. E. Davies, "Iterative Thresholding for Sparse Approximations," *Journal of Fourier Analysis and Applications,* journal article vol. 14, no. 5, pp. 629-654, December 01 2008.

[108] M. Schmidt, "Least squares optimization with L1-norm regularization," *CS542B Project Report,* pp. 14-18, 2005.

[109] B. Chen, J. Abascal, and M. Soleimani, "Electrical Resistance Tomography for Visualization of Moving Objects Using a Spatiotemporal Total Variation Regularization Algorithm," *Sensors,* vol. 18, no. 6, p. 1704, 2018.

[110] Z. Zhou *et al.*, "Multifrequency electrical impedance tomography with total variation regularization," *Physiological Measurement,* vol. 36, no. 9, p. 1943, 2015.

[111] A. Beck and M. Teboulle, "A fast iterative shrinkage-thresholding algorithm for linear inverse problems," *SIAM journal on imaging sciences,* vol. 2, no. 1, pp. 183-202, 2009.

[112] Q. Dai and W. Sha, "The physics of compressive sensing and the gradient-based recovery algorithms," *arXiv preprint arXiv:0906.1487,* 2009.

[113] T. Goldstein and S. Osher, "The split Bregman method for L1-regularized problems," *SIAM journal on imaging sciences,* vol. 2, no. 2, pp. 323-343, 2009.

[114] L. Jinzhen, L. Ling, Z. Weibo, and L. Gang, "A novel combined regularization algorithm of total variation and Tikhonov regularization for open electrical impedance tomography," *Physiological Measurement,* vol. 34, no. 7, p. 823, 2013.

[115] W. He, B. Li, Z. Xu, H. Luo, P. J. B. E. A. Ran, Basis, and Communications, "A combined regularization algorithm for electrical impedance tomography system using rectangular electrodes array," vol. 24, no. 04, pp. 313-322, 2012.

[116] S. I. Kang, A. K. Khambampati, M. H. Jeon, B. S. Kim, and K. Y. Kim, "A sub-domain based regularization method with prior information for human thorax imaging using electrical impedance tomography," *Measurement Science and Technology,* vol. 27, no. 2, p. 025703, 2016.

[117] M. Zhang, "Permittivity and Conductivity Imaging in Electrical Capacitance Tomography," University of Bath, 2016.

[118] X. Yin, H. Wu, J. Jia, and Y. Yang, "A Micro EIT Sensor for Real-Time and Non-Destructive 3-D Cultivated Cell Imaging," *IEEE Sensors Journal,* vol. 18, no. 13, pp. 5402-5412, 2018.

[119] Y. Yang, "Advanced digital electrical impedance tomography system for biomedical imaging," PhD, The University of Edinburgh, 2018.

[120] Y. Yang, H. Wu, and J. Jia, "Optimal Design of a Planar Miniature EIT Sensor for 3D Cell Imaging," presented at the 18th International Conference on Biomedical Applications of Electrical Impedance Tomography, Thayer School of Engineering at Dartmouth, Hanover, New Hampshire, USA, 2017.

[121] Y. Yang and J. Jia, "A multi-frequency electrical impedance tomography system for real-time 2D and 3D imaging," *Review of Scientific Instruments,* vol. 88, no. 8, p. 085110, 2017.

[122] S. C. Jun, J. Kuen, J. Lee, E. J. Woo, D. Holder, and J. K. Seo, "Frequency-difference EIT (fdEIT) using weighted difference and equivalent homogeneous admittivity: validation by simulation and tank experiment," *Physiological measurement,* vol. 30, no. 10, p. 1087, 2009.

[123] B. Packham *et al.*, "Comparison of frequency difference reconstruction algorithms for the detection of acute stroke using EIT in a realistic head-shaped tank," *Physiological measurement,* vol. 33, no. 5, p. 767, 2012.

[124] T. K. Bera, J. Nagaraju, and G. Lubineau, "Electrical impedance spectroscopy (EIS)-based evaluation of biological tissue phantoms to study multifrequency electrical impedance tomography (Mf-EIT) systems," *Journal of Visualization,* journal article pp. 1-23, 2016.

[125] R. A. Scott, J. Palmisano, G. Justin, and M. Nasir, "MICRO BIOIMPEDANCE TOMOGRAPHY FOR CONTINUOUS MONITORING OF CELLULAR PROCESSES," presented at the 18th International Conference on Miniaturized Systems for Chemistry and Life Sciences, San Antonio, Texas, USA, 2014.

[126] C. Canali *et al.*, "Electrical impedance tomography methods for miniaturised 3D systems," *Journal of Electrical Bioimpedance,* vol. 7, no. 1, pp. 59-67, 2016.

[127] A. Boyle and A. Adler, "The impact of electrode area, contact impedance and boundary shape on EIT images," *Physiological measurement,* vol. 32, no. 7, p. 745, 2011.

[128] J. Sun and W. Yang, "Evaluation of fringe effect of electrical resistance tomography sensor," *Measurement,* vol. 53, pp. 145-160, 2014.

[129] S. V. Puttaswamy, S. Sivashankar, R. J. Chen, C. K. Chin, H. Y. Chang, and C. H. J. B. j. Liu, "Enhanced cell viability and cell adhesion using low conductivity medium for negative dielectrophoretic cell patterning," vol. 5, no. 10, pp. 1005-1015, 2010.

[130] H. P. Schwan and C. D. Ferris, "Four‐electrode null techniques for impedance measurement with high resolution," *Review of scientific instruments,* vol. 39, no. 4, pp. 481-485, 1968.

[131] J. Joshi, D. Kanchan, M. Joshi, H. Jethva, and K. Parikh, "Dielectric relaxation, complex impedance and modulus spectroscopic studies of mix phase rod like cobalt sulfide nanoparticles," *Materials Research Bulletin,* vol. 93, pp. 63-73, 2017.

[132] N. Otsu, "A Threshold Selection Method from Gray-Level Histograms," *IEEE Transactions on Systems, Man, and Cybernetics,* vol. 9, no. 1, pp. 62-66, 1979.

[133] A. Adler *et al.,* "GREIT: a unified approach to 2D linear EIT reconstruction of lung images," *Physiological measurement,* vol. 30, no. 6, p. S35, 2009.

[134] H. Schwan, "Electrical properties of tissues and cell suspensions: mechanisms and models," in *Engineering in Medicine and Biology Society, 1994. Engineering Advances: New Opportunities for Biomedical Engineers. Proceedings of the 16th Annual International Conference of the IEEE,* 1994, pp. A70-A71 vol. 1: IEEE.

[135] J. B. Kolbeck, "Excitation frequency dependence of conductivity of electrolytic solutions," NAVAL POSTGRADUATE SCHOOL MONTEREY CA1983.

[136] V. Koshkin, L. E. Ailles, G. Liu, and S. N. Krylov, "Metabolic Suppression of a Drug‐Resistant Subpopulation in Cancer Spheroid Cells," *Journal of cellular biochemistry,* vol. 117, no. 1, pp. 59-65, 2016.

[137] K. Shield, M. L. Ackland, N. Ahmed, and G. E. Rice, "Multicellular spheroids in ovarian cancer metastases: Biology and pathology," *Gynecologic oncology,* vol. 113, no. 1, pp. 143-148, 2009.

[138] M. Hay, D. W. Thomas, J. L. Craighead, C. Economides, and J. Rosenthal, "Clinical development success rates for investigational drugs," *Nature biotechnology,* vol. 32, no. 1, pp. 40-51, 2014.

[139] N. J. Martucci *et al.*, "Nondestructive Optical Toxicity Assays of 3D Liver Spheroids with Optical Coherence Tomography," *Advanced Biosystems,* pp. 1700212-n/a, Art. no. 1700212.

[140] J. Friedrich, C. Seidel, R. Ebner, and L. A. Kunz-Schughart, "Spheroid-based drug screen: considerations and practical approach," *Nature protocols,* vol. 4, no. 3, pp. 309-324, 2009.

[141] A. Geltmeier *et al.*, "Characterization of dynamic behaviour of MCF7 and MCF10A cells in ultrasonic field using modal and harmonic analyses," *PloS one,* vol. 10, no. 8, p. e0134999, 2015.

[142] M. Pavlin, N. Pavselj, and D. Miklavcic, "Dependence of induced transmembrane potential on cell density, arrangement, and cell position inside a cell system," *IEEE Transactions on Biomedical Engineering,* vol. 49, no. 6, pp. 605-612, 2002.

[143] Y. Yang, J. Jia, S. Smith, N. Jamil, W. Gamal, and P. Bagnaninchi, "A Miniature Electrical Impedance Tomography Sensor and 3D Image Reconstruction for Cell Imaging," *IEEE Sensors Journal,* vol. PP, no. 99, pp. 1-1, 2016.

[144] E. C. Costa, V. M. Gaspar, P. Coutinho, and I. J. Correia, "Optimization of liquid overlay technique to formulate heterogenic 3D co‐cultures models," *Biotechnology and bioengineering*, vol. 111, no. 8, pp. 1672-1685, 2014.

[145] D. Koley and A. J. Bard, "Triton X-100 concentration effects on membrane permeability of a single HeLa cell by scanning electrochemical microscopy (SECM)," *Proceedings of the National Academy of Sciences*, vol. 107, no. 39, pp. 16783-16787, 2010.

[146] Y. Huang, N. S. Sekhon, J. Borninski, N. Chen, and B. Rubinsky, "Instantaneous, quantitative single-cell viability assessment by electrical evaluation of cell membrane integrity with microfabricated devices," *Sensors and Actuators A: Physical*, vol. 105, no. 1, pp. 31-39, 2003/06/15/ 2003.

[147] D. J. J. o. c. e. Swinehart, "The beer-lambert law," vol. 39, no. 7, p. 333, 1962.

[148] T. Tobe, K. Ueda, M. Ando, Y. Okamoto, and N. J. J. J. o. B. I. C. Kojima, "Thiol-mediated multiple mechanisms centered on selenodiglutathione determine selenium cytotoxicity against MCF-7 cancer cells," vol. 20, no. 4, pp. 687-694, 2015.

[149] P. Peidaee, N. Almansour, R. Shukla, E. J. C. Pirogova, and s. b. journal, "The cytotoxic effects of low intensity visible and infrared light on human breast cancer (MCF7) cells," vol. 6, no. 7, p. e201303015, 2013.

[150] M. Brischwein *et al.*, "Electric cell-substrate impedance sensing with screen printed electrode structures," *Lab on a Chip*, vol. 6, no. 6, pp. 819-822, 2006.

[151] T. Schwarzenberger *et al.*, "Bioimpedance microelectronics in a 24-microwell plate with metabolic-sensors for testing chemosensitivity of tumor cells and tissues," in *Journal of Physics: Conference Series*, 2010, vol. 224, no. 1, p. 012141: IOP Publishing.

[152] T. Schwarzenberger *et al.*, "Impedance sensor technology for cell-based assays in the framework of a high-content screening system," *Physiological measurement*, vol. 32, no. 7, p. 977, 2011.

[153] A. Borsic, E. Attardo, and R. Halter, "Multi-GPU Jacobian accelerated computing for soft-field tomography," *Physiological measurement*, vol. 33, no. 10, p. 1703, 2012.

[154] R. Langer and J. Vacanti, "Tissue engineering," *Science*, vol. 260, no. 5110, pp. 920-926, 1993.

[155] A. Shafiee and A. Atala, "Tissue engineering: Toward a new era of medicine," *Annual review of medicine*, vol. 68, pp. 29-40, 2017.

[156] P. Linderholm, T. Braschler, J. Vannod, Y. Barrandon, M. Brouard, and P. Renaud, "Two-dimensional impedance imaging of cell migration and epithelial stratification," *Lab on a Chip*, vol. 6, no. 9, pp. 1155-1162, 2006.

[157] H. Wu, Y. Yang, P. O. Bagnaninchi, and J. Jia, "Electrical impedance tomography for real-time and label-free cellular viability assays of 3D tumour spheroids," *Analyst*, 10.1039/C8AN00729B vol. 143, no. 17, pp. 4189-4198, 2018.

[158] L. A. Solchaga *et al.*, "A rapid seeding technique for the assembly of large cell/scaffold composite constructs," *Tissue engineering,* vol. 12, no. 7, pp. 1851-1863, 2006.

[159] X. Yin, H. Wu, J. Jia, and Y. Yang, "A Micro EIT Sensor for Real-time and Non-destructive 3-D Cultivated Cell Imaging," *IEEE Sensors Journal,* pp. 1-1, 2018.

[160] X. Yin, Y. Yang, J. Jia, and C. Tan, "3D image reconstruction on a miniature planar EIT sensor using sparsity with median filter," in *SENSORS, 2017 IEEE*, 2017, pp. 1-3: IEEE.

[161] B. Obradovic, R. L. Carrier, G. Vunjak‐Novakovic, L. E. J. B. Freed, and bioengineering, "Gas exchange is essential for bioreactor cultivation of tissue engineered cartilage," vol. 63, no. 2, pp. 197-205, 1999.

[162] J. R. Fuchs, B. A. Nasseri, and J. P. Vacanti, "Tissue engineering: a 21st century solution to surgical reconstruction," *The Annals of thoracic surgery,* vol. 72, no. 2, pp. 577-591, 2001.

[163] J. P. Vacanti and C. A. Vacanti, "The history and scope of tissue engineering," in *Principles of Tissue Engineering (Fourth Edition)*: Elsevier, 2014, pp. 3-8.

[164] A. Mazzoleni, B. Sisken, and R. Kahler, "Conductivity values of tissue culture medium from 20 C to 40 C," *Bioelectromagnetics: Journal of the Bioelectromagnetics Society, The Society for Physical Regulation in Biology and Medicine, The European Bioelectromagnetics Association,* vol. 7, no. 1, pp. 95-99, 1986.

[165] R. Firstenberg-Eden and J. Zindulis, "Electrochemical changes in media due to microbial," *Journal of microbiological methods,* vol. 2, no. 2, pp. 103-115, 1984.

[166] H. Sudibyo, D. Sudiana, A. S. Tamsir, I. Muttakin, W. Widada, and W. P. Taruno, "Switch Configuration Effect on Stray Capacitance in Electrical Capacitance Volume Tomography Hardware," *TELKOMNIKA (Telecommunication Computing Electronics and Control),* vol. 14, no. 2, pp. 456-463, 2016.

[167] M. Wang, "Electrode models in electrical impedance tomography," *Journal of Zhejiang University-SCIENCE A,* vol. 6, no. 12, pp. 1386-1393, 2005.

[168] Y. Jiang and M. Soleimani, "Capacitively Coupled Resistivity Imaging for Biomaterial and Biomedical Applications," *IEEE Access,* 2018.

[169] B. Veal, P. Baldo, A. Paulikas, and J. Eastman, "Understanding artifacts in impedance spectroscopy," *Journal of The Electrochemical Society,* vol. 162, no. 1, pp. H47-H57, 2015.

[170] M. R. Baidillah, A.-A. S. Iman, Y. Sun, and M. Takei, "Electrical Impedance Spectro-Tomography Based on Dielectric Relaxation Model," *IEEE Sensors Journal,* vol. 17, no. 24, pp. 8251-8262, 2017.

[171] C. Wu and M. Soleimani, "Frequency Difference EIT With Localization: A Potential Medical Imaging Tool During Cancer Treatment," *IEEE Access*, vol. 7, pp. 21870-21878, 2019.

[172] M. Michalikova, R. Abed, M. Prauzek, and J. Koziorek, "Image reconstruction in electrical impedance tomography using neural network," in *2014 Cairo International Biomedical Engineering Conference (CIBEC)*, 2014, pp. 39-42.

[173] C. Tan, S. Lv, F. Dong, and M. Takei, "Image Reconstruction Based on Convolutional Neural Network for Electrical Resistance Tomography," *IEEE Sensors Journal*, pp. 1-1, 2018.

[174] Z. Hao, S. Yue, B. Sun, and H. Wang, "Optimal distance of multi-plane sensor in three-dimensional electrical impedance tomography," *Computer Assisted Surgery*, vol. 22, no. sup1, pp. 326-338, 2017.

[175] M. Z. J. I. j. o. e. e. e. Abdullah, "Simulation of an inverse problem in electrical impedance tomography using resistance electrical network analogues," vol. 36, no. 4, pp. 311-324, 1999.

[176] C. Yang, A. Mohammed, Y. Mohamadou, T. Oh, and M. Soleimani, "Complex conductivity reconstruction in multiple frequency electrical impedance tomography for fabric-based pressure sensor," *Sensor Review*, vol. 35, no. 1, pp. 85-97, 2015.

[177] J. Yao and M. Takei, "Application of process tomography to multiphase flow measurement in industrial and biomedical fields: A review," *IEEE Sensors Journal*, vol. 17, no. 24, pp. 8196-8205, 2017.

[178] H. Wu, S. Liu, Y. Yang, P. Bagnaninchi, and J. Jia, "Multi-plane electrode configuration for 3D cellular assay of electrical impedance tomography," presented at the 19th International Conference on Biomedical Applications of Electrical Impedance Tomography, University of Edinburgh, Edinburgh, UK, 2018.

[179] J. Lei, H. Mu, Q. Liu, Z. Li, S. Liu, and X. Wang, "Tensor-based dynamic reconstruction method for electrical capacitance tomography," *Measurement Science and Technology*, vol. 28, no. 3, p. 035403, 2017.

[180] M. Nahvi and B. Hoyle, "Wideband electrical impedance tomography," *Measurement Science and Technology*, vol. 19, no. 9, p. 094011, 2008.

[181] M. Baidillah, A.-a. Iman, Y. Sun, and M. Takei, "Electrical Impedance Spectro-Tomography (EIST) based on Dielectric Relaxation Model," *IEEE Sensors Journal*, 2017.